

The Effects of Fluid Elasticity on Grid Turbulence

THÈSE N° 4676 (2010)

PRÉSENTÉE LE 14 MAI 2010

À LA FACULTÉ SCIENCES ET TECHNIQUES DE L'INGÉNIEUR
LABORATOIRE DE MÉCANIQUE DES FLUIDES
PROGRAMME DOCTORAL EN MÉCANIQUE

ÉCOLE POLYTECHNIQUE FÉDÉRALE DE LAUSANNE

POUR L'OBTENTION DU GRADE DE DOCTEUR ÈS SCIENCES

PAR

Richard VONLANTHEN

acceptée sur proposition du jury:

Dr M. Farhat, président du jury
Prof. P. Monkewitz, directeur de thèse
Prof. C. Ancey, rapporteur
Prof. P. Jenny, rapporteur
Dr C. Pipe, rapporteur



ÉCOLE POLYTECHNIQUE
FÉDÉRALE DE LAUSANNE

Suisse
2010

To Lucia

I didn't think; I experimented.
Anthony Burgess

Abstract

Experiments on grid turbulence are reported for pure water and dilute Polyox WSR 301 solutions. A novel passive grid, which consists of a square mesh grid with tethered spheres, has been developed to enhance the turbulence properties. In pure water the new grid produces higher turbulence intensities per unit C_p (pressure drop coefficient) than the classic plain grid, and the turbulence Reynolds number Re_λ is increased by a factor of roughly two.

In polymer solutions turbulence dissipation rates and energy spectra were measured using PIV with a high spatial resolution. The energy spectra reveal a characteristic length scale at which the polymers begin to affect the energy cascade. Above this scale the turbulence is essentially Newtonian, whereas below this scale the energy flux from large to small scales is reduced proportional to the length scale squared. Consequently, the energy in this new self-regulating spectral region scales according to a power-law with an exponent of -3 instead of the $-5/3$ for Newtonian turbulence, and the excess energy is dissipated by the polymers.

Keywords: turbulence; grid turbulence; non-Newtonian; improved passive grid; particle image velocimetry; dissipation by polymers.

Zusammenfassung

Es wurden Experimente zur Gitterturbulenz in reinem Wasser und verdünnten Polyox WSR 301-Lösungen angestellt. Dazu wurde ein neuartiges passives Gitter entworfen, das aus einem klassischen Gitter und festgebundenen Kugeln besteht. In reinem Wasser produziert das neue Gitter höhere Turbulenzintensitäten pro C_p -Einheit (Druckabfallkoeffizient) als das klassische einfache Gitter, und die Turbulenz-Reynolds-Zahl Re_λ ist rund um das zweifache erhöht.

In Polymerlösungen wurden Turbulenzdissipationsraten und Energiespektren unter Einsatz von PIV mit einer hohen räumlichen Auflösung gemessen. Die Energiespektren zeigen eine charakteristische Längenskala bei welcher die Polymere anfangen die Energiekaskade zu beeinflussen. Oberhalb dieser Skala ist die Turbulenz im Wesentlichen Newtonsch, wohingegen unterhalb der Energiefluss von grossen zu kleinen Skalen proportional zum Quadrat der Längenskala reduziert wird. Infolgedessen nimmt die Energie in diesem neuen, selbst-regulierenden Spektralbereich gemäss eines Potenzgesetzes ab, mit einem Exponent von -3 anstatt $-5/3$ wie im Newtonschen Fall. Die überschüssige Energie wird durch die Polymere in Wärme umgewandelt.

Stichwörter: Turbulenz; Gitterturbulenz; nicht-Newtonsch; verbessertes passives Gitter; Particle Image Velocimetry; Dissipation durch Polymere.

Danksagung

Diese Arbeit entstand während meiner Anstellung im Laboratoire de Mécanique des Fluides an der EPFL, mit der finanziellen Unterstützung des Schweizer National Fonds (SNF).

Mein ganz besonderer Dank gilt meinem Doktorvater Prof. Peter Monkewitz, welcher mir nicht nur diese Arbeit ermöglicht hat, sondern mir auch stets mit Rat und Tat zur Seite gestanden ist. Er hat mir ein grosses Vertrauen entgegengebracht und viel Freiraum zur Gestaltung des Experiments gelassen. Die vielen interessanten Diskussionen waren wohl der grösste Ansporn diese Arbeit fertigzukriegen.

I would also like to thank the members of the jury, Prof. Patrick Jenny, Prof. Christophe Ancey, Dr. Christopher Pipe and of course Dr. Mohamed Farhat for their constructive comments and critics.

Je tiens également à remercier le Dr. Trong Vien Truong pour son expertise précieuse et indispensable pour l'aboutissement de ce travail expérimental. Je le remercie particulièrement pour sa patience et sa confiance quand il m'a confié des instruments de mesure.

La bonne réussite de l'expérience est due au savoir-faire de l'équipe de l'atelier, notamment de Bernard Savary et Marc Salle. Je les remercie surtout pour leur flexibilité envers mes dessins souvent très minimalistes.

Je dois également remercier le Laboratoire de Thermique appliquée et de Turbomachines, notamment à Virginie et Elia qui m'ont prêté leur système LDA. Je n'exagère pas quand je dis que sans leur générosité je n'aurais pas pu terminer ce travail.

Speaking of borrowed equipment, I would like to thank Jeff of the Laboratory of Heat and Mass Transfer, for helping me out with the high-speed camera.

Dans la liste des gens importants pour ces dernières années j'aimerais aussi mentionner l'ancien labo: Emeric, Radboud, Etienne, Flavio, Chris et David. Sans Emeric, certains outils de mesure ne fonctionneraient probablement toujours pas. Mais je le remercie surtout de m'avoir remonté le moral lors des nombreuses bières et burgers. J'aimerais aussi remercier à Chris, pour m'avoir transmis son savoir-faire, pour m'avoir donné l'opportunité de le visiter au MIT, et en particulier pour les sorties de grimpe. Je continue la liste avec Martin, Jonathan, Gaffu et Emanuele pour toutes les fois où on est allé courir, ainsi que Roland, Orestis, Benoit, Marc-Antoine, Prof. François Gallaire, Mathias, Edouard et Philippe pour les nombreuses pauses café. C'est grâce à tout ces gens que je vais garder de bons souvenirs de

DANKSAGUNG

cette aventure.

I am also grateful to Eva Gasser who always found the right word to cheer me up, and Dr. Navid Borhani for his interest in this study.

Many thanks to Dr. Sheldon Cooper and J.D. for distracting me whenever it was necessary, as well as Jorge Cham for reassuring me that there are other grad students with the same experiences.

Und zum Glück gibt es da noch ein paar Fribourgeois die es ab und zu doch noch geschafft haben, dass ich wenigstens fürs Wochenende den Laser gegen ein Snowboard tausche: Merci Alex, Lukas, Beat, Jonas, Thomas, Marc und Benja.

Nun möchte ich auch noch den wichtigsten Menschen danken, ohne deren Unterstützung, Motivation und Geduld die Arbeit nicht zustande gekommen wäre, meinen Eltern, meiner Schwester, und ganz besonders Lucia.

Allen anderen die ich hier vergessen habe aufzuzählen: Merci.

Contents

CHAPTER 1 Introduction	
1.1	Turbulence in elastic fluids 1
1.2	Grid turbulence 2
1.3	Turbulence velocity spectra 3
1.4	Thesis layout and contributions 5
CHAPTER 2 Aqueous poly(ethylene oxide) solutions	
2.1	Ideal elastic fluids and polymer solutions 7
2.2	Rheological description of dilute polymer solutions 8
2.2.1	Material functions and dimensionless groups, 10
2.2.2	Models for polymer solutions, 10
2.2.3	Data reduction, 12
2.3	Fluids and instrumentation 13
2.3.1	Preparation of sample solutions and tunnel fluids, 13
2.3.2	Rheological measuring systems, 14
2.4	Characteristics of the working fluids 15
2.4.1	Molecular weight and coil overlap concentration, 15
2.4.2	Concentration and temperature dependence of the viscosity, 16
2.4.3	Shear dependent viscosity, 17
2.4.4	Relaxation time, 20
2.4.5	Resistance to mechanical degradation, 23
2.5	Final remarks 24
CHAPTER 3 Experiment setup and data processing	
3.1	Closed-loop flow facility 25
3.2	Turbulence grids 28
3.3	Differential static pressure measurement 30
3.4	Hot-film anemometry 31
3.4.1	HFA data acquisition, 31
3.4.2	Velocity spectra and rms, 32

CONTENTS

3.5	Particle image velocimetry	35
3.5.1	PIV setup and calibration, 35	
3.5.2	PIV processing, 37	
3.5.3	Velocity spectra and rms, 38	
3.6	Laser Doppler anemometry	41
3.6.1	LDA setup and recording details, 41	
3.6.2	Velocity spectra, 42	
3.7	Monitoring of temperature and viscosity	43
3.8	Turbulence dissipation and length scales	44
3.8.1	Energy dissipation rate, 45	
3.8.2	Turbulence length scales, 47	
3.9	Summary of experimental runs	48
CHAPTER 4 Performance of the new grid in water		
4.1	Brief overview	51
4.2	Grid pressure drop	51
4.3	Homogeneity and streamwise decay	52
4.3.1	Transverse homogeneity, 52	
4.3.2	Streamwise energy decay, 55	
4.4	Velocity spectra	61
4.4.1	Comparison of all tested grids, 61	
4.4.2	Improved turbulence grid, 65	
4.5	Correlation functions and length scales	66
4.6	Direct measurement of the dissipation rate	71
4.7	Concluding remarks	74
CHAPTER 5 Grid turbulence in polymer solutions		
5.1	Brief overview	77
5.2	Experimental conditions	77
5.3	Degradation of the polymer solutions	79
5.3.1	Fluid viscosity, 79	
5.3.2	Static pressure drop, 79	
5.3.3	Fluid elasticity, 81	
5.4	Turbulence spectra in polymer solutions	82
5.4.1	Kinetic energy and large-scale isotropy, 82	
5.4.2	Effects of fluid elasticity on velocity spectra, 83	
5.4.3	Viscous and polymer dissipation rate, 90	
5.5	Summary and concluding remarks	92
5.5.1	The model spectrum, 92	
5.5.2	General remarks, 95	

CONTENTS

CHAPTER 6	Final remarks and outlook	
6.1	Summary of the most important findings	97
6.2	Perspectives	98
References		99
List of Figures		107
List of Tables		109
Notation		111

CHAPTER 1

Introduction

1.1 TURBULENCE IN ELASTIC FLUIDS

The Toms effect¹³⁷ describes a phenomenon in which a significant lowering of the pressure drop necessary to maintain turbulent flow occurs when adding minute amounts of a high molar mass polymer to the fluid. Besides their obvious industrial relevance, these *drag-reducing*^{25, 87, 118, 145} flows also present a fundamental interest. Since their discovery, a vast number of experimental, numerical and analytical efforts have been made, but the phenomenon—the interaction between turbulence and polymers—is still not well understood.

It should be stressed that the turbulence in question is the *inertial turbulence* at high Reynolds numbers, which differs in its nature from the *structural turbulence*⁹², also called *elastic turbulence*⁵⁹. The latter occurs in viscoelastic fluids at low Reynolds numbers and emerges from viscoelastic instabilities.⁶⁰

Polymer solutions are the favored fluids to investigate viscoelasticity, because they exhibit elastic effects already at concentrations as low as a few parts per million¹⁰. Moreover, there exist many polymer grades that are soluble in water and hence simplify the experimental setup. The nature of the polymer-solvent system depends on the the solvent and the polymer concentration.^{47, 58} At high concentrations the polymers tend to built networks, whereas in dilute solutions they don't interact. The complexity and the origin of the resulting elastic effects change accordingly. It seems clear that for a fundamental approach, solutions with individual polymer coils have to be considered first.

The majority of existing experimental studies on turbulence in polymer solutions were realized in pipe flows (e.g., refs. 41, 46, 76, 102, 146), and only a few investigations were carried out in grid-generated turbulence (viz., refs. 10, 51, 53, 93, 141) or other experimental configurations producing nearly homogeneous and isotropic turbulence^{83, 84}. Homogeneous and isotropic turbulence¹² is essentially decaying and polymer chains can only modify the energy fluxes from large to small scales. This greatly reduces the complexity of the problem compared to situations with mean shear, as in channel flows.

Among the numerical studies, the one by Berti et al.¹⁷ was of particular interest for the present experimental investigation. They investigated the effect of polymers on the energy fluxes in homogeneous turbulence, and found that there

INTRODUCTION

exists a characteristic turbulence length scale ℓ_p at which the polymers start to affect the energy cascade. Below this scale, turbulence kinetic energy is dissipated by the viscous drag of relaxing polymer coils¹⁰¹, and ℓ_p acts like a new dissipation scale. Necessarily, the energy cascade deviates from the Newtonian case below ℓ_p , whereas turbulence scales larger than ℓ_p remain essentially unaffected. This describes closely the ideas about turbulence-polymer interaction put forward by Balkovsky et al.⁸ and Fouxon and Lebedev⁴⁹.

Another, competing scenario exists^{15, 17}: the dissipation through polymer relaxation is limited to a relatively narrow range of scales around ℓ_p , below which the inertial turbulence cascade proceeds at a reduced energy flux. Thus, elastic effects manifest at turbulence scales that are neither too large nor too small.

When testing these hypotheses experimentally, a major issue is the degradation of polymer solutions in turbulent flows, which leads to lower molecular weights and reduced elastic effects. Friehe and Schwarz⁵¹ ran grid turbulence experiments on polyacrylamide solutions in a closed-loop flow tunnel and reported that the flow properties changed over long periods. In the present study, severe polymer degradation was observed. As this phenomenon is practically unavoidable in grid turbulence, it was seen as a chance to investigate elastic effects on turbulence in fluids of the same mass concentration but varying elastic properties in a single experimental run.

The most recent experimental investigation into elastic effects on grid turbulence was carried out in 1999 by van Doorn et al.¹⁴¹, two years before the paper by Balkovsky et al.⁸ was published. Although their measured turbulence spectra show some effect of the polymers, they do not correlate with any of the two models mentioned above. Moreover, the spectra seem to be heavily corrupted by experimental noise. Older turbulence spectra by McComb et al.⁹³ or Friehe and Schwarz⁵¹ lack accuracy and resolution. Therefore, it appeared necessary to conduct new experiments with focus on turbulence spectra.

1.2 GRID TURBULENCE

The classic setup to study homogeneous and isotropic turbulence is a grid placed normal to a uniform mean flow. Far behind the grid, turbulence production is essentially zero and one finds a simple decaying turbulence where the energy budget reads

$$\frac{dk}{dt} \equiv \frac{1}{2} \frac{d}{dt} \langle u_i u_i \rangle = -2\nu \langle s_{ij} s_{ij} \rangle, \quad (1.1)$$

in which k is the turbulence kinetic energy, u_i ($\equiv U_i - \langle U_i \rangle$, where $\langle \rangle$ denotes the time average) is the fluctuating velocity and s_{ij} ($\equiv S_{ij} - \langle S_{ij} \rangle$) is the fluctuating strain rate tensor defined in equation (1.10). (Notice the summation over dummy indices.) Because of its simplicity, this arrangement is very popular (e.g., refs. 13, 33, 50, 77, 111, 128), though it has some flaws. For example, it has the drawback to be limited in practice to small Reynolds number turbulence, where the turbulence spectrum is poorly developed¹². To this end, a variety of turbulence enhancing grids were

1.3 TURBULENCE VELOCITY SPECTRA

introduced^{52, 66, 85}. A particularly impressive effort was made by Makita⁹⁰ who introduced a sophisticated *active* grid. The turbulence Reynolds number

$$Re_\lambda \equiv \frac{\lambda u'_1}{\nu}, \quad (1.2)$$

was greatly improved and the inertial subrange clearly visible in the energy spectrum^{72, 79, 98}. In expression (1.2), ν is the kinematic viscosity, u'_1 is the root mean square (rms) velocity (i.e., $u'_i \equiv \sqrt{\langle u_i u_i \rangle}$), and λ is the Taylor microscale given in equation (1.13). But its mechanical complexity makes an application in smaller facilities or in water tunnels difficult. Thus, we developed yet another *passive* grid, intensifying turbulence by means of tethered spheres. This design concept is based on the random motion of the spheres^{57, 151}, and is simple to implement.

1.3 TURBULENCE VELOCITY SPECTRA

The following gives only a brief summary of a vast topic. For details, the reader may consult Hinze⁶⁴, McComb⁹², Pope¹⁰⁷, Tennekes and Lumley¹³⁴ or Batchelor¹².

The turbulence kinetic energy cascade of a given flow is best described by its velocity spectrum. In particular, one can measure the one-dimensional spectral energy density function

$$\phi_{ij}(\kappa_l) = 2 \iint_{-\infty}^{\infty} \Phi_{ij}(\boldsymbol{\kappa}) d\kappa_m d\kappa_n, \quad (1.3)$$

where $\Phi_{ij}(\boldsymbol{\kappa})$ is the velocity spectrum tensor, and $\boldsymbol{\kappa}$ the wavenumber vector. Here, the indices i, j, k and l, m, n can take the values 1, 2 and 3, referring to the components of Cartesian coordinates. The factor 2 is required to satisfy

$$u_i'^2 = \int_0^\infty \phi_{ii}(\kappa_l) d\kappa_l. \quad (1.4)$$

(The summation over repeated indices does not apply here.) This is convenient for working with measured one-dimensional spectra, as they are usually presented in a one-sided fashion, that is, for $0 < \kappa_l < \infty$.

For homogeneous and isotropic turbulence, Φ_{ij} has the form¹²

$$\Phi_{ij}(\boldsymbol{\kappa}) = \frac{E(\kappa)}{4\pi\kappa^4} (\kappa^2 \delta_{ij} - \kappa_i \kappa_j). \quad (1.5)$$

The three-dimensional spectral energy density function $E(\kappa)$ depends only on the magnitude of $\boldsymbol{\kappa}$. Pope¹⁰⁷ summarizes the turbulence spectra of various researchers with a model function for $E(\kappa)$,

$$E(\kappa) = \alpha \epsilon^{2/3} \kappa^{-5/3} \mathcal{F}_\Lambda(\kappa\Lambda) \mathcal{F}_\eta(\kappa\eta), \quad (1.6)$$

which describes the inertial range with Kolmogorov's famous $-5/3$ -law, as well as the integral range,

$$\mathcal{F}_\Lambda(\kappa\Lambda) = \left\{ \frac{\kappa\Lambda}{[(\kappa\Lambda)^2 + C_\Lambda]^{1/2}} \right\}^{5/3+2}, \quad (1.7)$$

INTRODUCTION

and the dissipation range,

$$\mathcal{F}_\eta(\kappa\eta) = \exp\left(-5.2\left[\{(\kappa\eta)^4 + C_\eta^4\}^{1/4} - C_\eta\right]\right). \quad (1.8)$$

Here, α is the Kolmogorov constant¹²⁶ with a value of 1.5. The length scales Λ and η are the integral and the Kolmogorov length scale, respectively. They represent the characteristic scales for the energy containing and the energy dissipating structures of a turbulent flow.

The parameter ϵ designates the rate at which turbulence kinetic energy is transferred from large to small scales, hence, the energy flux. This important quantity is defined as⁶⁴

$$\epsilon \equiv 2\nu \langle s_{ij}s_{ij} \rangle = \nu \left\langle \left(\frac{\partial u_i}{\partial x_j} + \frac{\partial u_j}{\partial x_i} \right) \frac{\partial u_j}{\partial x_i} \right\rangle, \quad (1.9)$$

where

$$s_{ij} \equiv \frac{1}{2} \left(\frac{\partial u_i}{\partial x_j} + \frac{\partial u_j}{\partial x_i} \right) \quad (1.10)$$

is the rate-of-strain tensor. Together with the integral scale and the Kolmogorov scale, this parameter defines the turbulence energy cascade.

The remaining constants $C_\Lambda = 6.78$ and $C_\eta = 0.4$ were determined¹⁰⁷ such that the integrals

$$k = \int_0^\infty E(\kappa) d\kappa \quad (1.11)$$

and

$$\epsilon = 2\nu \int_0^\infty \kappa^2 E(\kappa) d\kappa \quad (1.12)$$

are satisfied.

The Taylor microscale used for the Reynolds number in equation (1.2) is also a characteristic length scale for the fine structures of the turbulent motion, as it designates the smallest turbulent eddies that are not affected by viscous dissipation. For an isotropic flow it is given by^{64, 134}

$$\lambda^2 = u_1'^2 / \left\langle \left(\frac{\partial u_1}{\partial x_1} \right)^2 \right\rangle, \quad (1.13)$$

or alternatively by means of the kinetic energy,

$$\lambda^2 = 10\nu \frac{k}{\epsilon}. \quad (1.14)$$

The direct measurement of spatial velocity derivatives in a turbulent flow, in order to evaluate expression (1.9), is a very challenging task that demands a high spatial resolution. In this context, particle image velocimetry (PIV) appears to be the obvious choice. Ideally, the measurement technique should resolve the Kolmogorov scale, as well as the large scales. In typical grid-generated turbulence, these two length scales are separated by more than three decades and hence, it is not possible with PIV to capture all length scales. Consequently, a compromise is found by measuring the intermediate wavenumber range, and applying corrections for the filtered small scales.

1.4 THESIS LAYOUT AND CONTRIBUTIONS

There are two major contributions in this work. First, it introduces a novel passive turbulence grid with turbulence enhancing capabilities, which has a simple geometry and is applicable in wind and water tunnels. Second, it presents measurements of velocity spectra and energy dissipation rates in dilute polymer solutions with an improved quality relative to existing results. These measurements allow to identify important features of the turbulent motion in polymer solutions and adapt the existing models.

The following chapters first treat the polymer solutions employed in the present study, followed by the experimental setup with details on the data processing. These include descriptions of the correction procedures for each measurement technique, and highlights their importance. The subsequent chapters four and five summarize the findings on the new grid and the turbulence properties in polymer solutions. Concluding remarks and a brief outlook on future work are given in the last chapter.

CHAPTER 2

Aqueous poly(ethylene oxide) solutions

2.1 IDEAL ELASTIC FLUIDS AND POLYMER SOLUTIONS

Viscoelastic fluids are special because of their ability to ‘remember’ their deformation history, and so their behavior for a given flow configuration, for example a turbulent flow, differs from Newtonian fluids. Many types of viscoelastic fluids exist, for example shower gel, bread dough or saliva, but only a few are suitable for turbulence experiments. More specifically, an ideal viscoelastic fluid should have the following properties: highly elastic, constant and low viscosity, transparent, non-toxic and if possible, cheap. These requirements closely apply to polymer solutions. Moreover, they are very effective: only a few parts per million of polymers dissolved in a Newtonian solvent are necessary to exhibit viscoelastic behavior. Unfortunately, they also have drawbacks, such as a shear dependent viscosity^{44, 132}, or degradation due to chain breakup⁶⁵, to mention the most important ones.

Nevertheless, due to the fact that many polymer grades are relatively inexpensive, non-toxic and easy to handle, polymer solutions seem to be a fair compromise and are very popular for investigations into various kinds of viscoelastic effects, for example vortex shedding from a cylinder¹⁰⁴, disintegration of liquid drops^{34, 113, 114}, or elastic turbulence^{30, 59, 60}. The latter is a turbulent flow which develops in elastic fluids at very low Reynolds numbers, unlike turbulence in Newtonian fluids.

However, many of these materials exhibit shear-thinning, which is a reduction of the apparent viscosity with increasing shear rates. This makes it difficult to differentiate between shear-thinning, elastic and inertial effects. This becomes clear by considering the material functions for a simple shear flow in the x_1 - x_2 -plane¹⁸:

$$D_{12} = 2\mu(\dot{\gamma})S_{12}, \quad (2.1)$$

and the normal stress differences

$$N_1 = D_{11} - D_{22} = 4S_{12}^2\Psi_1(\dot{\gamma}), \quad (2.2a)$$

$$N_2 = D_{22} - D_{33} = 4S_{12}^2\Psi_2(\dot{\gamma}), \quad (2.2b)$$

where

$$D_{ij} = 2\mu(\dot{\gamma})S_{ij} = \mu(\dot{\gamma})\left(\frac{\partial U_i}{\partial x_j} + \frac{\partial U_j}{\partial x_i}\right), \quad (2.3)$$

is the deviatoric (or viscous) stress tensor. The viscosity μ is a scalar function and depends only on the shear stress magnitude¹⁸ of S_{ij} , that is,

$$\dot{\gamma} \equiv \sqrt{2S_{ij}S_{ji}}. \quad (2.4)$$

Thus, for a simple shear flow, $\dot{\gamma} = |S_{12}|$. (Note that, to avoid confusion with the Kolmogorov microscale, μ is used for the dynamic viscosity, non-Newtonian and Newtonian, instead of the more common symbol η .) Equations (2.1) and (2.2) illustrate that the viscosity is a first order function of the shear rate, and that the normal stress differences N_1 and N_2 , deriving from the elastic properties, are of the second order. The quantities Ψ_1 and Ψ_2 are called the first and the second normal stress coefficients, respectively. In consequence, elastic forces are small at low shear rates, and experimentally speaking, sufficiently high shear rates are necessary to generate elastic effects. But if shear-thinning is present, normal stresses can be difficult to measure.

An ideal elastic fluid with a constant viscosity would allow to separate viscous and elastic behavior. Such a fluid was suggested by Boger²¹, with the unique feature of a large relaxation time. But because of its high viscosity, it is difficult to handle and not suitable for flow configurations with large Reynolds numbers. Tam and Tiu¹³¹ presented highly elastic fluids with low viscosities, remaining constant over a wide range of shear rates. They also emphasize that the relaxation time—characterizing the elastic properties of a fluid—is dependent on the solvent viscosity, the molecular weight, the solvent quality, and the temperature. Thus, a low viscosity fluid with long relaxation times, which results in developed elastic effects, can be obtained with a high molecular weight polymer and a good solvent. An adequate choice is a water soluble polymer, with the additional feature of being transparent, and hence, allowing the investigation with optical measuring techniques.

The following sections will introduce the particular type of dilute polymer solutions, and specify its most important characteristics, such as the shear viscosity, the relaxation time, and the degradation in strong shear flows.

2.2 RHEOLOGICAL DESCRIPTION OF DILUTE POLYMER SOLUTIONS

Depending on the molecular weight, polymer solutions can develop non-Newtonian behavior at vanishingly low polymer concentrations, of the order $O(10^{-5})$, and these effects increase with increasing concentrations. One can easily imagine that the structure changes with the amount of polymers, from isolated polymer chains to large polymer networks. Graessley⁵⁸ introduced five distinguished regimes depending on the concentration and the molecular weight: (i) dilute solution with individual polymer coils; (ii) semi-dilute solution with individual chains; (iii) semi-dilute solution with polymer networks; (iv) concentrated solution with individual coils; and finally, (v) concentrated solution with networks. In regimes (ii) to (v), one differentiates between simple coil overlap, characterized by weak polymer-polymer

2.2 RHEOLOGICAL DESCRIPTION OF DILUTE POLYMER SOLUTIONS

interaction, and polymer chain entanglement where strong connections between coils exist. Viscoelastic properties of dilute solutions, and presumably also of non-entangled semi-dilute and concentrated solutions, are governed by isolated polymer chain dynamics, whereas in solutions of polymer entanglements, the network structure is predominant.^{47, 58}

The rather smooth transition from one regime to another is usually indicated by critical concentrations (and molecular weights), which should not be regarded as sharp separations but as rough indicators. The dilute regime (i), to which the solutions of the present study belong, is distinguished from the semi-dilute regime by the critical coil overlap concentration c^* . This value, is reached when the polymer molecules, assuming a tangled-ball configuration, are in dense spherical packing.⁸⁷ The size of the individual coils, and therefore also c^* , depends on several parameters, such as the molecular weight of the polymer and the solvent quality. Good solvents are characterized by weak inter-polymer forces and strong polymer-solvent interaction. The behavior is opposite for poor solvents. An idea of the magnitude of these interactions is given by the intrinsic viscosity $[\mu]$ defined as the contribution of the polymer to the solution viscosity as the polymer concentration approaches zero. Or more precisely, it is the limiting value

$$[\mu] = \lim_{c \rightarrow 0} \mu_{\text{red}} \quad \text{or} \quad [\mu] = \lim_{c \rightarrow 0} \mu_{\text{inh}} \quad (2.5)$$

of the reduced viscosity

$$\mu_{\text{red}} = \frac{\mu - \mu_s}{c\mu_s}, \quad (2.6)$$

or the inherent viscosity

$$\mu_{\text{inh}} = \frac{\ln(\mu/\mu_s)}{c}, \quad (2.7)$$

respectively, and where μ_s designates the solvent viscosity. Similarly to μ , $[\mu]$ is dependent on the shear rate¹⁸, and we define here $[\mu]$ to be the intrinsic viscosity measured at zero-shear.* In order to determine c^* , it is common to use the expression

$$c^* = \frac{1}{[\mu]}, \quad (2.8)$$

leading to the coil overlap parameter $c[\mu]$. An alternative definition of c^* is⁵⁸

$$c^* = \frac{0.77}{[\mu]}, \quad (2.9)$$

yielding a more restrictive critical concentration, but of the same order of magnitude. Both expressions figure in the literature^{105, 112, 136}.

In the present study, only the dilute regime (i) will be considered, such that the polymer concentration $c < c^*$. Therefore, viscoelastic effects are assumed to arise from single polymer chain behavior. It should be mentioned that in practice such

*In the literature, the zero-shear intrinsic viscosity is often denoted $[\mu]_0$.

idealized solutions may not exist, or only at very low polymer concentrations, such that $c[\mu] \ll 1$.

It has been observed that ‘fresh’ dilute solutions yield higher viscosities than aged solutions, and that the viscosity remains stable only after a few days of ageing.^{63, 70} Thus, one has to expect that even in aged solutions, small networks of entangled polymer molecules persist^{69, 136}, rather than dissolve to isolated polymer chains. Hence, the results of the turbulence experiment will have to be interpreted with this in mind.

2.2.1 MATERIAL FUNCTIONS AND DIMENSIONLESS GROUPS

In the present study, the two important material functions characterizing the polymer solution are the non-Newtonian viscosity $\mu(\dot{\gamma})$ and the polymer relaxation time τ . (As λ is reserved for the Taylor microscale, τ represents the polymer relaxation time.) The relaxation time is the characteristic time scale describing the viscoelastic properties. Large relaxation times indicate pronounced elastic effects, while small relaxation times characterize weak elasticity. The relaxation time being one important parameter, the development of viscoelastic effects also depends on the local time scales of a given flow configuration. This leads to the Weissenberg number which is equal to the product of the characteristic time scale of the fluid and the shear rate magnitude,

$$Wi \equiv \tau \dot{\gamma}. \quad (2.10)$$

It is a measure for the relation between the elastic forces of the polymers, and the viscous forces of the flow acting on the polymer coils.

Alternatively, in turbulent flows the Weissenberg number is given by the ratio between the polymer relaxation time and the characteristic time scale t_K of the smallest turbulence scales,

$$Wi \equiv \frac{\tau}{t_K}. \quad (2.11)$$

Viscoelastic behavior becomes noticeable when $Wi \gtrsim 1$, that is, when the relaxation time is comparable to the time scales of the turbulent flow.

2.2.2 MODELS FOR POLYMER SOLUTIONS

In order to analyze and synthesize rheological data, one has to adopt a model suitable for the problem at hand. A large variety of models are available, and two simple ones are the multi-mode Maxwell and the Rouse-Zimm model, which belong to the family of linear viscoelastic models. For the models employed here, only the necessary information will be given. More details can be found in references 18 and 19.

In experimental rheology, it is also customary to use empirical relations, for example the Carreau-Yasuda (CY) model (2.12), because of their ability to describe the measured data more closely than mechanistic models. Practically speaking, the Rouse-Zimm model predicts a constant solution viscosity, which is not the case for

2.2 RHEOLOGICAL DESCRIPTION OF DILUTE POLYMER SOLUTIONS

many polymer solutions, and the generalized Maxwell model has also a very limited capacity of describing shear dependent viscosities (illustrated in figure 2.7).

The shear-dependent viscosity can be very well fitted by¹⁸

$$\frac{\mu - \mu_\infty}{\mu_0 - \mu_\infty} = [1 + (\tau_{\text{CY}} \dot{\gamma})^{a_{\text{CY}}}]^{(n_{\text{CY}} - 1)/a_{\text{CY}}}, \quad (2.12)$$

where μ_0 and μ_∞ are the zero-shear rate and the infinite-shear rate viscosities, respectively. The quantity τ_{CY} is a pseudo time constant, and its reciprocal indicates the intersection of the zero-shear rate viscosity with the power-law region of slope $n_{\text{CY}} - 1$. The parameter a_{CY} allows to smooth the transition between these two regions.

Macroscopic linear viscoelastic behavior can be modeled by linear combinations of dashpots and Hookean springs, characterized by viscosities and relaxation times, respectively. A single Maxwell element consists of a dashpot connected in parallel with a spring. The superposition of N such elements, each with a different relaxation time τ_j and viscosity μ_j , allows to increase the complexity of the model

It is customary to investigate linear viscoelasticity with small amplitude oscillatory shears S_{12} at variable frequencies ω to determine the complex modulus

$$G^*(\omega) = \frac{D_{12}(t)}{2S_{12}(t)} = G'(\omega) + iG''(\omega). \quad (2.13)$$

G' and G'' are referred to as the elastic (or storage) modulus and viscous (or loss) modulus respectively. They are related to the discrete relaxation spectrum by

$$G'(\omega) = \sum_{j=1}^N \frac{\mu_j \tau_j \omega^2}{1 + (\tau_j \omega)^2}, \quad (2.14a)$$

$$G''(\omega) = \sum_{j=1}^N \frac{\mu_j \omega}{1 + (\tau_j \omega)^2}. \quad (2.14b)$$

The longest and most influential relaxation time is equal to the sum of all relaxation times τ_j , idem for the corresponding viscosity, that is,

$$\tau_{\text{M}} = \sum_{j=1}^N \tau_j, \quad (2.15a)$$

$$\mu_{\text{M}} = \sum_{j=1}^N \mu_j. \quad (2.15b)$$

In order to identify the N relaxation times and viscosities, one has to fit (2.14) to the measured moduli. This harbours the difficulty of a non-linear minimization problem. A procedure proposed by Jensen⁶⁷ involving a simulated annealing algorithm^{35, 56} was adopted to determine the relaxation spectrum.

The Rouse model is based on a necklace of N beads, producing viscous drag on the polymer, connected with $N - 1$ linear elastic and frictionless springs. Including the hydrodynamic interactions between the beads leads to the Rouse-Zimm

description of a polymer chain dissolved in a Newtonian solvent. This microscale model is very similar to the macroscale model of Maxwell. That is, it also consists of a linear superposition of elastic, and viscous units and has a spectrum of $N - 1$ relaxation times. The dominant relaxation time is given by¹¹²

$$\tau_z = \frac{1}{\zeta(3\beta)} \frac{[\mu]\mu_s M_v}{RT}, \quad (2.16)$$

where

$$\zeta(3\beta) = \sum_{i=1}^{\infty} \frac{1}{i^{3\beta}}$$

is the Riemann zeta function. The expression M_v denotes the *viscosity* average molecular weight (determined by means of the intrinsic viscosity and the Mark-Houwink relationship¹⁸), R is the universal gas constant, and T is the temperature in Kelvin. The parameter β denotes the solvent quality factor (which will be defined below, along with M_v).

2.2.3 DATA REDUCTION

Due to limitations of rheological instruments, data can be acquired only for relatively narrow ranges of shear rate and frequency. To overcome this handicap and extend the measured domains, tests are run on polymer solutions of various concentrations and at different temperatures. This leads to a relatively large amount of data spread over a wide parameter space. In order to correlate the data, viscosities, as well as storage and loss moduli, are shifted horizontally and vertically to overlap with one another.^{47, 132} Viscosity data are shifted according to

$$\hat{\gamma} = \dot{\gamma} \frac{T_{\text{ref}}}{T} \frac{\mu_0 - \mu_s}{\mu_0(T_{\text{ref}}) - \mu_s(T_{\text{ref}})}, \quad (2.17a)$$

$$\hat{\mu} = \mu \frac{\mu_0(T_{\text{ref}}) - \mu_s(T_{\text{ref}})}{\mu_0 - \mu_s}, \quad (2.17b)$$

where concentration differences are not compensated. Hence, only measurements of the same solution, but realized at different temperatures, can be reduced to a common curve. The shift factors for oscillatory shear data, on the other hand, do include a normalization for concentration:

$$\hat{\omega} = \omega \frac{M_v}{cRT} (\mu_0 - \mu_s), \quad (2.18a)$$

$$\hat{G}' = G' \frac{M_v}{cRT}, \quad (2.18b)$$

$$\hat{G}'' = G'' \frac{M_v}{cRT}. \quad (2.18c)$$

2.3 FLUIDS AND INSTRUMENTATION

Polymers exist in many types and molecular weights, and every grade has its own viscoelastic behavior. For our study we chose poly(ethylene oxide) (PEO) because of its low sensitivity to shear-thinning¹³², and its wide spread use for studies on drag reduction^{16, 40, 53, 121} and homogeneous turbulence^{10, 82–84, 93}. Polyox WSR 301, supplied by Dow, is a water soluble, flexible and polydisperse polymer with a nominal average molecular weight of 4×10^6 g/mol, a repeat unit mass of 44 g/mol and an average bond length of 0.147 nm. The polymer contour length is roughly 13.3 μm , which is much larger than the rms end-to-end distance of the unperturbed coil, namely 0.09 μm .¹⁰⁴

The Newtonian solvent for the turbulence experiment was filtered tap water, and distilled water was used to prepare the sample solutions for the polymer characterization. An average mass per unit volume of 998 kg/m³ was used for pure water, as well as for the polymer solutions.

2.3.1 PREPARATION OF SAMPLE SOLUTIONS AND TUNNEL FLUIDS

Small sample solutions of 200 g each were made by adding distilled water to a 0.5 wt% stock solution. The latter was prepared by sprinkling the dry polymer powder on the free surface of the water in a container, and was then gently mixed by means of a roller mixer for 24 hours. Subsequent storage for another week at 6 °C was necessary to obtain an optically homogeneous solution, before the dilutions were made. According to Kalashnikov⁷⁰, high concentration solutions attain stable fluid properties after approximately ten days. Hence, the residual stock solution, as well as the dilutions were left to rest during three more days before starting the rheological measurements. For storage they were kept in a refrigerator at 6 °C.

PEO solutions for the turbulence experiment were prepared by means of a five litre parent solution saturated with NaCl. The saturated NaCl solution is a non-solvent[†] and prevents the PEO to soak up water and build up large polymer blocks. This parent solution was poured, right after its preparation, into the flow facility filled with water. To promote spatial homogenization and avoid large agglomerations, the pump was running at full speed (≈ 40 litres/s) during this operation. The polymer-NaCl solution formed small droplets, which were nicely dispersed over the whole tunnel volume. The pump was then immediately slowed down to a few revolutions per minute, corresponding to $\approx 1\%$ of full speed, and was left running for three days. The fluids prepared in this manner were optically homogeneous after only one hour, and viscosity tests showed that they were stable four days later. This is very fast compared to the three weeks of homogenization that were necessary, when the dry polymer powder was sprinkled directly on the free water surface in the tunnel. No biocide was necessary for the polymer solutions, but one litre of bleach—which destroys any non-Newtonian effect within a few hours—was added to plain water experiments.

[†]A list of other possible non-solvents of Polyox can be found online on the Dow webpage.

The final salt concentration in the tunnel was less than 0.04 % by weight. No noticeable effect on the solution viscosity could be detected in test solutions with NaCl concentrations below 0.1 wt%. In fact, elastic and viscous moduli of a test solution dropped by less than 5 %, which is approximately equal to the error of the rheometer, and hence negligible. These conclusions are consistent with findings of other experimentalists^{86, 130, 133, 153}. In contrast to PEO, minute amounts of salt almost completely annihilate elastic effects in aqueous polyacrylamide solutions.^{55, 133} A more rigorous investigation would be necessary for a better understanding of the physico-chemical properties of PEO dissolved in weak NaCl solutions, which is beyond the scope of this work.

2.3.2 RHEOLOGICAL MEASURING SYSTEMS

In order to properly characterize the elastic fluids used for the turbulence experiments, a series of tests was conducted on small sample solutions covering a wide range of concentrations, $10 \leq c \leq 5000$ wppm[‡], and temperatures, $5 \leq T \leq 30$ °C. Steady shear and oscillatory shear measurements were realized on a Bohlin C-VOR 150 rheometer with a double-gap sample holder, or a cone-and-plate setup, respectively. A water jacket allowed to regulate the sample temperature between 5 ± 0.1 °C and 30 ± 0.1 °C. Due to the very small forces involved at low shear rates and the onset of the Taylor-Couette instability at high shear rates, the range of explorable shear rates was relatively narrow, that is, from roughly 0.05 to 300 1/s. Minimal scatter in the data was obtained when the rheometer was driven in the controlled stress mode. All measurements were run with at least one ‘up-and-down’ cycle (increasing shear stresses followed by a decrease) to verify that the properties of the tested sample remained stable. For steady shear tests, the same sample was tested at various temperatures, while for oscillatory shear tests, a fresh sample was used for each temperature. In any case, for a given polymer concentration the first measurement was repeated at the end. None of the tested samples did show any kind of evolution, and all measurements were perfectly repeatable during the whole measurement campaign carried out over the period of one month.

The kinematic viscosity was measured with an Ubbelohde capillary viscometer for solutions of concentrations below 1000 wppm, where solutions with more than 500 wppm were strongly affected by shear-thinning. To maintain the solution temperature at a constant value between 20 ± 0.1 °C and 25 ± 0.1 °C, the capillary was placed in a controlled water bath. In order to minimize the measurement uncertainty, an average was taken over nine runs with the same sample.

An accuracy of less than 5 % is guaranteed for the rheometer by the manufacturer, and viscosity measurements of distilled water, and 87 % glycerol gave an error of less than 2 % compared to literature values. Viscosities determined with the capillary viscometer were within 0.5 % of published values for distilled water.

[‡]Weight parts per million, denoted wppm, will be used as standard concentration unit throughout the report. Exceptionally, the concentration may be given in g/ml ($\approx 10^6$ wppm) or wt% ($= 10^4$ wppm).

2.4 CHARACTERISTICS OF THE WORKING FLUIDS

2.4 CHARACTERISTICS OF THE WORKING FLUIDS

The characteristics of the selected polymers following in this section were determined with the sample solutions, and are assumed to be transferable to the solutions prepared in the tunnel. One should keep in mind, that the solvent was of different quality, the sample solutions were prepared with distilled water and the tunnel fluids with tap water. It is further believed that the salt added to the tunnel solutions in combination with the stainless steel of the tunnel does not alter, by significant amounts, the solution properties. As will be seen in chapter 5, the salt probably caused a reduced polymer-solvent interaction, noticeable by a lower solution viscosity.

2.4.1 MOLECULAR WEIGHT AND COIL OVERLAP CONCENTRATION

The average molecular weight of Polyox WSR 301 was determined with the Mark-Houwink relationship

$$[\mu] = K M_v^{3\beta-1} = 0.072 M_v^{0.65}, \quad (2.19)$$

where M_v is the viscosity average molecular weight, β the solvent quality parameter and K a constant. The indicated prefactor and exponent were found by Tirtaatmadja et al.¹³⁶ to produce appropriate results for aqueous Polyox solutions with $8 \times 10^3 \leq M_v \leq 5 \times 10^6$ g/mol. The exponent $3\beta - 1 = 0.65$ yields a solvent quality parameter of 0.55, indicating that water is a relatively good solvent of PEO. The limiting values of β are 0.5, for a theta solvent, and 0.6 for a good solvent, denoting weak and strong polymer-solvent interaction, respectively.

Extrapolating the reduced viscosity and the inherent viscosity to zero concentration produces $[\mu] = 1625 \pm 55$ ml/g. This value coincides well with literature values for the same polymer grade (e.g., refs. 36, 71, 94, 100, 116, 132, 136), which vary between 1420 and 1860 ml/g. A plot of the data measured at 24 °C, including the linear regressions used for the extrapolation, is shown in figure 2.1. In order to verify the relation (2.5), the regressions were found simultaneously. The viscosities μ_{inh} and μ_{red} drop at concentrations below 100 wppm, a similar behavior was reported by Sylvester and Tyler¹³⁰. They speculate that the sudden change is possibly due to formation of polymer entanglements above this concentration.

Applying equation (2.19), we find an average molecular weight of 5.0×10^6 g/mol, which is 25 % higher than indicated by the supplier.

With the expression for the critical coil overlap concentration (2.8) one obtains

$$c^* = \frac{1}{[\mu]} \approx 615 \text{ wppm}, \quad (2.20)$$

or alternatively with (2.9)

$$c^* = \frac{0.77}{[\mu]} \approx 475 \text{ wppm}, \quad (2.21)$$

AQUEOUS POLY(ETHYLENE OXIDE) SOLUTIONS

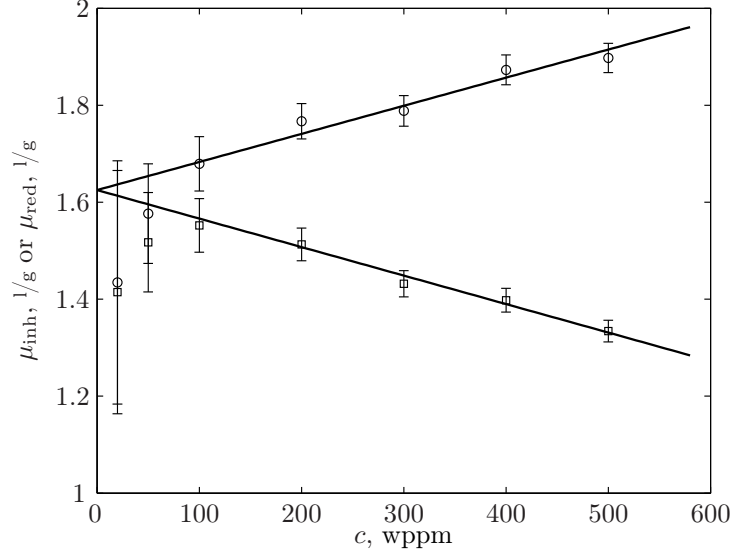


FIGURE 2.1 Inherent (\square) and reduced (\circ) viscosity plotted versus solution concentration. Linear fits (solid lines) were used to determine the intrinsic viscosity at $c = 0$.

for our PEO sample. The fluids for the turbulence experiment consisted of polymer concentrations of less than or approximately equal to 100 wppm, and were therefore considered to be dilute.

2.4.2 CONCENTRATION AND TEMPERATURE DEPENDENCE OF THE VISCOSITY

Zero-shear viscosities were measured for sample solutions with concentrations ranging from 10 to 5000 wppm at 24°C with the capillary viscometer or the rheometer. The relative viscosity μ_0/μ_s plotted against the polymer concentration, shown in figure 2.2, is well described by the general relation for a homogeneous solution^{18, 63}

$$\frac{\mu}{\mu_s} = 1 + c[\mu] + 0.5 (c[\mu])^2, \quad (2.22)$$

for concentrations below 1000 wppm (cf. broken line). An improved representation is

$$\frac{\mu}{\mu_s} = \left(1 + \frac{c[\mu]}{6.2} \right)^{6.2}, \quad (2.23)$$

which was fitted in the least squares sense (cf. solid line). For sample solutions with concentrations above 500 wppm, the capillary viscometer underestimates the zero-shear viscosity due to shear-thinning effects. Assuming a Poiseuille flow in the capillary tube, the maximum shear rate, occurring at the capillary wall, can be approximated by¹⁰⁴

$$\dot{\gamma}_{\max} = \frac{d\rho gh}{4\mu}. \quad (2.24)$$

2.4 CHARACTERISTICS OF THE WORKING FLUIDS

With a capillary diameter $d = 0.53$ mm, a total driving head $h = 16$ cm, $g = 9.81$ m/s², and $\rho = 998$ kg/m³, (2.24) yields $\dot{\gamma}_{\max} \approx 92$ 1/s for the 500 wppm solution, which has a zero-shear viscosity of 2.25 mPa.s. Although steady shear viscosity measurements at such low concentrations were difficult, shear-thinning could be detected for shear rates above 10 1/s.

In the dilute regime, far below 615 wppm, the discrepancy between the viscometer and the rheometer data may be explained with the measurement uncertainty of the rheometer at very low shear stresses. Another source of error is the fact that zero-shear viscosities were determined manually using log-log plots.

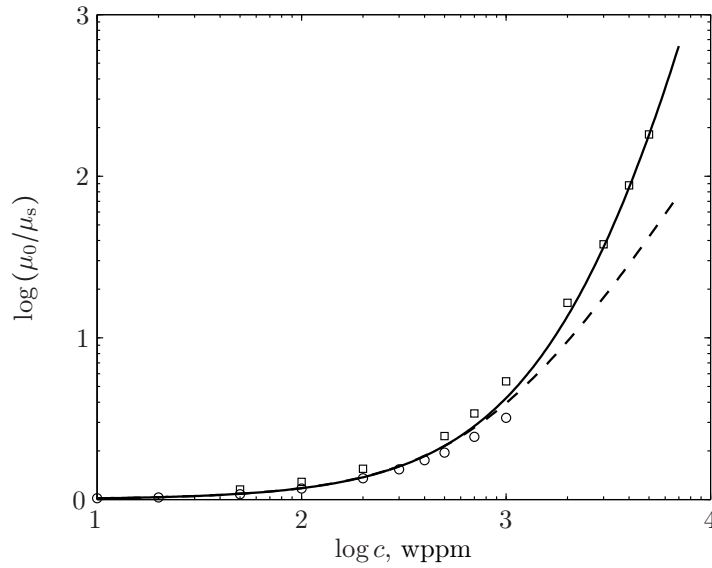


FIGURE 2.2 Zero-shear viscosity at 24 °C measured with the capillary viscometer (\circ) and the double-gap rheometer (\square). The solid and the dashed lines are defined by (2.23) and (2.22) respectively.

In order to determine accurately the solution concentrations used for the turbulence experiments, a simplified empirical relationship was derived from measurements of solutions of $c \leq 100$ wppm in the temperature range between 20 and 25 °C. Figures 2.3 (a) and 2.3 (b) are the required plots for the relations

$$\mu(c, T) = \mu_s(T) (1 + c[\mu]), \quad (2.25a)$$

$$\mu(c, T) = \mu(c, T_{\text{ref}}) (1 - 0.023 [T - T_{\text{ref}}]), \quad (2.25b)$$

which are drawn as solid lines. These two expressions provide a simple implement to verify the concentration of the fluids used for the turbulence experiments.

2.4.3 SHEAR DEPENDENT VISCOSITY

Shear-thinning is accurately describe by the model (2.12). Applying the shifting technique mentioned earlier to the steady shear data, separated by concentration,

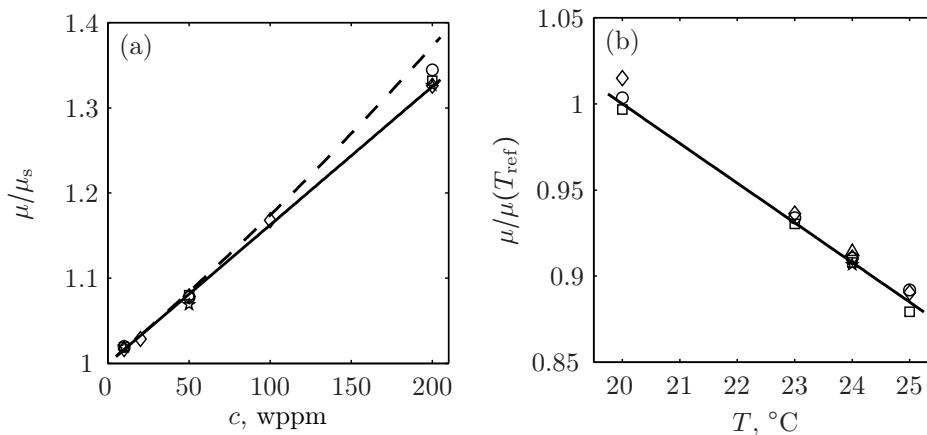


FIGURE 2.3 Concentration and temperature dependence of the zero-shear viscosity. (a): \circ , 20 °C; \square , 23 °C; \diamond , 24 °C; and \star , 25 °C. (b): \circ , 10 wppm; \star , 20 wppm; \square , 50 wppm; \triangle , 100 wppm; and \diamond , 200 wppm. The linear regressions (2.25a) and (2.25b) are indicated by solid lines. The dashed line shows the relative viscosity computed with (2.23).

reduced shear viscosity curves covering at least four decades of shear rates were obtained. Individual Carreau-Yasuda models were fitted to each reduced curve, where the zero-shear viscosities have been previously determined from the raw data. The infinite-shear viscosity μ_∞ was taken to be equal to the Newtonian solvent viscosity μ_s , although $\mu_\infty = 0$ is more commonly used. This is justified considering that the difference between μ_s and zero is negligible for high polymer concentrations, but it is not for low concentrations. Furthermore, μ_∞ is more likely to approach a value $\gtrsim \mu_s$ than zero.

All the $\mu(\dot{\gamma})$ curves were reduced with respect to the 5000 wppm data set, using the reference values $T_{\text{ref}} = 293$ K, $\mu_s(T_{\text{ref}}) = 1.002$ mPa s and $\mu_0(T_{\text{ref}}) = 202.0$ mPa s. As an example, the reduced data for the 5000 wppm solution and the corresponding model curve are plotted in figure 2.4.

The low shear data deviates from the zero-shear rate plateau due to the incapacity of the rheometer to measure the very small forces. Instrument tolerance boundaries⁹¹ for the controlled-stress rheometer were calculated assuming that the only corrupted quantity is the measured shear-rate, and the error boundaries indicated in figure 2.4 correspond to an error of 3 1/s. Otherwise the data overlaps very nicely, and the model curve is flexible enough to capture the transition.

The determined values for $n_{\text{CY}} - 1$ and τ_{CY} showed some dependence on the solution concentration, whereas the transition parameter a_{CY} was invariant. According to Pipe and Monkewitz¹⁰⁵ and Stadler et al.¹²⁷ $a_{\text{CY}} = a_{\text{CY}}(M_v)$, and since this is a property of the polymer itself and not the solution, it seemed appropriate to force $a_{\text{CY}} = 1.2$ for all fits.[§] With the purpose of being able to extrapolate the

[§]Pipe and Monkewitz¹⁰⁵ stipulate that $0 < a_{\text{CY}} \leq 2$ for polydisperse materials, whereas Stadler

2.4 CHARACTERISTICS OF THE WORKING FLUIDS

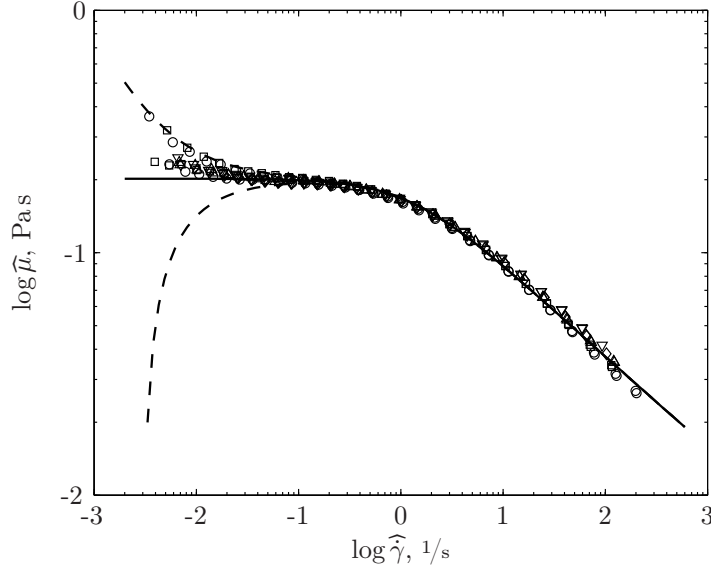


FIGURE 2.4 Shifted viscosity plotted against shifted shear rate for a PEO solution of 5000 wppm at various temperatures: \circ , 5 °C; \square , 10 °C; \star , 20 °C; \diamond , 24 °C; and \triangle , 30 °C. The solid line shows the fitted CY model (2.12), and the dashed lines mark the rheometer error boundaries.

CY model to very low concentrations, $n_{\text{CY}} - 1$ and τ_{CY} have to be replaced by functions of μ . The required plots are presented in figure 2.5 and the functions are

$$\tau_{\text{CY}} = 1.3 - 100\mu, \quad (2.26a)$$

$$n_{\text{CY}} - 1 = -(0.1 + 12\mu^{0.7}). \quad (2.26b)$$

Equation (2.26b) takes into account the limiting value $n_{\text{CY}} - 1 = 0.1$ for infinitely dilute solutions¹⁸.

After injecting these expressions into (2.12), rescaling $\hat{\gamma}$ and replacing $\mu_0(T_{\text{ref}}) - \mu_s(T_{\text{ref}})$ by its numerical value, namely 0.201 Pa s, one finds the function for the shear viscosity

$$\mu(\dot{\gamma}, c, T) = \mu_s + (\mu_0 - \mu_s) \left[1 + \left\{ (1.3 - 100c) \frac{293}{T} \frac{\mu_0 - \mu_s}{0.201} \dot{\gamma} \right\}^{1.2} \right]^{(n_{\text{CY}} - 1)/1.2}, \quad (2.27)$$

where

$$\frac{n_{\text{CY}} - 1}{1.2} = - \left(\frac{1}{12} + 10c^{0.7} \right).$$

In figure 2.6, expression (2.27) is illustrated by the solid lines successfully modelling the measured data. But this expression also allows to predict, or at least

et al.¹²⁷ show that, at least for polyethylene, a_{CY} does not depend on the polydispersity.

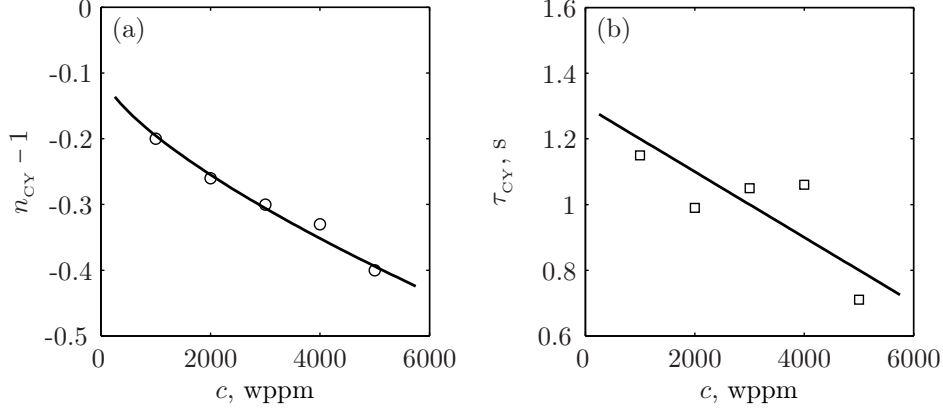


FIGURE 2.5 Fitted CY model parameters: (a) $n_{\text{CY}} - 1$; (b) τ_{CY} . The solid lines correspond to (2.26a) and (2.26b).

gives a rough picture of, the shear-thinning of the fluids used during the turbulence experiments. An example is indicated by the curve ①, which corresponds to a 100 wppm solution.

With the Cox-Merz rule, oscillatory shear data can be directly compared to steady shear measurements, that is, $\mu(\dot{\gamma}) = |\mu^*(\omega)|_{\omega=\dot{\gamma}}$ for small shear rates and frequencies, respectively.¹¹ In figure 2.7 such a superposition is made for the 4000 wppm PEO solution measured at 20°C. At the low shear rate and frequency end the data collapse quite well, while at the other end the dynamically measured data drops faster, which was also found in reference 18.

In terms of the complex modulus, the complex viscosity is given by

$$|\mu^*| = \frac{|G^*|}{\omega}, \quad (2.28)$$

and in conjunction with equations (2.14) and (2.18), the shear viscosity can be deduced from the generalized Maxwell model. It was done so for the data in figure 2.7, where the solid line represents (2.28) computed for a two-mode Maxwell model. Two modes are certainly not enough to fully capture the complex behavior of the polymer solutions, but the number of modi is limited by the window of measurable frequencies. (A thorougher description of the fitted Maxwell modes will be given below.) Nevertheless, the figure 2.6 demonstrates that the CY model is more effective to describe shear dependent viscosity.

2.4.4 RELAXATION TIME

Two different approaches to determining the polymer relaxation time have been introduced in a foregoing section. One involves the measurement of the bulk behavior under small oscillatory displacements, whereas the other can be computed solely from the intrinsic properties of the polymer-solvent system. The latter, called the

2.4 CHARACTERISTICS OF THE WORKING FLUIDS

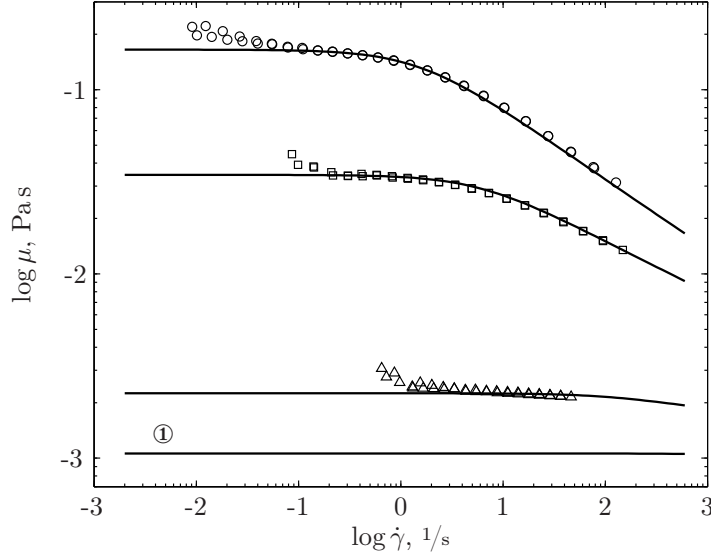


FIGURE 2.6 Rescaled CY model (solid lines) for solutions at 24 °C: Δ , 500 wppm; \square , 3000 wppm; \circ , 5000 wppm. The curve ① indicates the predicted behavior for a 100 wppm solution.

Zimm relaxation time, is defined by equation (2.16), and $\tau_z = 1.39$ ms, where the previously obtained values $[\mu] = 1625$ ml/g and $M_v = 5 \times 10^6$ g/mol at 297 K have been injected. The appropriate solvent viscosity is 0.911 mPa s and $R = 8.314510$ J/mol K.

By fitting the N -mode Maxwell model (2.14) to the measured storage and loss moduli, one can deduce τ_M . Only the thickest solutions produced measurable forces, and hence data was acquired for solutions with 3000 to 5000 wppm of PEO, in the temperature range between 5 and 30 °C. The number of possible modes essentially depends on the span of measured frequencies, which reached from $2\pi \times 10^{-2}$ to 4π rad/s. The j -th relaxation time, $j = 1 \dots N$, is limited by the inverse of the maximum and the minimum frequencies. It was found that with three modes the smallest relaxation times were bound by the limits, and in consequence the next lower model was considered, that is, the two-mode model. Figure 2.8 shows the model curves on top of the reduced moduli \widehat{G}' and \widehat{G}'' .

Rescaling the relaxation times computed for the reduced moduli according to relation (2.18), and making use of equation (2.23), yields

$$\tau_M = \mu_s \left[\left(1 + \frac{c[\mu]}{6.2} \right)^{6.2} - 1 \right] \frac{M_v}{cRT} \sum_{j=1}^2 \widehat{\tau}_j, \quad (2.29)$$

where

$$\sum_{j=1}^2 \widehat{\tau}_j = 1.227 \times 10^{-5}$$

is the total relaxation time of the fitted model. A plot of this function is given in

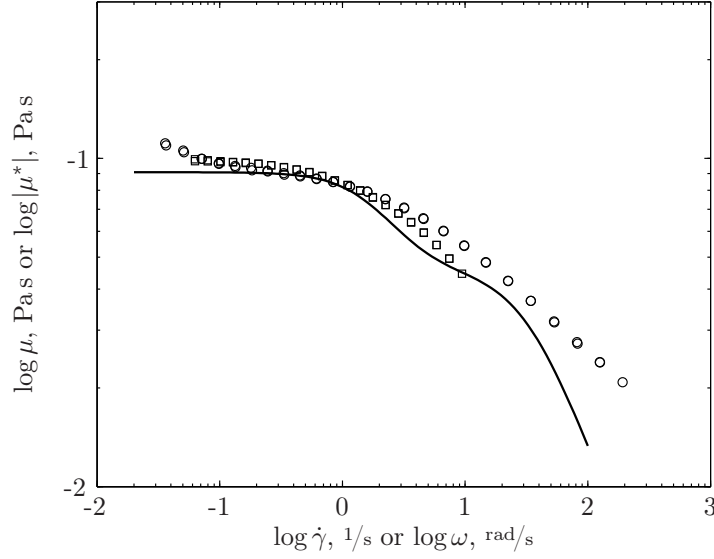


FIGURE 2.7 Superposition of the steady shear viscosity μ (\circ) and the complex viscosity $|\mu^*|$ (\square) of a 4000 wppm PEO solution at 20 °C. Shear-thinning is coarsely described by a two-mode Maxwell model (2.28) (solid line).

figure 2.9, emphasizing that the Maxwell relaxation time depends on the solution concentration.

Comparing the Maxwell relaxation time to the Zimm relaxation time (cf. figure 2.9), one immediately sees that there is a difference of at least one order of magnitude. One should note here, that τ_M was extrapolated over two decades towards the very low concentration region.

Rozhkov et al.¹¹³ determined the empirical relationship

$$\tau_R = 3.68 \times 10^{-4} c^{0.688}, \quad (2.30)$$

between the relaxation time and the polymer concentration in wppm, for a similar PEO grade with a molecular weight of 4×10^6 g/mol. For a 100 wppm solution this yields a relaxation time of 8 ms, which is larger but still comparable to the Zimm relaxation time.

All three estimates of the polymer relaxation time τ (i.e., τ_Z , τ_M and τ_R) are given in figure 2.9, which emphasizes the dependence of τ on the selected model. Intuitively, the molecular description of the polymer-solvent system by Zimm seems to be the appropriate choice, although the directly measured relaxation time of Rozhkov et al.¹¹³ indicates a dependence on the polymer concentration.

In addition to these estimates, figure 2.9 also indicates the relaxation times τ_p deduced from the Lumley scale ℓ_p ($\sim \sqrt{\epsilon \tau_p^3}$, where ϵ is the turbulence energy dissipation rate) of the non-degraded polymer solutions. This scale roughly indicates the turbulence scale at which the local (in terms of length scales) Wi is in the vicinity of one. (The Lumley scale will be properly introduced in chapter 5.)

2.4 CHARACTERISTICS OF THE WORKING FLUIDS

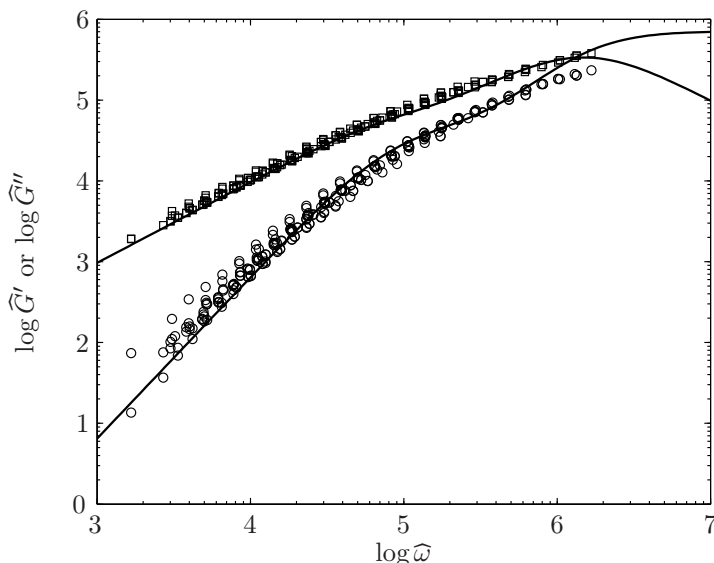


FIGURE 2.8 Reduced elastic and viscous moduli \widehat{G}' , \circ , and \widehat{G}'' , \square , with fitted tow-mode Maxwell model (solid lines).

These values are even larger than the Maxwell relaxation times, and also grow with increasing polymer concentration. The discrepancy between this estimate and the preceding approximations may have different causes: instead of individual polymer coils, polymer networks with larger relaxation times may have formed in the solution; the salt added during the solution preparation altered the polymer-solvent interaction; or the polymer relaxation is not linear, but depends on more than one relaxation time. Another possible explanation will be put forward in section 5.4.

2.4.5 RESISTANCE TO MECHANICAL DEGRADATION

Polyox WSR 301 can be qualified as one of the most effective drag reducers, but also the most liable to mechanical degradation.¹⁴⁰ An alternative choice to PEO is polyacrylamide, which was reported to be more resistant to mechanical degradation^{32, 40, 140}, but suffers from shear-thinning¹³².

That high molecular weight polymers are indeed very sensitive to strong shear flows, was shown mainly in rotating disk rheometers^{32, 36, 74, 129}, and a few other geometries^{20, 22, 144}. The only way to avoid mechanical degradation of the polymer coils is to avoid flows with excessive shear rates. Unfortunately, in the flow facility used for this study are many sources of high shear rates, other than the large velocity gradients in the turbulent flow itself. The grid used for the turbulence generation is probably the most important. In its boundary layers shear rates are estimated to at least one order of magnitude larger than the shear rates in the bulk far away from the grid, namely $O(10^4)$ 1/s. Moreover, from turbulent flows in various rheological devices, it was concluded that polymers are the most

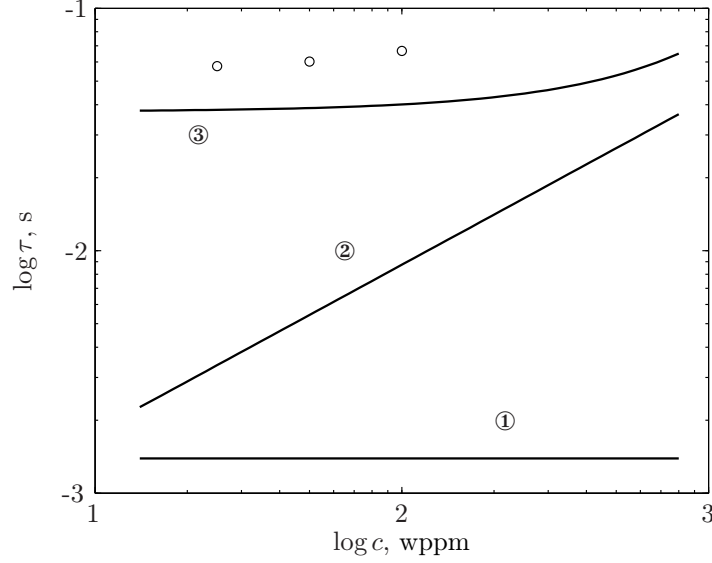


FIGURE 2.9 Estimates of the polymer relaxation time: ①, Zimm relaxation time (2.16); ②, empirical fit (2.30) by Rozhkov et al.¹¹³; ③, total Maxwell relaxation time (2.29); ○, relaxation time derived from Lumley scale for polymer solutions used in the turbulence experiments (cf. chapter 5).

vulnerable to scission when the ratio between the polymer contour length and the Kolmogorov scale is close to three.¹⁴⁴ This ratio was roughly 0.15 in the present study, which suggests that the turbulent flow behind the grid contributed very little to the polymer degradation.

However, heavy polymer degradation was observed during the turbulence experiments in polymer solutions, which will be further discussed in chapter 5.

2.5 FINAL REMARKS

Shear-thinning appears to be negligible even at high shear rates for the solution concentrations studied in the turbulence experiments, that is, 25, 50 and 100 wppm (cf. figure 2.6). Consequently, observed non-Newtonian behavior of the investigated turbulent flows can be attributed to elastic effects.

Regarding the fluid elasticity, relation (2.30) represents the result of directly measured relaxation times, and is considered to be a more ‘realistic’ characterization than the Zimm or the Maxwell relaxation time. Moreover, this relaxation time is representative only for the initial polymer solution, because during the turbulence experiments the polymers were heavily degraded and the fluid elasticity diminished. Due to the lack of a measurement technique allowing to measure the relaxation time accurately, approximate elastic properties of the degraded solutions were determined from the Lumley scale.

CHAPTER 3

Experiment setup and data processing

3.1 CLOSED-LOOP FLOW FACILITY

To study the influence of an elastic fluid on grid generated turbulence, we used the flow facility at EPFL* originally built to investigate the cylinder wake in an elastic fluid^{104, 105}. A few modifications were necessary, in order to accommodate turbulence grids of various geometries and to extend the streamwise distance from the grid. The facility is depicted in figure 3.1. It consists of a horizontally aligned recirculating tunnel made of stainless steel and with a capacity of roughly 3 600 liters. Its cross-section is mainly 600 by 600 mm and the central line following the flow direction has a length of 11.4 m.

In order to reduce the mechanical destruction of the dissolved polymers, the fluid is driven by a *bladeless* pump[†], similar to the one described by Den Toonder et al.⁴⁰. The pump is situated close to the downstream end of the test section (TS). It allows to vary the mean flow velocity U_0 , in the TS from a few millimeters per second to approximately 10 m/s.

There is a free surface downstream of the pump, roughly occupying a fourth of the loop, which was particularly useful during the polymer solution preparation. A settling chamber upstream of the 12:1 contraction is equipped with a honeycomb, separated by one hydrodynamic diameter (i.e., 600 mm) from the contraction, in order to straighten the flow and suppress streamwise vorticity of the fluid. Another honeycomb is installed 600 mm ahead of the TS exit in the diffuser. Both honeycombs have a cell diameter to cell length ratio of 16. This is well above the recommended⁹⁵ 7 to 10, but the flow straighteners performed satisfactorily.

The test volume, illustrated in figure 3.2, has a rectangular cross-section of width $W = 150$ mm and height $H = 200$ mm and a length of one meter. It is equipped with a chimney covering the whole top surface and allowing to access the TS without emptying the flow tunnel. All four lateral walls, including top and bottom, have 30 mm strong plexiglas windows for good optical access on a length of 920 mm. The turbulence grids are mounted 60 mm from the TS entry, leaving

*Ecole Polytechnique Fédérale de Lausanne, Laboratoire de Mécanique des Fluides.

[†]Parallel discs are oriented normal to the rotation axis and entrain the fluid by friction. Also called Tesla pump or disc pump.

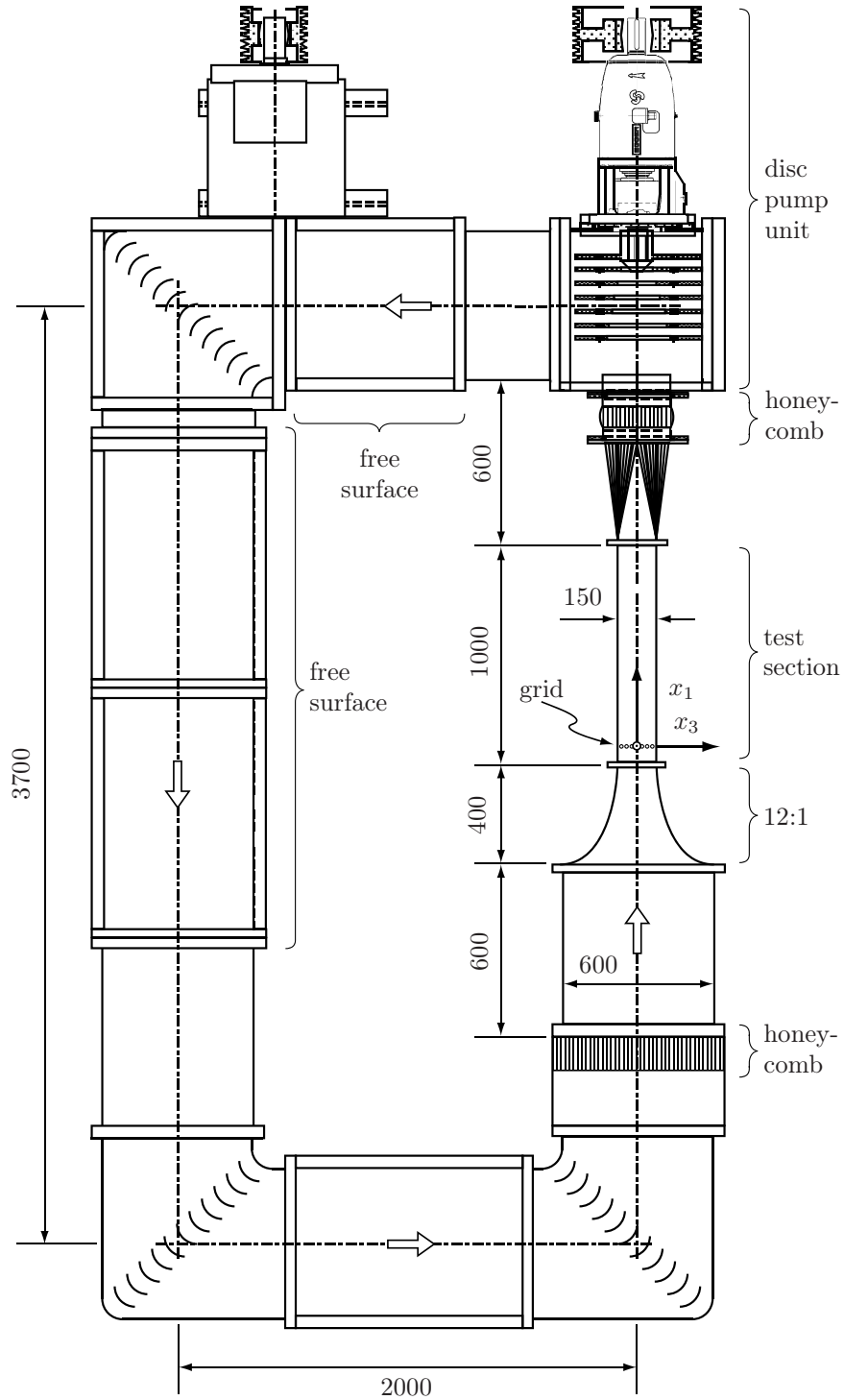


FIGURE 3.1 Overview of the closed-loop flow facility indicating its dimensions in millimeters. The large arrows point in the flow direction.

3.1 CLOSED-LOOP FLOW FACILITY

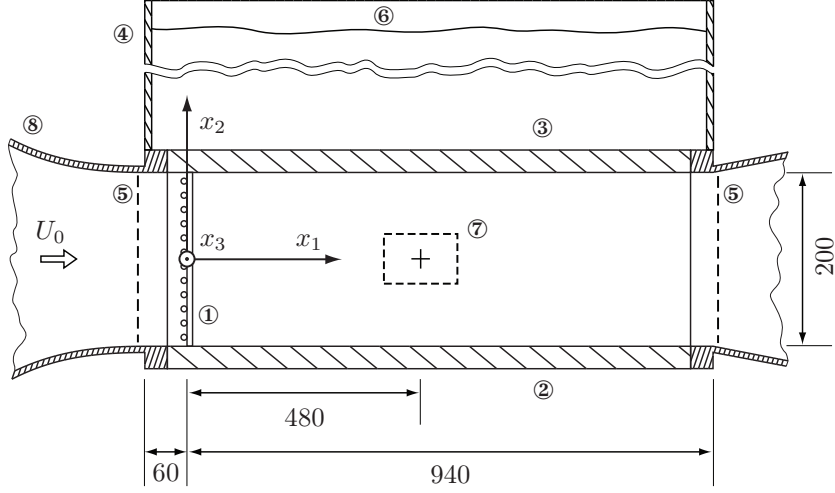


FIGURE 3.2 Schematic representation of the TS: ①, turbulence grid; ②, bottom window; ③, removable top window; ④, chimney; ⑤, sections with pressure taps; ⑥, free surface; ⑦, PIV area; ⑧, 12:1 contraction. Dimensions in millimeters.

an explorable distance of 900 mm behind the grid, which is equivalent to $56 M$ (M is the mesh width of the turbulence grid introduced in the next section).

All coordinates are given relative to a coordinate system centered on the grid and with its x_1 -, x_2 - and x_3 -axis aligned with the flow direction, the vertical and the horizontal grid rods, respectively (cf. figure 3.2).

An attempt was made to add a slight contraction downstream to reduce the inherent anisotropy of grid generated turbulence, as was suggested by Comte-Bellot and Corrsin³³ and Uberoi and Wallis¹³⁸, or more recently by Antonia et al.⁵. Molded plexiglas windows formed a contraction with an area ratio of 1.38 to ‘correct’ an estimated anisotropy level of $\approx 25\%$. The contraction ratio was determined with Batchelor’s¹² relations for a rapid distortion of a turbulent field. Unfortunately, the resulting turbulence isotropy gained shortly after this contraction, was not preserved further than 25 grid meshes from the grid. Another consequence of this contraction was the inferior PIV image quality due to the increased thickness of about 30 % of the plexiglas windows. Hence, flat windows were used for the entirety of the experiments presented here.

The free-stream quality of the flow through the TS was measured with LDA and for water only. As shown in figure 3.3 (a), the spanwise profiles of the average velocity \bar{U}_1 ($\bar{U}_i = \langle U_i \rangle$) has a ‘top-hat’ shape, and neither the elbows, nor the pump have an asymmetric effect. Idem for the longitudinal, u'_1/U_0 , and lateral, u'_2/U_0 , turbulence levels. They are below 1 % for a large portion across the TS before they increase close to the walls (cf. figure 3.3 (b)). In the streamwise direction, the mean free-stream velocity increased linearly by about 3 % between 5 and 42 M downstream of the grid, which corresponds to an increase of 5 % over the entire length of the working section. During the turbulence experiments, the longitudinal

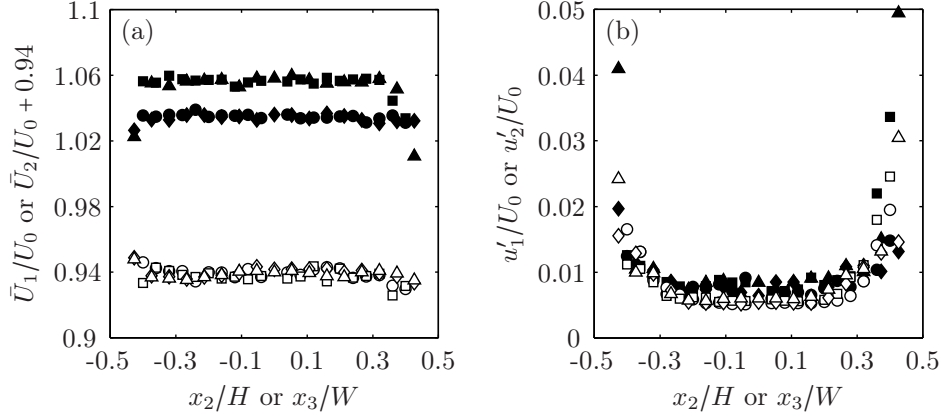


FIGURE 3.3 Free-stream quality. Horizontal (diamonds and triangles) and vertical (circles and squares) transverse profiles of (a) the mean velocity and (b) the rms velocity at two different streamwise locations: circles and diamonds, $x_1 = 20 M$; squares and triangles, $x_1 = 43 M$; solid symbols, x_1 -velocity component; open symbols, x_2 -velocity component. Note the offset of \bar{U}_2/U_0 .

mean velocity grew with the square root of the distance to the grid by roughly 3.5 % in the region $10 \leq x_1/M \leq 56$.

3.2 TURBULENCE GRIDS

A classic plain grid, hereafter referred to as reference turbulence grid (RTG), was used to measure the quality of our experimental setup with respect to similar experiments realized by others, as well as reference for comparison with the improved turbulence grid (ITG).

The RTG is composed of a biplane grid with square meshes and round rods. Its mesh width M is of 16 mm and the rod diameter d of 3 mm, resulting in a solidity of 34 %. Occupying the entire cross section of the TS, the grid is made of 8 by 11 whole meshes distributed symmetrically. In order to compare different grid turbulence experiments, it is customary to work with the grid based Reynolds number, defined as

$$Re_M \equiv \frac{MU_0}{\nu}. \quad (3.1)$$

The grid mesh is comparable to the turbulence injection scale, and hence, Re_M is generally two to three orders of magnitude larger than Re_λ .

We designed a new turbulence grid which consists of a plain grid identical to the RTG and tethered spheres attached to the grid nodes. Photographs of the ITG are shown in figure 3.4.

Various spherical beads with diameter D^* ($= D/M$), and relative density m^* ($= \rho_b/\rho$), have been studied in order to find an effective combination. Table 3.1 summarizes all tested grids. Note that only the ITG is fully occupied, that is,

3.2 TURBULENCE GRIDS

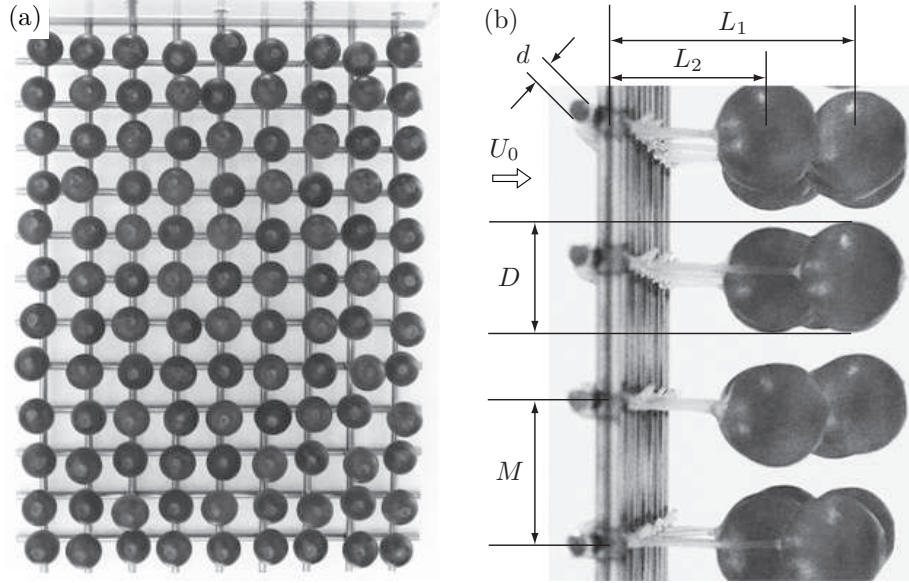


FIGURE 3.4 (a) front and (b) side view of the new passive grid with tethered spheres (ITG), indicating the main parameters.

TABLE 3.1 Test grids with tethered spheres. Diameters and lengths are normalized with $M = 16$ mm and the densities are given relative to $\rho = 998 \text{ kg/m}^3$.

Grid	Bead material	D^*	m^*	L_1^*	L_2^*	Grid node occupation, %
RTG	—	—	—	—	—	—
ITG	wood	0.75	0.7	1.35	1.0	100
W12	wood	0.75	0.7	1.35	1.0	65
W8	wood	0.50	0.7	1.35	1.0	65
W6	wood	0.37	0.7	1.35	1.0	65
G6	glass	0.37	2.4	1.35	1.0	65

one tethered bead for each of the 9 by 12 nodes; whereas for the other test grids the outermost rows and columns were vacant (i.e., 7 by 10 occupied nodes). This was chosen to reduce manufacturing time, and the resulting flow properties were satisfactory for the evaluation of the grid performance. The tethers are made of flexible silicone tubes of lengths L_1^* ($= L_1/M$) and L_2^* ($= L_2/M$), which were the same for all grids, and an outer diameter of 1 mm. A staggered arrangement of the beads (cf. figure 3.4 (b)) allows for larger oscillation amplitudes and a lower blockage ratio.

To obtain a rough idea about the nature of the tethered bead motion, a small test array of three by three W6 beads ($D = 6$ mm) attached to a plain grid was installed in a water flow with $U_0 = 1.0$ m/s. The trajectory and the vertical power spectral density function (psd) were obtained from a sequence of images taken with a Photron high-speed camera at 500 frames per second. The recording time was two

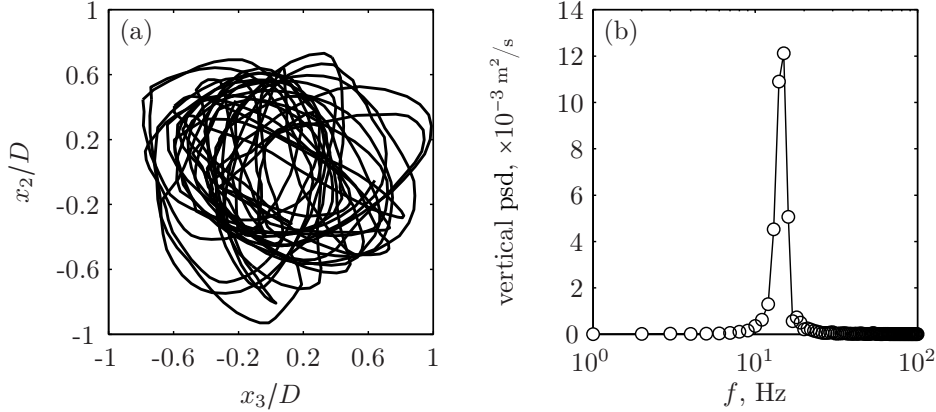


FIGURE 3.5 Bead motion in a steady flow with $Re_M = 1.6 \times 10^4$: (a) trajectory during a period of 2 s and (b) power spectrum of the vertical velocity. Data for the central bead of a 3×3 test array with $D = 6$ mm, $L_1 = L_2 = 40$ mm and $M = 16$ mm.

seconds. Figure 3.5 shows the trajectory and the spectrum of the central bead. The maximum amplitude response is of about 0.9 bead diameters, which is in agreement with Williamson and Govardhan¹⁵¹, and Govardhan and Williamson⁵⁷. Despite the chaotic trajectory, the spectrum emphasizes a single, relatively narrow peak, located at roughly 15 Hz, which is equivalent to a Strouhal number $St (\equiv fD/U_0)$, of 0.09. This is slightly less than half of the Strouhal number generally observed for vortex shedding from a stationary sphere.^{99, 151}

3.3 DIFFERENTIAL STATIC PRESSURE MEASUREMENT

Three cross-sections of the facility are equipped with four symmetrically positioned pressure taps each (cf. figure 3.2): the first is at the contraction inlet (not indicated on the figure), the second is between the contraction and the test section, and the third is at the TS outlet. Optionally, one could replace the low pressure intake at the TS exit with a Pitot-static tube mounted on the centerline $11M$ ahead of the grid. Two differential pressure transducers (Validyne DP15TL) measured the pressure drop at the large contraction, which provides the mean bulk velocity U_0 , and in the test volume, respectively.

Recordings for the pressure drop at the different grids were taken at a sampling rate of 2 kHz and averaged over 50 seconds for each mean flow velocity U_0 studied. During the turbulence experiments in polymer solutions we also monitored the evolution of the pressure drop across the test section. This data was sampled at a rate of 1 kHz during one hour.

Pressure measurements with transducers that are not flush-mounted are somewhat problematic when the working fluid is viscoelastic.¹¹ The pressure bias is proportional to the first normal stress difference¹⁸, which was too weak to be mea-

3.4 HOT-FILM ANEMOMETRY

sured with the available rheometer. Without any further proof, it was assumed that the error is negligible. However, the standard deviation of the pressure measurement in water and polymer solutions could be as large as 9% of the mean pressure, which in all likelihood outweighs this effect.

3.4 HOT-FILM ANEMOMETRY

Hot-film and hot-wire anemometry has been used extensively for the estimation of turbulence statistics in air and water²⁶, whereas in polymer solutions, anomalous measurements have been reported in various papers, see for example Piau¹⁰³, or Smith et al.¹²³. According to Friehe and Schwarz⁵¹, the main effect of polymers on cylindrical hot-film anemometry (HFA) probes is a strongly modified heat transfer; and Barenblatt et al.⁹ actually used this abnormal behavior to investigate the structure of aqueous polymer solutions. Nevertheless, Virk et al.¹⁴⁶ reported turbulence energy spectra for dilute polymer solutions measured in a pipe flow, using hot-film probes and an in situ calibration.

In order to avoid trouble due to possible misinterpretation of data, no measurements were realized with the HFA in polymer solutions, and it was only used to acquire reference data in water.

3.4.1 HFA DATA ACQUISITION

Longitudinal one-dimensional turbulence spectra have been acquired with a hot-film anemometer from TSI consisting of a single film probe (1210-20W) with a sensitive length $l = 1$ mm, and an analog analyzer (IFA 100). The film was oriented normal to the flow, and the probe holder had an angle of 50° to the flow direction. All HFA spectra correspond to a location close to the center of the TS cross section, 30 mesh widths downstream of the grid.

The analog HFA signal was low-pass filtered with a cut-off frequency of 5 kHz to avoid aliasing, well above the Kolmogorov frequency $f_K (\equiv U_0/2\pi\eta)$ which is of the order of 2 kHz. A dedicated computer then digitized the filtered signal at a sampling rate of 20 kHz during an interval of 400 s. This allowed to resolve both ends of the turbulence spectrum. In order to increase the signal to noise ratio, the signal was either high-pass filtered at 0.1 Hz, or off-set by an appropriate voltage, before amplified.

We used two different calibration procedures for the hot-film probe, both in situ: for early experiments, we used a standard calibration method²⁷ by fitting a function of the form $g^2(\bar{U}_1) = a_0 + a_1\bar{U}_1^b + a_2\bar{U}_1^{2b}$ to measured voltages $g(\bar{U}_1)$ for velocities \bar{U}_1 ranging from 0.05 to 2.0 m/s. The parameters a_0 to a_2 and b were found with a least-squares method. Simultaneously to the voltage recording, we measured the mean velocity close to the HFA probe with laser Doppler anemometry (LDA), which is more accurate than using the mean velocity derived from the static pressure difference at the contraction.

Calibrating the probe in this manner was time consuming and had to be done for at least every test series, due to probe contamination⁶⁸. Thus, for later test series, we adopted a local calibration technique, where we applied a quadratic relation to five calibration points taken in the vicinity of the actual measuring point. This proved to be a valid approach, considering that the fluctuating velocities are very small compared to the total velocity range necessary for a standard calibration. Accordingly, no significant deviations from older data were observed. Moreover, we repeated the five point calibration before and after each spectrum measurement, in order to verify if the recording has suffered from an important calibration drift. In such cases the measurement was repeated.

3.4.2 VELOCITY SPECTRA AND RMS

A total of 8×10^6 samples in one large set was available for the turbulence spectrum estimation. Spectra were calculated for data blocks of 2×10^5 samples, which yields a frequency resolution of 0.1 Hz. Block averaging and a 50 % overlap of subsequent blocks reduced the variance of the estimate. The 95 % confidence intervals were typically within 20 % of the mean spectrum.

Despite the low-pass filtering during the recording, the resulting spectrum was polluted by high frequency noise generated by the power supply of the pump, as well as resonance peaks, supposedly emerging from a fluid-probe interaction. Unfortunately, this was unavoidable. The affected frequency range lay in the far dissipation region, above ≈ 2 kHz and was cut off by digital low-pass filtering the recorded signal at 1.3 kHz. Hence, the spectrum does not completely resolve the dissipation region.

By invoking Taylor's hypothesis⁶⁴ (i.e., $\kappa_1 = 2\pi f/\bar{U}_1$), the obtained frequency spectrum $\phi_{11}(f)$ was then converted to the wavenumber spectrum $\phi_{11}(\kappa_1)$, from which the two-point correlation function $B_{11}(r_1)$ was derived.

Although hot-films and hot-wires are the preferred instruments for the estimation of higher order statistics, they have a severe impact on the measured spectrum. In the present experiments, the sensitive length of the hot-film is several times larger than the smallest scales of the flow, and consequently, these scales will be significantly underestimated. One can consider the measured velocity field to be the actual velocity field low-pass filtered by a rectangular window, whose spectral counterpart is a cardinal sine function,

$$\chi(\kappa_2) = \frac{\sin(\kappa_2 l/2)}{\kappa_2 l/2}, \quad (3.2)$$

where l is the length of the sensitive hot-film portion, and the wavenumber component κ_2 is aligned with the coordinate x_2 . Wyngaard¹⁵² expressed the corrections on the turbulence spectrum as the ratio between the original and the filtered model spectrum, that is,

$$Q_{11}^\phi(\kappa_1) \equiv \frac{\phi_{11}^m(\kappa_1)}{\phi_{11}(\kappa_1)} = \frac{\iint_{-\infty}^{\infty} \Phi_{11}(\boldsymbol{\kappa}) \chi^2(\kappa_2) d\kappa_2 d\kappa_3}{\iint_{-\infty}^{\infty} \Phi_{11}(\boldsymbol{\kappa}) d\kappa_2 d\kappa_3}, \quad (3.3)$$

3.4 HOT-FILM ANEMOMETRY

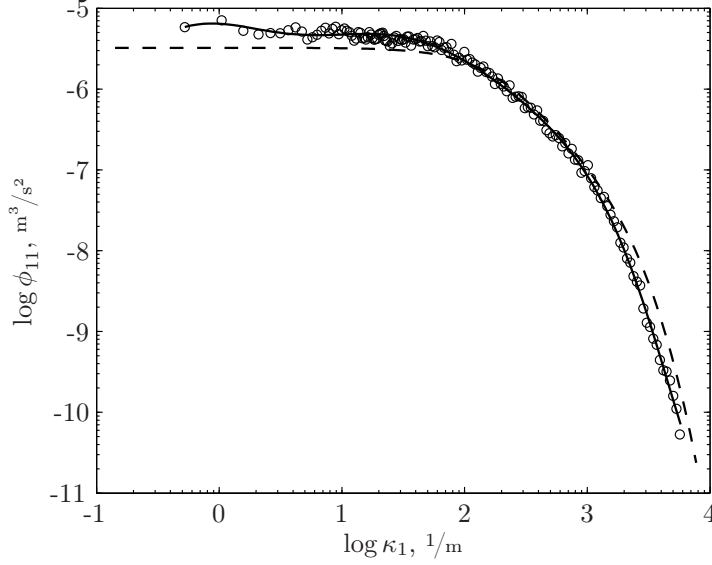


FIGURE 3.6 Eighth-order polynomial function (solid line) fitted to the spectrum estimate from HFA measurements at $x_1/M = 30$ behind the RTG (\circ). For clarity, only a reduced number of spectral estimates are plotted. The broken line is the model spectrum (1.6) evaluated with $\Lambda \equiv k^{3/2}/\epsilon = 12.1$ mm, $\eta = 0.12$ mm and $\epsilon = 45$ cm²/s³.

where the superscript ‘m’ denotes the measured quantity, and accordingly for the squared rms

$$Q_1 \equiv \left(\frac{u_1^m}{u_1'} \right)^2 = \frac{\int_0^\infty \phi_{11}(\kappa_1) Q_{11}^\phi(\kappa_1) d\kappa_1}{\int_0^\infty \phi_{11}(\kappa_1) d\kappa_1}. \quad (3.4)$$

To evaluate expressions (3.3) and (3.4) we used Pope’s model spectrum (1.6) together with the experimentally determined values for the turbulence parameters Λ , η and ϵ . Such a model spectrum is shown for the RTG in figure 3.6 (dashed line), together with the measured and already corrected turbulence spectrum (circles). It should be stressed that this is not a fitted model, but rather a spectrum of a given shape with the same length scales and energy content as the measured spectrum. Numerical values for Λ , ϵ and η were generally derived from the streamwise energy decay (cf. section 4.3). Example correction curves for the RTG and the ITG computed via numerical integration are depicted in figure 3.7. They demonstrate that the finite resolution of the hot-film also affects wavenumbers below $\kappa_1 l = 1$, because for a given wavenumber κ_1^* , the spectrum depends on all wavenumbers $\kappa_1 \geq \kappa_1^*$.¹³⁴

The turbulence spectra of the tested grids turned out to be quite similar in shape, or in other words, the quantities Λ , η and ϵ varied only weakly throughout the tested grids. It was thus found appropriate to calculate spectrum corrections only for the two major grids, the RTG and the ITG, which were sufficiently ‘different’ (cf. figure 4.10). These were then used as well for the others, selecting the correction which seemed more convenient. Inasmuch as the model spectrum is at best an approximation to the measured spectrum, this procedure seemed to be

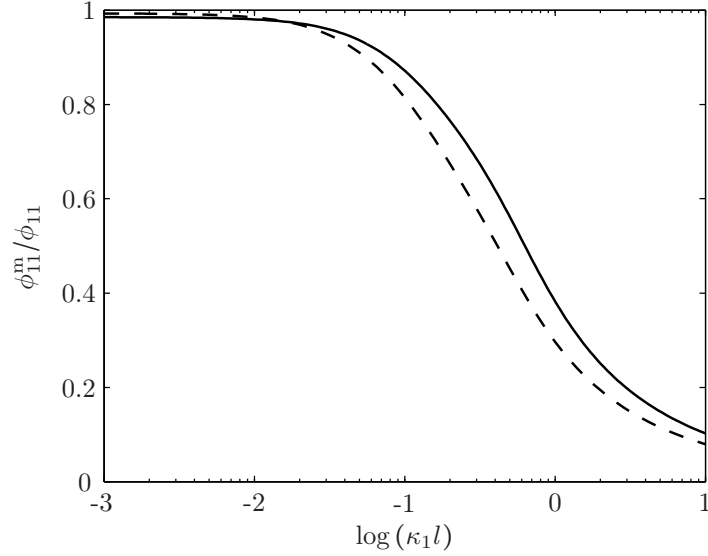


FIGURE 3.7 Longitudinal spectrum correction (3.3): solid line, RTG with $\Lambda/\eta = 100.2$ and $l/\eta = 9.1$; dashed line, ITG with $\Lambda/\eta = 235.6$ and $l/\eta = 11.8$; $l = 1.0$ mm.

justified.

However, figure 3.7 also shows that the correction is more important for high wavenumbers than for low. Therefore, the velocity rms is less affected than the dissipation rate of energy, because of its dependence on the energy containing turbulence scales. Practically speaking, the ratio between the uncorrected and the corrected rms using the curves in figure 3.7 is 0.974 for the plain grid, and 0.978 for the improved grid. These values are in contrast to the ratio between the measured and the corrected turbulence energy dissipation rate, that is,

$$Q_1^\epsilon \equiv \frac{\epsilon^m}{\epsilon} = \frac{15\nu \int_0^\infty \kappa_1^2 \phi_{11}(\kappa_1) Q_{11}^\phi(\kappa_1) d\kappa_1}{15\nu \int_0^\infty \kappa_1^2 \phi_{11}(\kappa_1) d\kappa_1}, \quad (3.5)$$

which yields an underestimation of ϵ as large as 25 % in the case of the RTG, and 33 % for the ITG.

Wynngaard's method applies only to probes with a heat transfer uniform over l , and might not be sufficient to correct the spectral attenuation for 'real' probes. Accepting the premise that the small scales of turbulence are universal, and that the model spectrum is a good approximation to this universality, it follows that the measured spectrum in figure 3.6 is insufficiently corrected in the dissipation region. To this end, Schedvin et al.¹¹⁷ presented a different procedure, where they rectified their measured spectra by iteratively adjusting its high wavenumber end to a supposedly universal spectrum until its dissipation rate matched with the dissipation rate of the streamwise decay. This routine has a slightly arbitrary character, coming from the fact that in anisotropic turbulence the dissipation rate calculated from the one-dimensional spectrum under isotropic assumptions is not

3.5 PARTICLE IMAGE VELOCIMETRY

necessarily the same as the one derived from the streamwise decay.^{78, 96} Moreover, George⁵⁴ stressed that every turbulence experiment has its own and, to some extent, unique spectral shape. Based on these concerns and the lack of a known ideal spectrum for the present setup, their correction method was not considered. Neither was the correction for the sampling rate as suggested by Burattini et al.²⁹, because the sampling rate in present experiments was an order of magnitude larger than the Kolmogorov frequency.

Once the streamwise spectrum of each grid was corrected, it was used as a benchmark for the estimates acquired with PIV and LDA. To reduce the number of points in the HFA spectrum, an eighth-order polynomial function of the form

$$\log \phi_{11}(z) = a_0 + a_1 z + a_2 z^2 + \dots + a_8 z^8, \quad (3.6)$$

in which $z = \log \kappa_1$, was fitted to the spectrum.^{31, 75, 115, 117} The parameters a_0 to a_8 were determined by means of a least squares regression. Figure 3.6 shows an example spectrum with the corresponding polynomial fit. Furthermore, the fitted function allows to calculate the derivatives, in order to obtain the lateral and the three-dimensional spectrum via isotropy relations.

3.5 PARTICLE IMAGE VELOCIMETRY

PIV is a widespread measurement technique used in many fluid flow configurations, appreciated for its non-intrusive[‡] character and its ability to capture whole velocity fields. An excellent guidebook on theoretical and practical aspects of the method was written by Raffel et al.¹⁰⁹.

Applying PIV to turbulent flows is still a challenging endeavor, mainly because of its relatively coarse sampling in time and/or space and the low spatial dynamic range, that is, the range between the largest and the smallest resolvable structures. Various attempts have already been undertaken to measure turbulence spectra^{62, 106} and structure functions^{38, 42}. Some of them include large eddy simulation (LES) models to resolve the small scale features^{73, 120}, such as the turbulence dissipation rate, others were able to measure it directly⁷.

3.5.1 PIV SETUP AND CALIBRATION

In our experiments, we employed a PIV chain consisting of two 11 Mpx (4008 by 2672 px) double-buffer cameras (TSI PowerView Plus) with 60 mm f/2.8 Nikkor lenses and a twin Nd:YAG laser (15 mJ/pulse at 532 nm, Quantel Brilliant Twins B) generating two distinct light pulses. The cameras were synchronized with the laser using trigger signals from pulse generators (BNC 500A and 500B). The flow was seeded with 9 g of polyamid tracer particles supplied by Dantec, with an average diameter $d_t = 5 \mu\text{m}$ and a density $\rho_t = 1.03 \text{ g/cm}^3$. To avoid clumping of the seeding

[‡]This holds for flow time scales much larger than the characteristic time scales of the seeding, and depends on the seeding concentration.

in the polymer solutions, it was added to the moderately agitated fluid shortly before the measurements.

Their ability to follow the small scale structures of the flow is partly characterized by the Stokes number $Sk = \rho_t d_t^2 / 18 \rho \eta^2 \approx 10^{-4}$, and partly by the volume fraction occupied by the particles, which was roughly $m_t/m = 2.5 \times 10^{-6}$. According to Elghobashi⁴⁵, the present configuration of seeding and turbulence is close to the regime where the particles enhance the turbulence energy dissipation, but it is assumed that this effect is still negligible.

Measurements were realized with either of two different setups: a stereoscopic and a single camera arrangement. Both were observing the same vertical light sheet produced with optics described in detail by Ursenbacher¹³⁹. The single camera was aligned normal to the light sheet and the TS window, resulting in minimal aberrations. The latter were more important for the stereo PIV, where the cameras had an angle of 30° with the axis normal to the light sheet, despite the Scheimpflug mounts¹⁰⁸ and the water filled plexiglas prism matching the camera axes.

A far more critical issue was the non-coincidence of the light sheets themselves: differences in the Gaussian intensity profiles of the twin lasers, despite both beams being colinear and traversing the same optics, produced 1 mm thick sheets with only a thin area of roughly 0.6 mm common to both. This led to a significant loss of particles on top of the particles disappearing because of out-of-plane motion and sampling. After inspection of some PIV images taken in quiescent water, the amount of particles present in the first image and replaced by new ones in the second is estimated to 30 to 40 %. As a consequence, the out-of-plane velocity could not be measured accurately with the stereo setup and had to be discarded in the present study. On the other hand, the uncertainties of the in-plane velocity components were fairly low for both arrangements, typically ≈ 0.06 px. Furthermore, the time lapse between two subsequent pulses had to be short, which in turn limited the dynamic range of the measured velocity. The mean flow produced a particle displacement typically between 8 and 12 px during a time lapse of 200 μ s, whereas the turbulence intensity is three percent of the mean flow, hence ≈ 0.3 px. Necessarily, the small scale motions of the flow were affected by measurement noise. The section 3.5.3 will describe the method adopted to recover, at least partly, relevant turbulence data.

The effective field of view varied between 6.3 by 4.2 cm and 10.1 by 6.7 cm, depending on the alignment and the camera arrangement. Its size was mainly restricted by the variation of the dissipation rate of turbulence energy across the field of view, which was below 30 %. The observed surface lay in the central x_1 - x_2 -plane with its midpoint located 30 mesh widths away from the grid (cf. figure 3.2). In water, a series of single camera measurements were acquired at five distinct locations on the x_1 -axis, in order to verify the streamwise decay for the plain (RTG) and the improved grid (ITG).

The calibration of the stereoscopic system was done by means of a 10 by 10 cm black two-plane target with white dots on a Cartesian grid, placed into the test

3.5 PARTICLE IMAGE VELOCIMETRY

section filled with water, and aligned with the laser sheet. Each dot on a given vertical or horizontal line is 8 mm away from its neighbors on the same plane, and 4 mm away from its neighbors on the second plane. The two levels are separated by 1 mm, which allows for a stereoscopic calibration with a linear relationship between the world and the image x_3 -coordinate. Cubic relations were found to be appropriate to describe the x_1 - x_2 -plane. A detailed description of the stereoscopic reconstruction method available in the TSI commercial software package is given in Soloff et al.¹²⁴. Misalignments between the the laser sheet and the target were eliminated with the self-calibration method suggested by Wieneke¹⁵⁰.

To calibrate the single camera setup, the same target was used, and the physical x_1 - x_2 -surface was related to the image plane with quadratic functions.

For each experiment, a total of 500 samples was acquired with an approximate sampling rate of 0.25 Hz, owing to the very large CCD arrays. Considering that the integral time scale was of the order of 10 ms, the recorded samples were statistically independent.

3.5.2 PIV PROCESSING

Stereo PIV measurements were processed with a commercial software package (TSI Insight 3G), and an in-house Fortran code was applied to single camera PIV images. The original code written by Ursenbacher¹³⁹ was updated with a multipass algorithm, where a different interrogation window (IW) size can be specified for each pass. Because of the large images, it was necessary to simplify the optimization process for the deformation of the IW, which in turn reduced the accuracy.[§] A main feature of Ursenbacher's code is that it provides spatial derivatives directly computed from the image data by means of IW deformation. This is a particularly nice feature because it avoids additional errors due to a subsequent differentiation of the velocity field. PIV software packages generally do not provide the velocity gradients as a result, albeit they are computed during the deformation. Consequently, for images processed with the commercial code the derivatives were computed from the velocity field using the circulation method¹⁰⁹.

All images were processed with a multipass algorithm starting with an IW size of 128 by 128 px and finishing with either 32 by 32 px or 64 by 64 px. Large-scale statistics and energy dissipation rates were obtained from the larger IWs because of their larger signal-to-noise ratio, whereas spectra were computed for the small IWs. A 50 % IW overlap recovered otherwise lost image data, and increased the number of vectors (but not the frequency response). IW deformation was available for both programs, but the TSI algorithm is excessively time consuming, and was therefore not used. After each pass, a validation procedure was applied to the vector field, and spurious vectors were replaced via interpolation between valid neighbors. The outlier detection was based on a global histogram filter, followed by a local median filter. To the in-house code, we added a normalized version of the median filter,

[§]The original genetic algorithm was replaced by a less accurate, but much more efficient least squares procedure.

which is more adapted to velocity fields with strong gradients.¹⁴⁹ The amount of replaced vectors for either arrangements was generally less than one percent of the total number of vectors.

In order to optimize the processing, the evolution of the mean and the rms error on synthetic PIV images generated with a software developed by Ursenbacher¹³⁹ was assessed. These images had a size of 512 by 512 px with a background noise matched to the real measurements. The particle density was matched to the real PIV images, notably 10 per 32 by 32 px area, and their average diameter (defined as the diameter where the intensity drops below 5 % of its peak) was set to 4 px. Figure 3.8 (a) shows an example of the imposed flow field, which consisted of Taylor vortices defined by the stream function

$$\psi(y_1, y_2) = \psi_0 \sin \frac{\pi y_1}{d_T} \sin \frac{\pi y_2}{d_T}, \quad (3.7)$$

with a diameter d_T of 64 px, overlaid with a uniform translation of 10.2 px/s. The intensity ψ_0 ranged from 1.6 to 48.0 px²/s, which is equivalent to maximum velocity fluctuations between 0.07 and 2.26 px/s, or 0.7 and 22.2 % of the mean velocity, respectively. Both PIV codes processed all ten image pairs, with the processing parameters chosen such that the amount of spurious vectors was minimal. In particular, these were a uniform window function and a Gaussian subpixel peak interpolation. The same settings were applied during the computation of the measured turbulence fields.

A sample velocity field calculated with the in-house software is depicted in figure 3.8 (b). All vortices are distinguishable in the vorticity field, but due to the sampling filter of the PIV the calculated vorticity is biased towards zero.

Figure 3.9 shows the average bias and uncertainty on the horizontal displacement and the vorticity as a function of increasing vorticity. As suspected, mean and rms errors increase with increasing vorticity. The figure illustrates the superior performance of the in-house software, which includes IW deformation for large velocity gradients.

To simulate the diverging light sheets, we created image pairs where a fraction of the particles in the first image was replaced by roughly the same amount of new particles randomly seeded in the second image. Fortunately, both PIV codes are only weakly sensitive to extensive particle loss between subsequent images, as is shown in figure 3.10. Of course, these results are for the in-plane velocity only.

3.5.3 VELOCITY SPECTRA AND RMS

Longitudinal and lateral power spectra were computed along x_1 by means of a standard fast Fourier transform (FFT). According to the homogeneity hypothesis, the spectra were averaged along x_2 . Each velocity map contained only two to three statistically independent spectra, in other words, vector lines separated by more than two integral length scales. In order to improve the convergence, the spectra were further averaged over several velocity fields. In the case of water, the flow and

3.5 PARTICLE IMAGE VELOCIMETRY

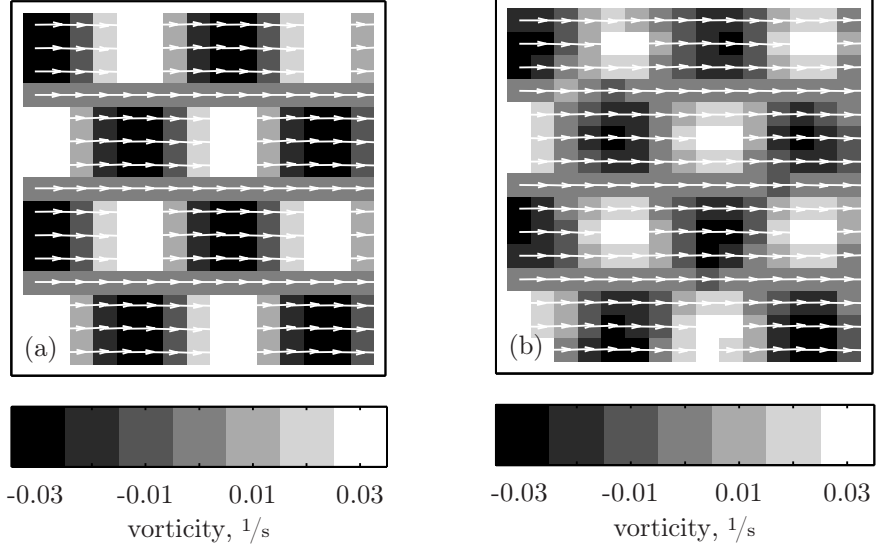


FIGURE 3.8 Velocity and vorticity fields of (a) the imposed convected Taylor vortex array with a diameter of 64 px and (b) the result of the in-house PIV processor. Only one quarter, that is, 15 by 15 vectors of the actual field is shown.

fluid properties remained constant, and averages were calculated over all 500 samples, which is equivalent to a time interval of ≈ 34 min. For polymer solutions, the fluid properties changed during the experiment, due to destruction of the polymer chains. Therefore, averages were taken over shorter periods of time. Practically speaking, we assumed the fluid characteristics to be stable for two complete cycles in the flow tunnel, that is ≈ 200 s, and hence averaged the turbulence statistics over roughly 50 samples. Despite the low number of independent spectral estimates in these smaller sets, the 95 % confidence intervals still converged to within 20 % of the mean value. In general, the time averages were subtracted from the velocity fields, prior to the calculation of rms and spectra.

Poelma et al.¹⁰⁶ recently investigated the influence of interpolated vectors on the power spectrum calculated with FFT, and demonstrated that it is significantly attenuated when the fraction of such vectors attains 20 % or more. With generally less than 1 % spurious vectors for both IW sizes, this effect can be neglected in our spectra.

Another, far more important, attenuation arises from the spatial and the temporal sampling of the PIV technique, similar to the filtering effect of the HFA described above. The filter function χ in (3.3) for an IW of width w_1 , height w_2 and depth w_3 can be expressed as⁸¹

$$\chi(\boldsymbol{\kappa}) = \frac{\sin(\kappa_1 \bar{U}_1 \Delta t / 2)}{\kappa_1 \bar{U}_1 \Delta t / 2} \frac{\sin(\kappa_1 w_1 / 2)}{\kappa_1 w_1 / 2} \frac{\sin(\kappa_2 w_2 / 2)}{\kappa_2 w_2 / 2} \frac{\sin(\kappa_3 w_3 / 2)}{\kappa_3 w_3 / 2}, \quad (3.8)$$

EXPERIMENT SETUP AND DATA PROCESSING

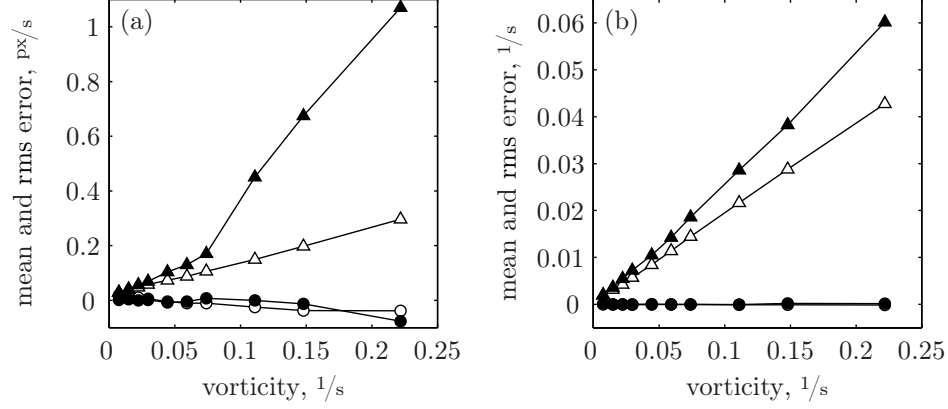


FIGURE 3.9 Mean (\circ , \bullet) and rms (\triangle , \blacktriangle) error on (a) the horizontal displacement and (b) the vorticity, for a Taylor vortex array with a diameter of 64 px and a uniform translation of 10.2 px. Plotted against the maximum absolute vorticity: open symbols, in-house PIV code; solid symbols, TSI software.

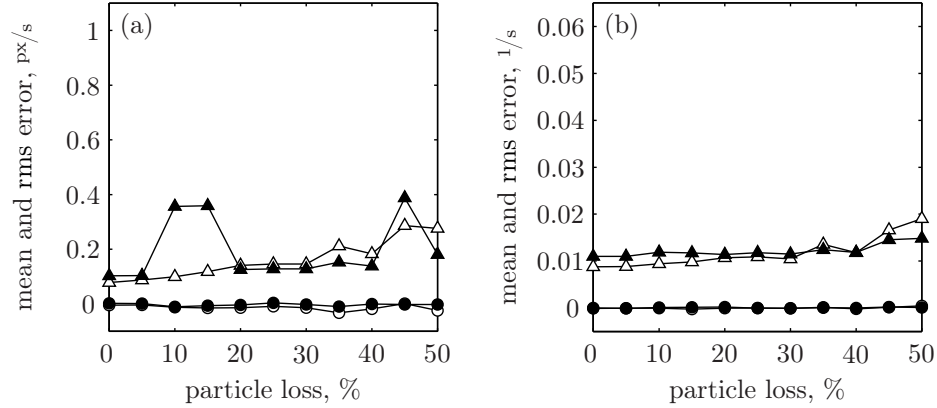


FIGURE 3.10 Influence of lost particles on a convected vortex array: mean (\circ , \bullet) and rms (\triangle , \blacktriangle) error on (a) the horizontal displacement and (b) the vorticity: open symbols, in-house PIV code; solid symbols, TSI software. Uniform translation = 10.2 px/s and maximum absolute fluctuation = 0.47 px/s

where Δt is the time lapse between two subsequent images. We also assume a mean flow in x_1 -direction. Unlike HFA, PIV measurements contain a relatively high noise level, often reaching into the interesting region of the spectrum, and hence, cannot be neglected. It was shown⁴⁸, that the PIV noise spectrum consists of a white noise ξ_{ii} modulated by the spectral function

$$\chi^*(\kappa_1) = \frac{\sin(\kappa_1 w_1/2)}{\kappa_1 w_1/2}. \quad (3.9)$$

3.6 LASER DOPPLER ANEMOMETRY

The measured spectrum can, thus, be written as

$$\phi_{ii}^m(\kappa_1) = 2 \iint_{-\infty}^{\infty} \Phi_{ii}(\boldsymbol{\kappa}) \chi^2(\boldsymbol{\kappa}) d\kappa_2 d\kappa_3 + \chi^{*2}(\kappa_1) \xi_{ii}. \quad (3.10)$$

From this it follows that the true spectrum can be obtained from the measured spectrum by

$$\phi_{ii}(\kappa_1) = \frac{\phi_{ii}^m(\kappa_1) - \chi^{*2}(\kappa_1) \xi_{ii}}{Q_{ii}^{\phi}(\kappa_1)}, \quad (3.11)$$

where $Q_{ii}^{\phi}(\kappa_1)$ is the one-dimensional spectrum correction (3.3).

The white noise level ξ_{ii} was deduced directly from the measured spectra, as proposed by Foucaut et al.⁴⁸, provided that at the cut-off wavenumber κ_c ($\equiv 2.8/w_1$) the noise is much larger than the filtered spectrum, that is, $\chi^{*2}(\kappa_c) \xi_{ii} \gg \phi_{ii}(\kappa_c) Q_{ii}^{\phi}(\kappa_c)$. At the wavenumber κ_c , the noise spectrum $\chi^{*2}(\kappa_c) \xi_{ii}$ has decreased by one half, hence the actual level of ξ_{ii} is twice the value $\phi_{ii}^m(\kappa_1 = \kappa_c)$.

Integrating relation (3.10) over all κ_1 from zero to infinity, one obtains the squared rms velocity

$$(u_i'^m)^2 = Q_i u_i'^2 + \int_0^{\infty} \chi^{*2}(\kappa_1) \xi_{ii} d\kappa_1, \quad (3.12)$$

in which Q_i was already defined by (3.4). The remaining integral represents the contribution of the noise to the rms velocity. To obtain the true rms velocity, equation (3.12) has to be solved for u_i' .

In polymer solutions the shape of the spectrum changes, and ideally the model function utilized for the correction should be adapted. Unfortunately, the wavenumber range of the spectrum captured with piv was too narrow, to accurately estimate the necessary length scales. As a consequence, all spectra measured in polymer solutions were corrected with the same function as for water. By this, additional uncertainties are avoided, although the correction is not optimal.

3.6 LASER DOPPLER ANEMOMETRY

Velocity profiles, streamwise turbulence decay and turbulence spectra have been realized by means of LDA. Like PIV, it is a non-intrusive technique, but with the limitation of punctual measurements. In return, it has a much better temporal resolution, and modern systems usually do not require calibration. Detailed insights into the principles and practical considerations can be found in Abbiss et al.¹, Durst et al.⁴³ and Albrecht et al.³, and more specifically on the usage in turbulent flows, in Buchave et al.²⁸.

3.6.1 LDA SETUP AND RECORDING DETAILS

The LDA employed in our experiment is a Dantec Fibre Flow system with two velocity components aligned with x_1 and x_2 . It was mounted on a traverse with

three movable axes, which allowed to sweep through more than two thirds of the test volume, and take measurements of the streamwise and the vertical transverse velocity components. The probe had a fixed focal length of 400 mm and a beam spacing of 38 mm. In water, this resulted in a measuring volume with a diameter and a length of roughly 118 μm and 3.3 mm, respectively.[¶] The particles were the same as for PIV, and the seeding density was such that the average data rate \dot{n} at $U_0 = 1.2 \text{ m/s}$ reached a value between 600 Hz for large scale statistics, and 2.5 kHz for spectral measurements. Furthermore, the sampling was verified to follow a Poisson distribution, which requires a homogeneous particle distribution.^{110, 125} In this case, the measured particle rates correspond to an average particle spacing of 2.0 and 0.5 mm, respectively. Because of the relatively low data rate, more statistically independent samples were recorded and the large scale statistics converged with less samples. Typically, 5×10^4 samples were acquired at each position to determine the streamwise decay of the turbulence intensity, and 10^6 samples for the spectrum.

The data was acquired in *burst-mode*, which records a velocity signal when there is only one particle at a time crossing the test volume. Hence, no volume averaging of the velocity data occurs. Nonetheless, one can expect that for turbulence scales with a size comparable to the measurement volume, or smaller, the statistics will be overestimated, because at high data rates x_3 -gradients in the direction of the LDA axis of larger structures are mistaken for smaller structures. Thus, the turbulence spectrum at a given wavenumber is biased by the spectrum of all wavenumbers below, or in other words, a *fold forward* occurs. As appropriate correction procedures were not available, the spectrum was cut at the highest admissible wavenumber. However, the estimator variance also increased at high wavenumbers, which makes a full recovery very difficult.

Another, quite similar issue with LDA is the statistical bias towards higher velocities.²⁸ The usual correction implies a transit time weighting during the calculation of the statistics. In our case, the differences between the corrected and the biased mean and rms values were less than 3 %, which was expected due to the low turbulence levels. Therefore, it could safely be neglected.

Instead, we were concerned about the velocity bias that may occur when the laser beams traverse media of different refractive indices.¹³⁵ A discrepancy between the position of the beam waists and the location where the beams cross creates gradients in the fringe pattern^{43, 61}, and hence, produces a skewed velocity distribution with the tail on the lower velocity side. However, no such systematic skew has been detected.

3.6.2 VELOCITY SPECTRA

Data gathered in burst-mode is irregularly sampled, and it is a challenging task to determine the spectrum. A multitude of techniques has been proposed on this very subject^{14, 23, 39, 142, 143}. The one adopted here is based on the *sample-and-*

[¶]These values were estimated from the manufacturer specifications given for air

3.7 MONITORING OF TEMPERATURE AND VISCOSITY

hold reconstruction method proposed by Adrian and Yao², and later improved by Simon and Fitzpatrick¹²². The improvement consists of a proper deconvolution to remove the step noise and the data rate filter effect, introduced by the equidistant resampling.

Assuming a measured one-dimensional spectrum $\phi_{ii}^m(f_j)$ with $1 \leq j \leq N$ discrete frequency samples, computed from data resampled at a rate f_s , one can express the true spectrum as

$$\phi_{ii}(f_j) = \frac{\phi_{ii}^m(f_j)}{\chi^2(f_j)} - \xi_{ii}, \quad (3.13)$$

where

$$\chi^2(f_j) = \frac{1}{2} \frac{\dot{n}}{f_s} \frac{1 - \exp(-2\dot{n}/f_s)}{1 - 2 \cos(2\pi j/N) \exp(-\dot{n}/f_s) + \exp(-2\dot{n}/f_s)} \quad (3.14)$$

is the reconstruction low-pass filter, and

$$\xi_{ii} = \frac{1}{N} \left\{ \sum_{j=0}^{N-1} \frac{\phi_{ii}^m(f_j)}{\chi^2(f_j)} - \sum_{j=0}^{N-1} \phi_{ii}^m(f_j) \right\} \quad (3.15)$$

is the total white noise, including the measurement noise and the step noise of the reconstruction. The noise level can, thus, be estimated from the measured spectrum, and requires no a priori knowledge.

Synthetic LDA data, that were generated by resampling a measured HFA signal according to a Poisson distribution with a mean data rate $\dot{n} = 1$ kHz, allowed to test the above procedure. The true and the LDA spectra computed with the original method and the corrected procedure are shown in figure 3.11. Up to ≈ 80 Hz both methods produce an adequate estimate. Above this frequency, the spectrum found with the original method rolls off due to the data rate filter with the cut-off frequency $f_c (\equiv \dot{n}/2\pi)$, indicated by the arrow. Simon and Fitzpatrick's¹²² method yields a spectrum close to the true spectrum up to roughly 400 Hz, before the variance becomes important.

In order to obtain adequate results with the above method, the resampling frequency needs to be large. We found that ten times the average data rate was sufficient. Spectra were then calculated for data blocks with a duration of 1.25 seconds, which is equivalent to roughly 100 integral time scales. Averaging over all blocks allowed to reduce the variance. The same procedure was already described for the HFA spectra. Once the estimate of the frequency spectrum $\phi_{ii}(f)$ was obtained, it was corrected using the relations (3.13) to (3.15), and finally converted to a wavenumber spectrum $\phi_{ii}(\kappa_1)$.

3.7 MONITORING OF TEMPERATURE AND VISCOSITY

Assuming that the molecular weight of the polymers is the only quantity altering during the experiments, its change will be reflected in the solution viscosity. The breakdown of polymer chains leads to lower average molecular weights, and hence,

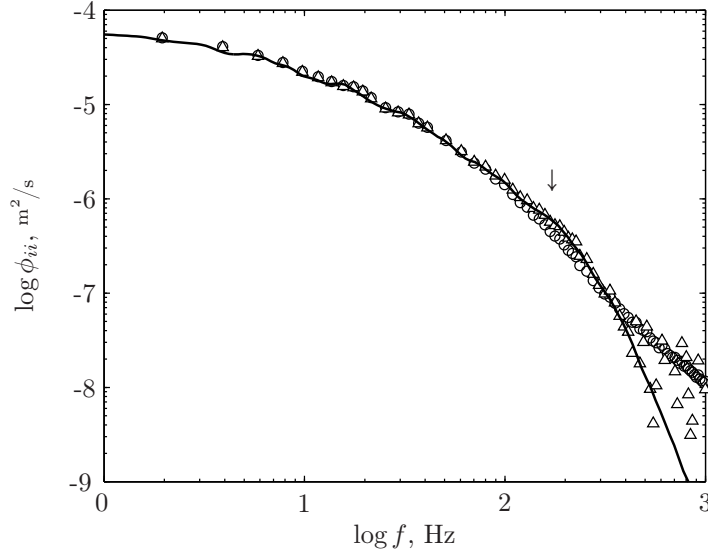


FIGURE 3.11 LDA spectrum calculated with the improved sample-and-hold reconstruction method¹²² (Δ) compared to the uncorrected method² (\circ) and the true spectrum (solid line). The arrow indicates the cut-off frequency f_c ($\equiv \dot{n}/2\pi$) of the reconstruction low-pass filter. For clarity, not all spectral samples are presented.

to a lower solution viscosity. In order to quantify this evolution during the experiments, the following strategy was adopted: fluid samples were taken at 5, 10, 20, 40 and 60 minutes after the start of the experiment. These correspond to samples having realized 3, 6, 12, 24 and 36 circuits in the tunnel, considering that one complete cycle takes roughly 100 s at a mean velocity of 1.2 m/s in the working section. An additional sample of non-degraded fluid taken shortly before the beginning of the experiment served as reference.

The fluid temperature in the TS was monitored continuously by means of a Dataforth K Thermocouple with its tip positioned in the boundary layer at the top window. The rather large volume of the facility has (at least) the advantage, that no temperature control was necessary. Experiments were run at room temperature, that is, between 22 and 24 °C, mainly depending on the operation time. During a measurement run of one hour, the temperature typically changed by 0.2 °C at most, regardless of the working fluid.

3.8 TURBULENCE DISSIPATION AND LENGTH SCALES

The above mentioned measurement techniques provide different strategies to determine turbulence properties, such as the dissipation rate or the turbulence length and time scales. The single hot-film measurement allows to capture the whole turbulence spectrum, but requires a correction for its finite resolution. So does the PIV, but it enables the estimation of the longitudinal and the lateral spectrum

3.8 TURBULENCE DISSIPATION AND LENGTH SCALES

without invoking the frozen turbulence hypothesis. The latter was again necessary for spectra evaluations with LDA. Although it allowed to measure two velocity components, the low data rates limited the resolution of the velocity spectra. Combining all together, one might be able to gain a relatively accurate picture of the turbulence studied.

3.8.1 ENERGY DISSIPATION RATE

In grid turbulence experiments, there exist several approaches to measure the turbulence energy dissipation rate ϵ defined in equation (1.9). For measurement techniques where only one component is determined, such as the employed hot-film probe, the terms in (1.9) including velocities and derivatives along the other axes have to be replaced through isotropy relations^{12, 64, 134}. Then the expression reads

$$\epsilon = 15\nu \left\langle \left(\frac{\partial u_1}{\partial x_1} \right)^2 \right\rangle \approx 15\nu \frac{1}{\bar{U}_1^2} \left\langle \left(\frac{du_1}{dt} \right)^2 \right\rangle. \quad (3.16)$$

where the third term was found by virtue of the Taylor hypothesis.

Whole-field measurements with PIV, on the other hand, give access to spatial derivatives of the velocity components. Consequently, more terms of the rate-of-strain tensor are available to determine the dissipation rate. Terms that are still missing are replaced according to assumptions about the studied turbulence, which do not necessarily imply isotropy. This greatly improves the accuracy of the estimate. The velocity derivatives were either computed from the velocity field by means of finite differences in the case of the stereo setup, or emerged directly from the IW deformation process when a single camera was employed. Figure 3.9 (b) gives an idea about the performance of both methods for flows with strong vorticity.

Similar to the hot-film, the dissipation calculated from PIV maps is heavily underestimated. In fact, for the present experiments the ratio between the filtered and the ‘true’ dissipation rate was between 0.2 and 0.4, depending on the IW size. Assuming isotropy, the true dissipation rate can be deduced from the spectrum through⁹⁷

$$\epsilon = 15\nu \int_0^\infty \kappa_1^2 \phi_{11}(\kappa_1) d\kappa_1 = \frac{15}{2}\nu \int_0^\infty \kappa_1^2 \phi_{22}(\kappa_1) d\kappa_1. \quad (3.17)$$

The measured dissipation rate is obtained from the measured longitudinal spectrum (3.10)

$$\begin{aligned} \epsilon^m &= 15\nu \int_0^\infty \zeta^2(\kappa_1) \phi_{11}^m(\kappa_1) d\kappa_1 \\ &= Q_1^\epsilon \epsilon + 15\nu \int_0^\infty \zeta^2(\kappa_1) \chi^{*2}(\kappa_1) \xi_{11} d\kappa_1, \end{aligned} \quad (3.18)$$

where

$$Q_i^\epsilon = \frac{\int_0^\infty \zeta^2(\kappa_1) \phi_{ii}(\kappa_1) Q_{ii}^\phi(\kappa_1) d\kappa_1}{\int_0^\infty \kappa_1^2 \phi_{ii}(\kappa_1) d\kappa_1}, \quad (3.19)$$

is the ratio between the filtered and the true dissipation rate as proposed by Lavoie et al.⁸¹. (Note that here is made a difference between the actually measured quantity that includes noise, and the filtered quantity without noise. Considering the HFA corrections (3.3) to (3.5) where no noise was taken into account, the measured and the filtered quantities are identic.) Equation (3.18) can also be redefined using the lateral spectrum according to (3.17). The function

$$\zeta(\kappa_1) = \frac{\sin(\kappa_1 w_1/2)}{w_1/2} \quad (3.20)$$

represents a filter accounting for derivatives based on finite differences in the x_1 -direction, and where w_1 is the IW width.⁸¹ Equation (3.19) is equivalent to the expression in (3.5) for very small w_1 . Analogously to the other corrections introduced earlier for HFA and PIV, the correction factor Q_i^ϵ is determined by means of the model spectrum. Finally, the true dissipation can be deduced from relation (3.18).

Reaching this point, one should notice that this correction is valid only for dissipation rates computed from derivatives in the x_1 -direction, that is, equation (3.17). A more general form of the correction, for dissipation rates calculated from mixed spatial derivatives, is based on the three-dimensional spectrum¹⁰⁷

$$E(\kappa) = -\kappa \frac{d}{d\kappa} \left[\frac{1}{2} \phi_{11}(\kappa) + \phi_{22}(\kappa) \right], \quad (3.21)$$

where $\kappa (\equiv \sqrt{\kappa_i \kappa_i})$ is taken to be equal to κ_1 . The corresponding measured three-dimensional spectrum reads

$$E^m(\kappa) = -\kappa \frac{d}{d\kappa} \left[\frac{1}{2} \phi_{11}(\kappa) Q_{11}^\phi(\kappa) + \phi_{22}(\kappa) Q_{22}^\phi(\kappa) \right] - \kappa \frac{d}{d\kappa} \chi^{*2}(\kappa) \left[\frac{1}{2} \xi_{11} + \xi_{22} \right], \quad (3.22)$$

which leads to the measured dissipation rate

$$\epsilon^m = 2\nu \int_0^\infty \zeta^2(\kappa) E^m d\kappa. \quad (3.23)$$

Substituting (3.22) into (3.23) one gets

$$\begin{aligned} \epsilon^m = 2\nu \int_0^\infty \zeta^2(\kappa) E(\kappa) Q_E(\kappa) d\kappa \\ + 2\nu \int_0^\infty \zeta^2(\kappa) \left\{ -\kappa \frac{d}{d\kappa} \chi^{*2}(\kappa) \left[\frac{1}{2} \xi_{11} + \xi_{22} \right] \right\} d\kappa, \end{aligned} \quad (3.24)$$

where

$$Q_E(\kappa) = \frac{-\kappa \frac{d}{d\kappa} \left[\frac{1}{2} \phi_{11}(\kappa) Q_{11}^\phi(\kappa) + \phi_{22}(\kappa) Q_{22}^\phi(\kappa) \right]}{-\kappa \frac{d}{d\kappa} \left[\frac{1}{2} \phi_{11}(\kappa) + \phi_{22}(\kappa) \right]} \quad (3.25)$$

3.8 TURBULENCE DISSIPATION AND LENGTH SCALES

is the three-dimensional spectrum correction. By rewriting the ratio between the filtered and the true dissipation rate (3.5) as a function of the three-dimensional spectrum,

$$Q_E^\epsilon = \frac{\int_0^\infty \zeta^2(\kappa) E(\kappa) Q_E(\kappa) d\kappa}{\int_0^\infty \kappa^2 E(\kappa) d\kappa}, \quad (3.26)$$

one finally obtains the correction for the measured dissipation rate, that is,

$$\epsilon^m = Q_E^\epsilon \epsilon + 2\nu \int_0^\infty \zeta^2(\kappa) \left\{ -\kappa \frac{d}{d\kappa} \chi^{*2}(\kappa) \left[\frac{1}{2} \xi_{11} + \xi_{22} \right] \right\} d\kappa, \quad (3.27)$$

where the remaining integral is the noise contribution. With the last expression, one can eventually correct the dissipation rate computed from PIV maps including all available velocity derivatives, which was not possible with Lavoie et al.'s original formulation, except for perfectly isotropic turbulence.

As has been mentioned above, corrections for polymer solutions were the same as for water: once a correction was computed for a given grid, it was applied to dissipation estimates in water and viscoelastic fluids.

The corrections for the dissipation rates derived from PIV measurements were generally very large, typically 60 % for IWs with a size of 32 by 32 px, and 80 % for 64 by 64 px. Values obtained from both IW sizes agreed generally to within 10 %, which was considered good. Essential to this was the noise removal explained above.

Alternatively, the dissipation rate in a grid turbulence experiment can also be deduced from the macroscale energy decay along the streamwise direction. With the assumption that no turbulence is produced beyond a certain distance from the grid, the turbulence energy budget for this production-free region reads

$$\frac{dk}{dt} = -\epsilon \approx \bar{U}_1 \frac{dk}{dx_1}, \quad (3.28)$$

accepting the frozen turbulence hypothesis. A particular advantage of this approach is that it does not require an exceptionally high spatial or temporal resolution. It can, thus, be estimated from any of the presented measurement techniques, provided that measurements at various streamwise locations are available.

An overview of other, more general methods to determine the dissipation rate, such as large-eddy PIV or fitting structure functions, can be found in de Jong et al.³⁸.

3.8.2 TURBULENCE LENGTH SCALES

The smallest turbulence length scale in a Newtonian fluid is the Kolmogorov scale (supposedly this holds as well for polymeric liquids of the type considered here¹⁷), and is given by

$$\eta \equiv \left(\frac{\nu^3}{\epsilon} \right)^{1/4}. \quad (3.29)$$

It requires an accurate determination of the dissipation rate, and in particular of the fluid viscosity.

The streamwise and the transverse integral length scales defined by

$$\Lambda_1 \equiv \int_0^\infty \frac{B_{11}(r_1)}{u_1'^2} dr_1 \quad \text{and} \quad \Lambda_2 \equiv \int_0^\infty \frac{B_{22}(r_1)}{u_2'^2} dr_1, \quad (3.30)$$

were determined from the spatial correlation functions $B_{11}(r_1)$ and $B_{22}(r_1)$, calculated from spectral estimates measured with LDA.

To obtain the Taylor microscale λ defined in (1.13), the generally adopted procedure is to fit an osculating parabola to the correlation coefficient when r_1 tends to zero. According to Batchelor¹², the Taylor length scale can be acquired from both correlation coefficients, B_{11} and B_{22} , provided that the turbulence at small r_1 (large κ_1) is isotropic:

$$\frac{B_{11}(r_1)}{u_1'^2} \approx 1 - \frac{r_1^2}{2\lambda^2} \quad \text{and} \quad \frac{B_{22}(r_1)}{u_2'^2} \approx 1 - \frac{r_1^2}{\lambda^2}. \quad (3.31)$$

Due to the finite resolution, the fitting quality depends on the number of correlation estimates included in the least squares procedure. In order to overcome the lack of robustness, the auxiliary functions

$$g(r_1) = \frac{B_{ii}(r_1)}{u_i'^2} = 1 + a_0 r_1^2 + a_1 r_1^3, \quad (3.32a)$$

$$h(r_1) = \frac{g(r_1) - 1}{r_1^2} = a_0 + a_1 r_1 \quad (3.32b)$$

were used, which adequately describe the correlation coefficient at small r_1 (cf. figure 3.12 (a)). Practically speaking, the parameters a_0 and a_1 were found by fitting the straight line $h(r_1)$ with a least squares approach to the measured data at small r_1 (cf. figure 3.12 (b)). Thus, the Taylor microscale is given by

$$\lambda = \frac{1}{\sqrt{-2a_0}} \quad \text{or} \quad \lambda = \frac{1}{\sqrt{-a_0}}, \quad (3.33)$$

depending on whether the longitudinal or the lateral correlation coefficient was used, respectively. The maximum value of r_1 was chosen such that $(B_{ii}/u_i'^2 - 1)/r_1^2$ presented the longest straight line possible. As shown in figure 3.12 (a), $g(r_1)$ provides a reasonable approximation of the correlation coefficient, and the corresponding parabola is indicated by the dashed line.

3.9 SUMMARY OF EXPERIMENTAL RUNS

Table 3.2 summarizes the experiments that were run to gather the data presented in the subsequent chapters. It specifies the x_1/M -positions explored with each measuring instrument, as well as the purpose of the measurement: either streamwise

3.9 SUMMARY OF EXPERIMENTAL RUNS

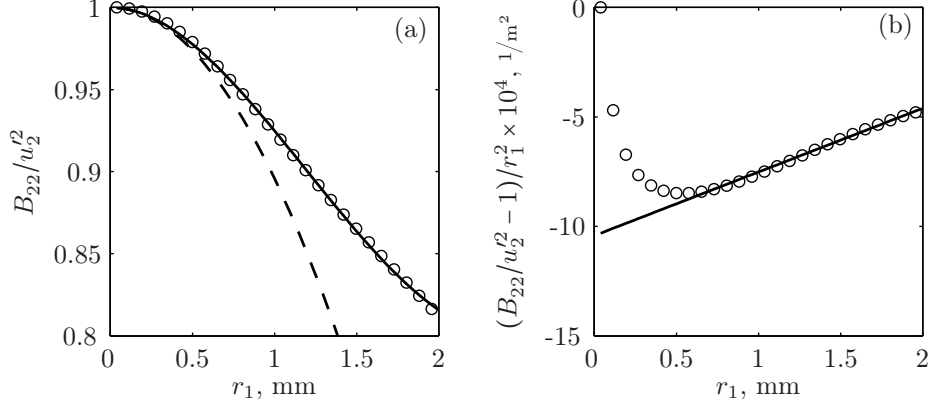


FIGURE 3.12 Taylor microscale parabola fit: (a) lateral correlation coefficient of the measured data (\circ) with the fitted function $g(r_1)$ (solid line) and the resulting parabola (broken line); (b) auxiliary function $h(r_1)$ (solid line) fitted to the measured values.

TABLE 3.2 Summary of experiments with investigated streamwise positions in units of M . Pressure drop measured with a Pitot-static tube (P) or pressure taps (T). Number of fluid samples taken to monitor the solution viscosity.

Fluid	Grid	Decay		Spectra			C_p method	ν samp.
		LDA	PIV	LDA	PIV	HFA		
Water	RTG	11–54	20–45	30	30	30	P&T	—
	ITG	11–54	20–45	30	30	30	P&T	—
	W12	11–42	—	30	—	30	P	—
	W8	11–42	—	30	—	30	P	—
	W6	11–42	—	30	—	30	P	—
	G6	11–42	—	30	—	30	P	—
PEO 25 wppm	ITG	—	—	—	30	—	T	6
PEO 50 wppm	ITG	—	—	—	30	—	T	6
PEO 100 wppm	ITG	—	—	—	30	—	T	6

energy decay, or velocity spectra and dissipation. Moreover, the table indicates whether a Pitot-static tube or the pressure taps on the facility walls (cf. figure 3.2) were used for the pressure recordings. Fluid samples were taken only during the experiments in polymer solutions. Multiple experiments shown on a given row have been run separately, and were repeated at least once, with the exception of the 25 wppm PEO solution.

In plain water, turbulence experiments were run at a pump rotation speed, such that the mean flow velocity U_0 was of 1.2 ± 0.03 m/s, whereas in polymer solutions, the pump rotation was the same for all fluids. The corresponding grid mesh based Reynolds number Re_M was of roughly 2×10^4 for the experiments in water, and 1.9×10^4 in polymer solutions.

CHAPTER 4

Performance of the new grid in water

4.1 BRIEF OVERVIEW

In this chapter turbulence properties for the new grids are presented and discussed. In particular, static pressure drop, spectrum and streamwise decay measurements were realized in plain water for all tested grids, mainly using LDA and HFA. Additionally, direct measurements of the energy dissipation rate were recorded with PIV for the most promising grid, the ITG, and the reference grid (RTG). Furthermore, dissipation rates and turbulence length scales obtained from the various measurement techniques are compared.

4.2 GRID PRESSURE DROP

The static pressure drop, Δp , at the different grids was measured between the TS entry and the Pitot-static tube placed on the centerline 11 mesh widths ahead of the grid. Additionally, the pressure difference over the entire TS with the RTG or the ITG mounted was also recorded. A compilation of all readings is presented in figure 4.1 by means of the pressure drop coefficient,

$$C_p \equiv \frac{2\Delta p}{\rho U_0^2}, \quad (4.1)$$

plotted against the grid Reynolds number Re_M . The error bars indicate the standard deviation, whereas the ones for the recordings with the Pitot-static tube are too small to be distinguished from the symbol.

The magnitudes of the pressure drops at the RTG lay between 0.45 and 0.55 for Reynolds numbers above 1.5×10^4 , and are the same as the values reported by Friehe and Schwarz⁵¹ for a similar grid geometry. Analytical expressions for the pressure drop coefficient of a plain grid as used by Batchelor and Townsend¹³,

$$C_p = \frac{d/M (2 - d/M)}{(1 - d/M)^4} \approx 0.78, \quad (4.2)$$

or Gad-el-Hak and Corrsin⁵²,

$$C_p = \frac{2Md - d^2}{M^2} \approx 0.34, \quad (4.3)$$

PERFORMANCE OF THE NEW GRID IN WATER

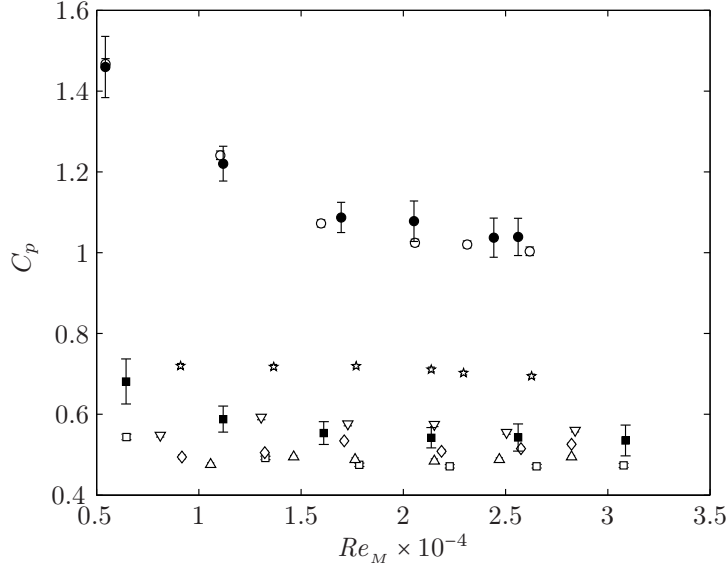


FIGURE 4.1 Static pressure drop coefficients of the turbulence grids measured with the Pitot-static tube (open symbols) and the pressure taps (solid symbols): \square , \blacksquare , RTG; \triangle , G6 grid; \diamond , W6 grid; ∇ , W8 grid; \star , W12 grid; \circ , \bullet , ITG.

do either over- or underestimate the value determined for the present plain grid.

Since the low pressure intake of the pressure taps is located further downstream than the Pitot tube, their pressure difference is larger; this is more distinct for the RTG. With large bead diameters, the blockage ratio increases and, naturally, also does the pressure drop. Williamson and Govardhan¹⁵¹ conducted experiments on a single tethered sphere in a uniform flow field, and reported that the drag of the oscillating sphere could be as large as twice the value for a static sphere.

A marked increase is apparent between the W12 grid and the ITG, which differ only by the number of grid nodes occupied with tethered beads. At a Reynolds number of 2×10^4 the pressure drop for the ITG is about twice as large as the corresponding value for the RTG.

4.3 HOMOGENEITY AND STREAMWISE DECAY

The macroscale properties of the turbulence generated by the different grids were characterized mainly with LDA. For comparison, PIV maps were acquired at five different stations along the streamwise direction, once for the plain grid, and once for the improved grid, ITG.

4.3.1 TRANSVERSE HOMOGENEITY

In the grid wake, turbulence production takes place and the flow is characterized by strong mean shear. Further away from the grid, where the mean flow gradients van-

4.3 HOMOGENEITY AND STREAMWISE DECAY

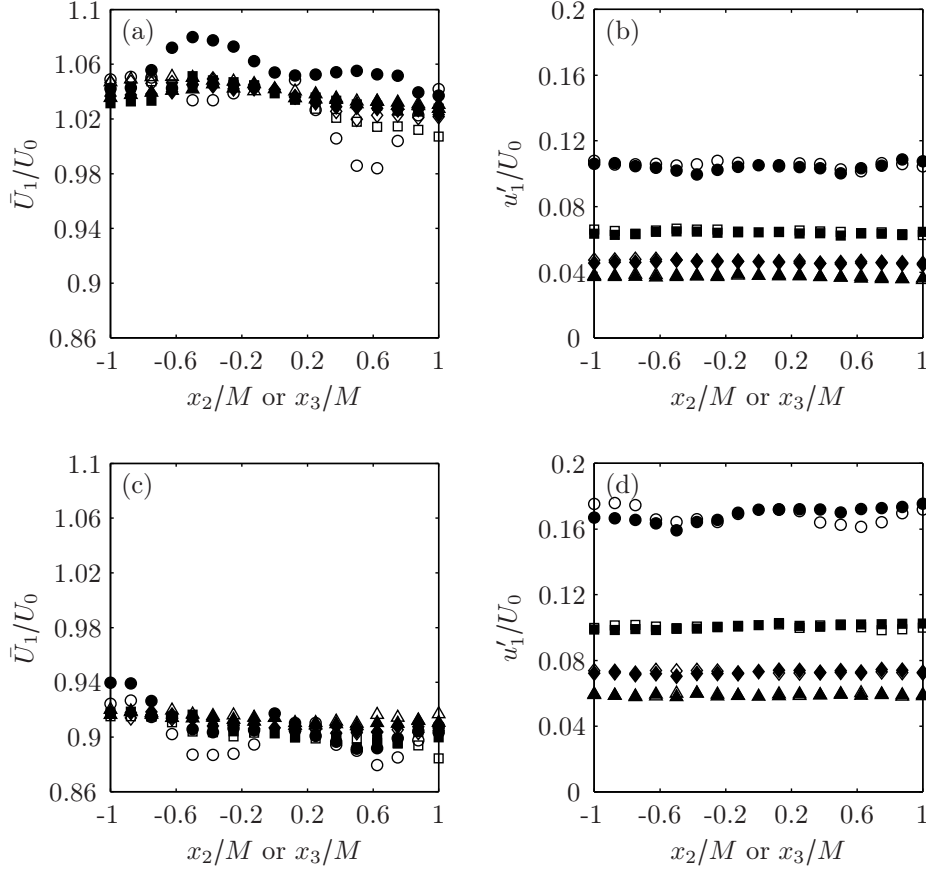


FIGURE 4.2 Velocity profiles in the wakes of the RTG (a, b) and the W12 grid (c, d). Horizontal (open symbols) and vertical (solid symbols) transverse profiles of (a, c) the mean velocity and (b, d) the rms velocity at four different streamwise locations: \circ , \bullet , $x_1/M = 6$; \square , \blacksquare , $x_1/M = 10$; \diamond , \blacklozenge , $x_1/M = 15$; \triangle , \blacktriangle , $x_1/M = 20$.

ish, the turbulent motion becomes statistically homogeneous and is monotonically decaying.

Figure 4.2 shows the streamwise velocity measured across two meshes, and in planes parallel to the grid located at four different downstream positions. The RTG, as well as the W12 grid, cease to have an influence on the mean flow statistics at a distance greater than 15 mesh widths away from the grid. Closer to the grid, one can identify the positions of the grid rods at $x_2/M = x_3/M = -0.5$ and $x_2/M = x_3/M = 0.5$.

A larger view over the entire width and height of the TS reveals that compared to the free-stream, the plain grid (cf. figure 4.3 (a) and 4.3 (b)) introduces a weak but persistent mean shear into the flow. However, the corresponding turbulence intensities are homogeneous to within 0.5%. A somewhat stronger mean shear is generated by the W12 grid (cf. figure 4.3 (c)), in which the outermost rows and

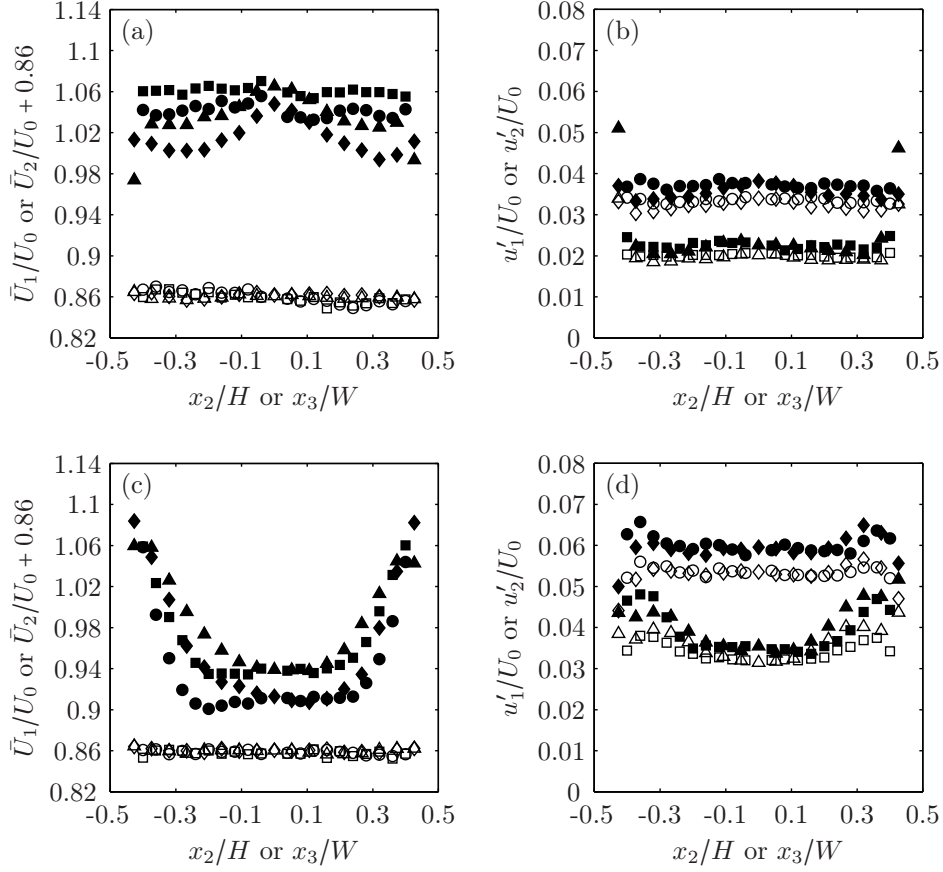


FIGURE 4.3 Turbulence homogeneity of the RTG (a, b) and the W12 grid (c, d). Horizontal (\diamond , \blacklozenge , \triangle , \blacktriangle) and vertical (\circ , \bullet , \square , \blacksquare) transverse profiles of (a, c) the mean velocity and (b, d) the rms velocity at two different streamwise locations: \circ , \bullet , \diamond , \blacklozenge , $x_1/M = 20$; \square , \blacksquare , \triangle , \blacktriangle , $x_1/M = 43$; solid symbols, x_1 -velocity component; open symbols, x_2 -velocity component. Note the offset of \bar{U}_2/U_0 .

columns are not equipped with tethered beads. As a consequence, turbulence is generated in these shear regions, which is reflected in higher turbulence intensities (cf. figure 4.3 (d)). The mean and rms velocity profiles of the G6, W6 and W8 grids differ very little from the W12 grid, and are therefore not shown. Mainly, they have a lower mean velocity gradient and a larger homogeneous region, yet, not as large as the RTG.

Filling the vacant positions around the periphery of the W12 grid with tethered beads increases the pressure drop (cf. circles and squares in figure 4.1) and significantly reduces the mean shear as shown in figure 4.4. The regions where the turbulence intensities vary by less than 0.5 %, in a given cross-section, are considerably extended. They notably grew from roughly one third to more than two thirds in width and height; this is comparable to the plain grid.

4.3 HOMOGENEITY AND STREAMWISE DECAY

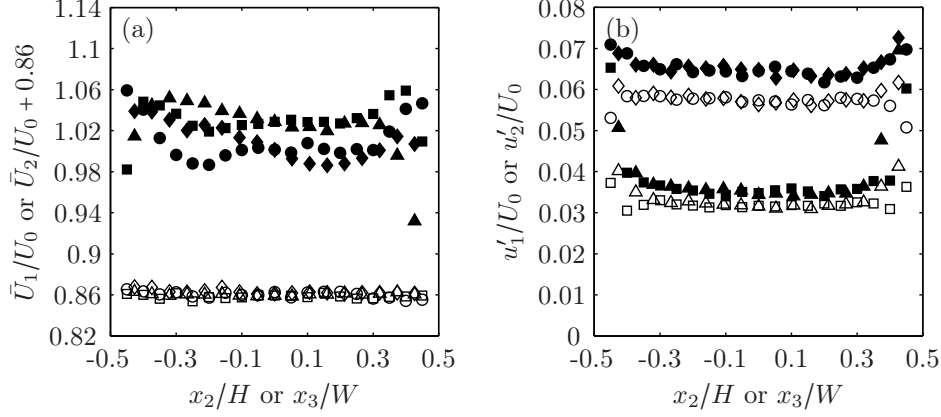


FIGURE 4.4 Turbulence homogeneity of the ITG. Horizontal (\diamond , \blacklozenge , \triangle , \blacktriangle) and vertical (\circ , \bullet , \square , \blacksquare) transverse profiles of (a) the mean velocity and (b) the rms velocity at two different streamwise locations: \circ , \bullet , \diamond , \blacklozenge , $x_1/M = 20$; \square , \blacksquare , \triangle , \blacktriangle , $x_1/M = 50$; solid symbols, x_1 -velocity component; open symbols, x_2 -velocity component. Note the offset of \bar{U}_2/U_0 .

4.3.2 STREAMWISE ENERGY DECAY

Based on the turbulence intensities presented above, a good approximation of homogeneity was found at 20 mesh widths from the grid, and beyond. In this region, the turbulence kinetic energy, $k = q^2/2 = \langle u_i u_i \rangle / 2$, is generally presumed to decay according to a power-law

$$\frac{q^2}{U_0^2} = A_{\text{dk}} \left(\frac{x_1}{M} \right)^{-n_{\text{dk}}}, \quad (4.4)$$

in which A_{dk} and n_{dk} are the decay coefficient and exponent, respectively. Here, the virtual origin that was initially suggested by Comte-Bellot and Corrsin³³ was omitted, because Mohamed and LaRue⁹⁶ pointed out that the fitting of the decay exponent n_{dk} is sensitive to its value. Recent measurements of decaying grid turbulence by Antonia et al.⁶ or Lavoie et al.⁸⁰ support the idea of the virtual origin being located on the grid. Furthermore, fitting our data to a decay law including a virtual origin did not produce an improvement. Worse, any value of the exponent could be obtained with a suitable virtual origin, as was previously noted by Wang and George¹⁴⁷.

For each grid, the decay coefficient and exponent were determined by a least squares regression to the data measured in the homogeneous region, that is, for $x_1/M \geq 20$. Because of the short distance available downstream of the grid, samples had to be taken at small streamwise increments to obtain robust fits. To further improve the fitting, we used multiple data sets for each grid, acquired in identical flow conditions.

Figures 4.5 and 4.6 show the streamwise decays of the turbulence intensities $u_1'^2$ and $u_2'^2$, as well as the decay of the total kinetic energy q^2 , behind the reference grid

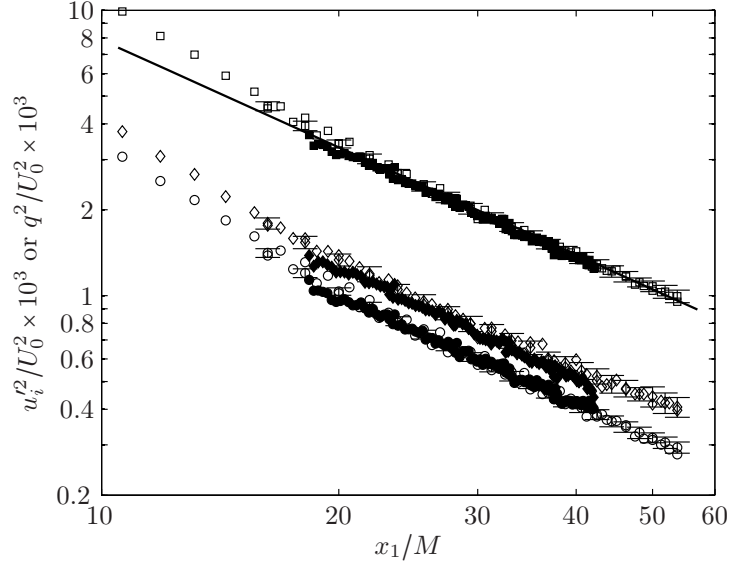


FIGURE 4.5 Streamwise turbulence decay of the RTG: \square , \blacksquare , q^2 ; \diamond , \blacklozenge , $u_1'^2$; \circ , \bullet , $u_2'^2$; open symbols, LDA data; solid symbols, PIV data; solid line, fitted decay law (4.4) with $n_{\text{dk}} = 1.25$ and $A_{\text{dk}} = 140.0 \times 10^{-3}$. The error bars indicate the standard deviation on repeated LDA measurements. For clarity, only every fifth point is shown for the PIV.

and the improved grid, respectively. The horizontal transverse turbulence intensity u_3' was not measured, and thus, the kinetic energy taken to be $q^2 = u_1'^2 + 2u_2'^2$. The error bars correspond to the standard deviation calculated from measurements along various lines parallel to the streamwise centerline. The overlapping data from different measurement series also indicate a good repeatability of the experiments. The fitted power-law is indicated by the solid line, and shows a good agreement with the measured data for large distances from the grid. Closer to the grid, the data points do not fall onto the line, which suggests that homogeneity has not been reached.

The PIV data was corrected with the procedure described in in section 3.5. In particular, five rms correction coefficients were calculated for the five streamwise stages at which PIV fields were acquired, and the corrections for other streamwise positions were obtained via a quadratic interpolation. The final data are depicted in figure 4.5 and 4.6 together with the LDA measurements. Both agree very well. The scatter of the PIV points, especially in the case of the improved grid, emerge from the high noise level and the weak dynamic range.

Comparing the kinetic energy at a given streamwise position, one notices a factor of roughly 2.5 between the RTG and the ITG. But unfortunately, the difference between the streamwise and the transverse turbulence intensities is also apparent in the new grid type. Figure 4.7 summarizes the ratios between the longitudinal and the lateral rms velocities for all tested grids. In all but two cases, namely the W12 grid and the ITG, the anisotropy increases with the streamwise distance to

4.3 HOMOGENEITY AND STREAMWISE DECAY

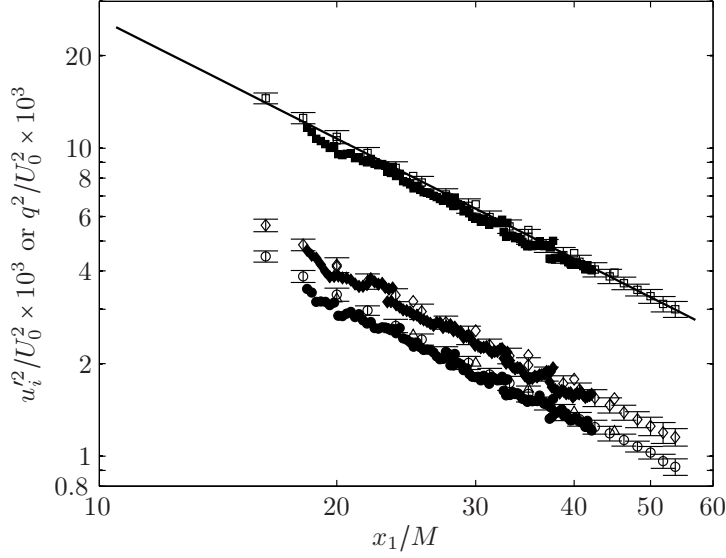


FIGURE 4.6 Streamwise turbulence decay of the ITG: $\square, \blacksquare, q^2$; $\diamond, \blacklozenge, u_1'^2$; $\circ, \bullet, u_2'^2$; open symbols, LDA data; solid symbols, PIV data; solid line, fitted decay law (4.4) with $n = 1.29$ and $A = 517.5 \times 10^{-3}$. The error bars indicate the standard deviation on repeated LDA measurements. For clarity, only every fifth point is shown for the PIV.

the grid, but never exceeds a ratio of 1.2. The ITG keeps a constant level of ≈ 1.13 , suggesting that u_1' and u_2' decay at the same rate, whereas the W12 grid shows an improvement of the isotropy. This could indicate a transfer of energy from the longitudinal to the lateral components, or it might be due to the turbulence production in the peripheral shear regions mentioned above, gaining influence on the centerline turbulence further away from the grid. Overall, the measured differences between u_1' and u_2' are comparable to existing grid turbulence experiments.

Batchelor and Townsend¹³ suggested that the turbulence intensity is proportional to the grid pressure drop, and hence, data that is rescaled with the pressure coefficient C_p should collapse. In figure 4.8 the rescaled turbulence kinetic energies of all tested grids are plotted. It appears that the scaling of the turbulence intensities with the inverse of C_p works reasonably well, although, the data have split into two sets. The lower group of data corresponds to the plain grid and the grids with small bead diameters, whereas the upper two curves belong to the grids with the largest beads, the W12 grid and the ITG. Compared to the first group including the RTG, these two grids produce turbulence with a larger energy content per unit C_p . This in turn, suggests that the motion of the large beads, indeed, amplifies the turbulence intensity compared to a standard plain grid with the same pressure drop coefficient. Considering that the motion of the tethered beads is confined to the transverse plane, one could expect that the lateral fluctuating velocities are enhanced to a greater extent than the longitudinal ones, resulting in an improvement of the large scale isotropy. As figure 4.7 illustrates, this is not the case.

PERFORMANCE OF THE NEW GRID IN WATER

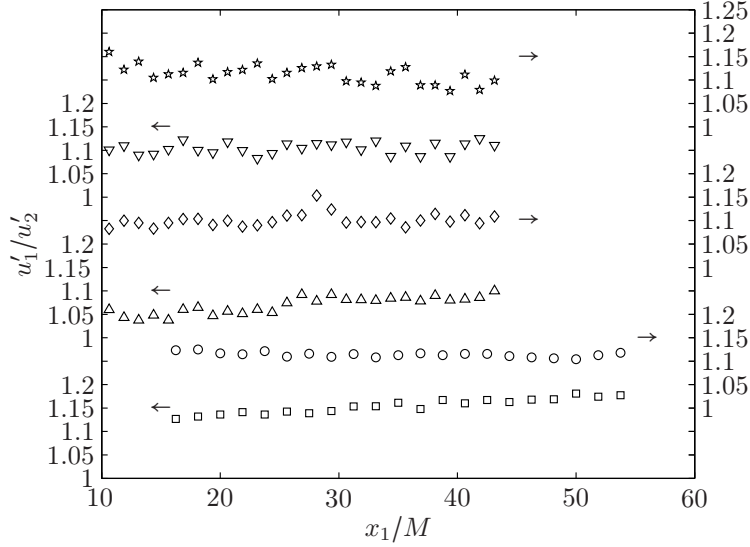


FIGURE 4.7 Large scale isotropy levels: \square , RTG; \triangle , G6 grid; \diamond , W6 grid; ∇ , W8 grid; \star , W12 grid; \circ , ITG.

TABLE 4.1 Streamwise turbulence energy decay and production parameters of (4.4) and (4.6). The values for the decay law parameters A_{dk} and n_{dk} , as well as for the coefficients of the mean flow gradient fitting function A'_{pd} and A''_{pd} , are given with the 95 % confidence intervals.

Grid	$Re_M \times 10^{-3}$	C_p	$A_{dk} \times 10^3$	n_{dk}	A'_{pd}	$A''_{pd} \times 10^3$
RTG	21.0	0.47	140.0 ± 19.8	1.250 ± 0.013	0.963 ± 0.006	11.7 ± 1.1
ITG	21.0	1.04	517.5 ± 27.5	1.293 ± 0.018	0.950 ± 0.006	11.0 ± 1.0
W12	20.5	0.72	511.0 ± 29.5	1.360 ± 0.020	0.876 ± 0.005	10.6 ± 0.9
W8	20.4	0.58	255.4 ± 19.0	1.365 ± 0.013	0.958 ± 0.005	8.0 ± 1.0
W6	20.5	0.52	219.9 ± 38.7	1.350 ± 0.026	0.927 ± 0.005	12.8 ± 0.9
G6	20.7	0.49	245.2 ± 37.9	1.408 ± 0.025	0.970 ± 0.006	8.2 ± 1.2

A summary of the decay parameters A_{dk} and n_{dk} found for the different grids is provided in table 4.1, along with the grid Reynolds number and the corresponding pressure drop coefficient. For A_{dk} and n_{dk} table 4.1 also specifies the 95 % confidence intervals. Literature values for n_{dk} lie typically between 1.1 and 1.4 regardless of the grid geometry, whereas A_{dk} depends on the experimental conditions. Large compilations of power-laws fitted to the streamwise turbulence energy decay can be found in Mohamed and LaRue⁹⁶ and Gad-el-Hak and Corrsin⁵².

In homogeneous turbulence the energy budget is written¹⁰⁷

$$\frac{dk}{dt} = \mathcal{P} - \epsilon, \quad (4.5)$$

where \mathcal{P} is the turbulence production term, which is zero in decaying turbulence. Grid turbulence is at best an approximation to this, thus, production may still

4.3 HOMOGENEITY AND STREAMWISE DECAY

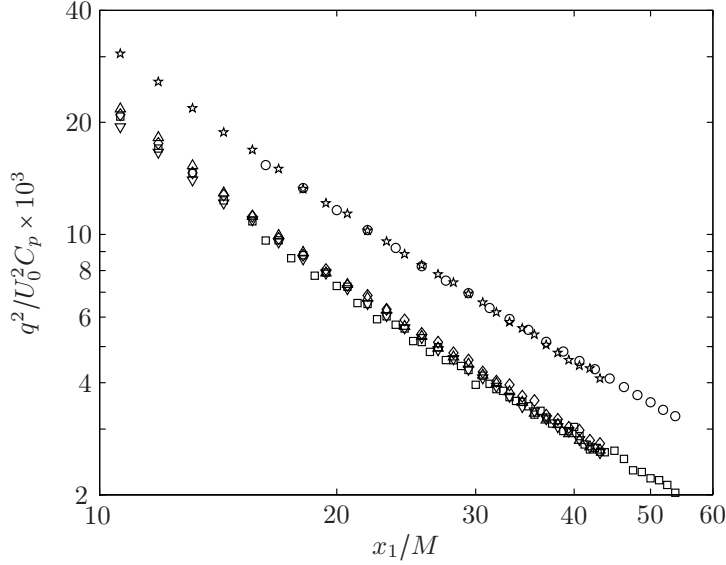


FIGURE 4.8 Streamwise decay of q^2 rescaled with C_p values of table 4.1: \square , RTG; \triangle , G6 grid; \diamond , W6 grid; ∇ , W8 grid; \star , W12 grid; \circ , ITG.

take place. Invoking symmetry about the x_1 -axis and satisfying continuity, the turbulence energy production on the streamwise centerline is given by

$$\mathcal{P} \equiv -\langle u_i u_j \rangle \frac{\partial \langle U_j \rangle}{\partial x_i} = (-u_1'^2 + u_2'^2) \frac{d\bar{U}_1}{dx_1}. \quad (4.6)$$

The streamwise mean flow gradient was determined by differentiation of the function

$$\bar{U}_1 = A'_{\text{pd}} + A''_{\text{pd}} \left(\frac{x_1}{M} \right)^{1/2} \quad (4.7)$$

fitted to the measured mean velocities on the centerline. The latter increased with the growth of the boundary layers on the walls, which was not accounted for in the design of the TS. And with $u_1'^2$ always being larger than $u_2'^2$, it is not surprising to find negative values for the production (cf. figure 4.9). Consequently, turbulence is not produced, but rather, damped by the acceleration of the flow. However, this damping term is three orders of magnitude smaller than the viscous energy dissipation rate estimated with the Taylor hypothesis

$$\epsilon = \mathcal{P} - \frac{U_0}{2} \frac{dq^2}{dx_1}, \quad (4.8)$$

and is therefore negligible.

Hence, the turbulence energy dissipation rate can be estimated from the streamwise decay by differentiating (4.4) to obtain

$$\epsilon_{\text{dk}} = \frac{A_{\text{dk}} U_0^3 n_{\text{dk}}}{2M} \left(\frac{x_1}{M} \right)^{-(n_{\text{dk}}+1)}. \quad (4.9)$$

PERFORMANCE OF THE NEW GRID IN WATER

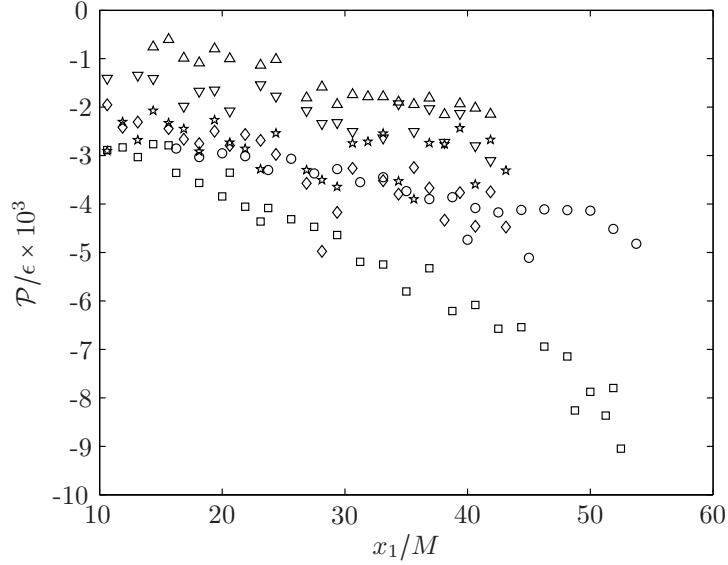


FIGURE 4.9 Streamwise turbulence energy production: \square , RTG; \triangle , G6 grid; \diamond , W6 grid; ∇ , W8 grid; \star , W12 grid; \circ , ITG.

This, in turn, allows to calculate the Kolmogorov microscale

$$\eta_{\text{dk}} = \left(\frac{\nu^3}{\epsilon_{\text{dk}}} \right)^{1/4}, \quad (4.10)$$

and the Taylor microscale

$$\lambda_{\text{dk}}^2 = 5\nu \frac{q^2}{\epsilon_{\text{dk}}}. \quad (4.11)$$

Values for these length scales evaluated at $x_1/M = 30$ are given in table 4.3. Although ϵ_{dk} is quite sensitive to the decay parameters, one notices that η_{dk} varies only moderately for the different grids, as it varies with ϵ_{dk} only to the power of one fourth.

What is interesting to note in the data of table 4.1 is, that all grids with tethered spheres significantly increase the decay coefficient, but at the same time rise the decay rate. The largest decay coefficient was determined for the G6 grid, which had small but heavy beads. The exception is the ITG, which injects more kinetic energy to the turbulence, without a large increase of the exponent. Furthermore, the turbulence decay rescaled with the pressure drop coefficient for the W12 grid, which differs from the ITG only by the missing beads at the outermost rows and columns, is almost identical to the values of the ITG. Hence, the missing beads do not significantly affect the large scale statistics determined here.

4.4 VELOCITY SPECTRA

4.4 VELOCITY SPECTRA

The turbulent velocity spectra have been measured close to the centerline and 30 mesh widths from the grid, in the homogeneous region. HFA and LDA measurements were realized for all grids, and additionally, PIV velocity fields were recorded for the RTG and the ITG.

4.4.1 COMPARISON OF ALL TESTED GRIDS

Figure 4.10 shows the u_1 - and u_2 -spectra in Kolmogorov variables acquired in water for all tested grids. Note that the wavenumber at which energy is dissipated into heat is defined⁶⁴ as $\kappa_K \equiv 1/\eta$. The dissipation rate and the Kolmogorov microscale were obtained from the streamwise decay, $\epsilon \approx \epsilon_{dk}$ and $\eta \approx \eta_{dk}$. The data collapses nicely at high wavenumbers, which suggests a universal behavior for all grids. Further, the agreement is also very good between LDA and HFA spectra, which were available for the streamwise velocity only. Due to a large variance at high wavenumbers and a limited sample size, the LDA spectra cover only a small portion of the entire turbulence spectrum. In particular, it was not possible to resolve the viscous dissipation region, that is, the wavenumber range above $\kappa_1 \eta = 0.1$. Nonetheless, the large scale features and the range that seems to have a power-law scaling were captured. The upper two curves in both, the longitudinal and the lateral spectra correspond to the two grids with the large tethered beads. They reflect the increased kinetic energy compared to the reference grid. The other grids, the G6, W6 and W8 grid, differ very little from the RTG.

To study the power-law scaling region in a turbulence spectrum it is customary^{98, 115} to work with compensated spectra of the form $\phi_{ii} \epsilon^{-2/3} \kappa_1^{5/3}$. Figure 4.11 shows these spectra for the tested grids. The data are presented together with eighth-order log-log polynomial fits of $\phi_{ii}(\kappa_1)$. To appreciate the quality of the fit, the measured data of the ITG is also plotted, although sparsely. If the spectra indeed present a Kolmogorov scaling region, this portion of the spectrum should fall on the horizontal dashed lines, which mark the Kolmogorov constants α_1 and α_2 . None of the tested grids reaches the constant values, which means that none of these spectra scale according to the Kolmogorov spectrum defined as $\phi_{ii} = \alpha_i \epsilon^{2/3} \kappa_1^{-5/3}$.

There is little difference with the G6, W6 and the W8 grid with respect to the RTG (they correspond to ③ in figure 4.11). Only the W12 grid (②) and the ITG (①) possess a small portion that has a constant slope, extending over roughly one decade (indicated by the arrows). This indicates a power-law region, but with a slope different from $-5/3$. One notices also that these constant slopes are not the same for the u_1 - and the u_2 -spectrum, and therefore, the energy transfer from the large to the small scales is different. A possible reason for this anisotropy could be an energy transfer from longitudinal to lateral scales caused by the initial anisotropy of the turbulence.

Figure 4.12 shows the ratio between the u_1 - and u_2 -spectrum measured with LDA. In turbulence with a sufficiently high Re_λ to develop an inertial subrange,

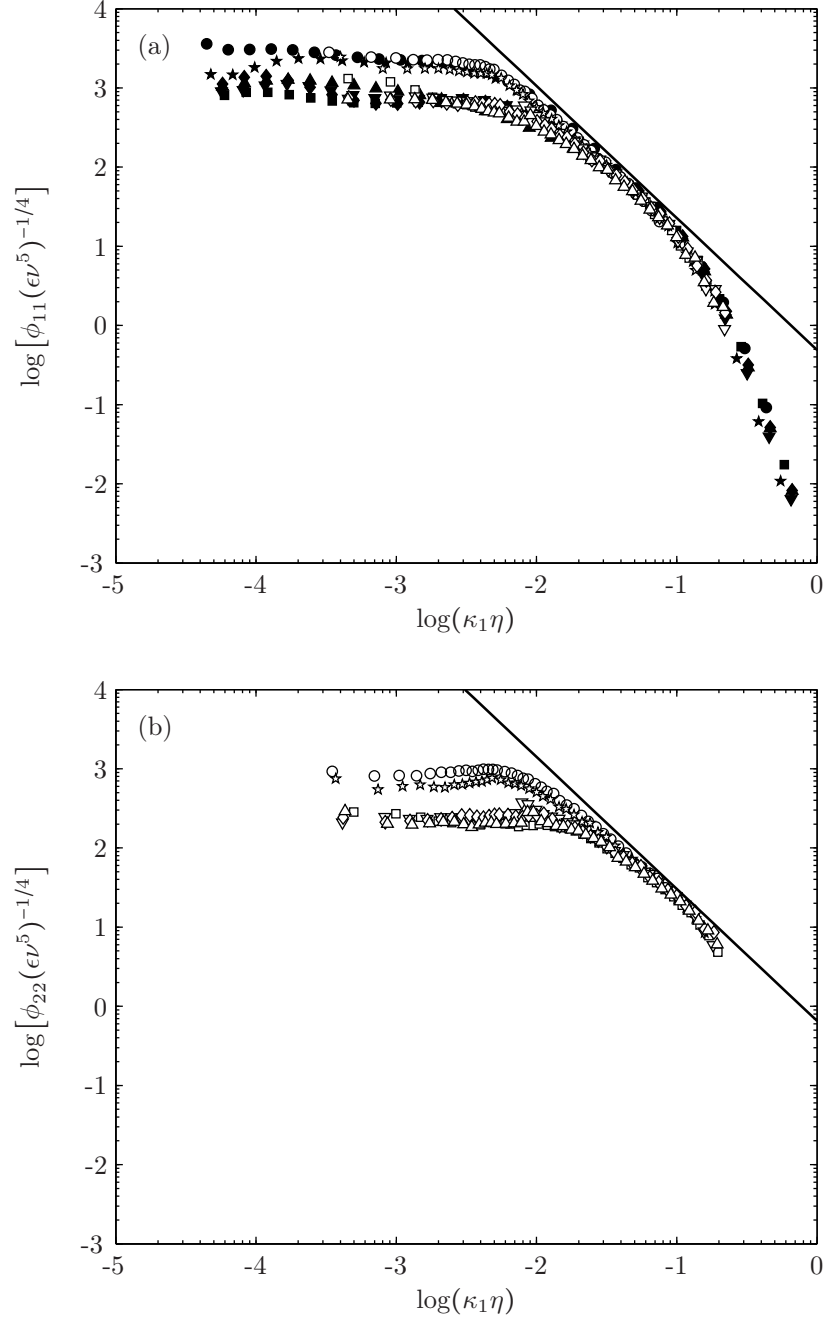


FIGURE 4.10 Longitudinal and lateral velocity spectra measured with LDA (open symbols) and HFA (solid symbols) at $x_1/M = 30$: \square, \blacksquare , RTG; $\triangle, \blacktriangle$, G6 grid; \diamond, \blacklozenge , W6 grid; $\nabla, \blacktriangledown$, W8 grid; \star, \blackstar , W12 grid; \circ, \bullet , ITG. For clarity, not all spectral samples obtained with LDA are shown, and the HFA points were evaluated with an eighth-order polynomial function. The solid lines give the Kolmogorov scaling: (a) $\alpha_1(\kappa_1 \eta)^{-5/3}$ and (b) $\alpha_2(\kappa_1 \eta)^{-5/3}$.

4.4 VELOCITY SPECTRA

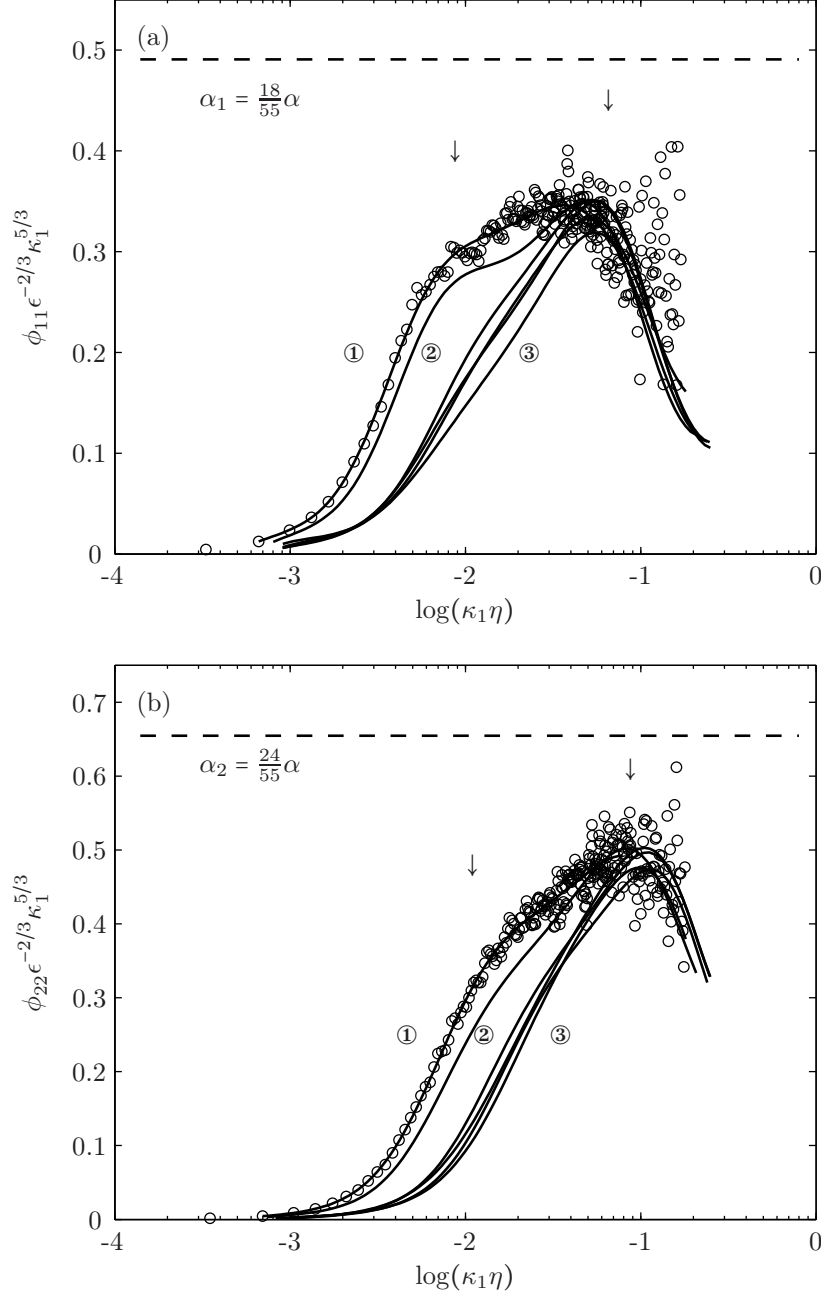


FIGURE 4.11 Spectra compensated for the scaling region: (a) longitudinal and (b) lateral spectra measured with LDA at $x_1/M = 30$. For clarity, eighth-order log-log polynomial fits (solid lines) to the data (\circ , example with sparsely plotted data of the ITG) are presented. ①, ITG; ②, W12 grid; ③, RTG, G6, W6 and W8 grid. The dashed lines indicate the Kolmogorov constants α_1 and α_2 , respectively, where $\alpha = 1.5$. The arrows designate the start and the end of the scaling region of the ITG.

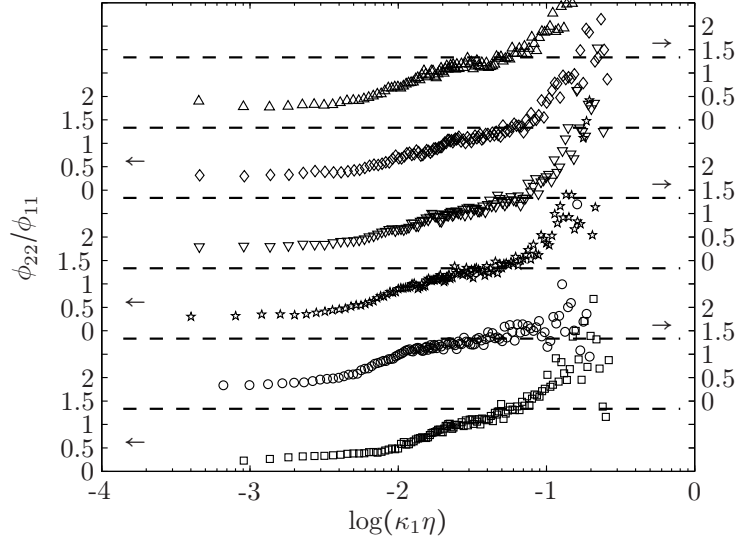


FIGURE 4.12 Ratios of the transverse to longitudinal spectra measured with LDA at $x_1/M = 30$: \square, \blacksquare , RTG; $\triangle, \blacktriangle$, G6 grid; \diamond, \blacklozenge , W6 grid; $\nabla, \blacktriangledown$, W8 grid; \star, \blackstar , W12 grid; \circ, \bullet , ITG. For clarity, not all spectral samples are shown. The dashed lines indicate $\alpha_2/\alpha_1 = 4/3$.

the small scales are assumed to be isotropic (i.e., locally isotropic), and the ratio ϕ_{22}/ϕ_{11} becomes constant in this scaling region. Thus, ϕ_{22}/ϕ_{11} allows to identify the portion of the spectrum with locally isotropic turbulence. Moreover, at low wavenumbers the ratio is 1/2 for turbulence satisfying large scale isotropy (cf. (1.3)). Figure 4.12 demonstrates the problem with low Reynolds number grid turbulence: the ratio at low wavenumbers is less than one half, and there exists no horizontal plateau at intermediate wavenumbers. Furthermore, although there is a scaling region identified for the ITG in figure 4.11, its unequal slopes imply no constant ratio ϕ_{22}/ϕ_{11} . The broken lines in figure 4.12 indicate where the plateau for a $-5/3$ power-law scaling would be. In the dissipation range, the ratio increases caused by the exponential decay of the two spectra, and the estimator variance becomes important.

Examining the effect of the bead weight, figures 4.10 and 4.12 reveal that the G6 grid introduces no noticeable variation into the spectrum compared to the plain grid.

Although none of the tested grids exactly satisfy local isotropy and the Kolmogorov scaling, the ITG is a better approximation to these conditions. It exhibits a small, but yet noteworthy constant scaling region, and the figure 4.12 suggests that the small scales are not far from an isotropic state.

4.4 VELOCITY SPECTRA

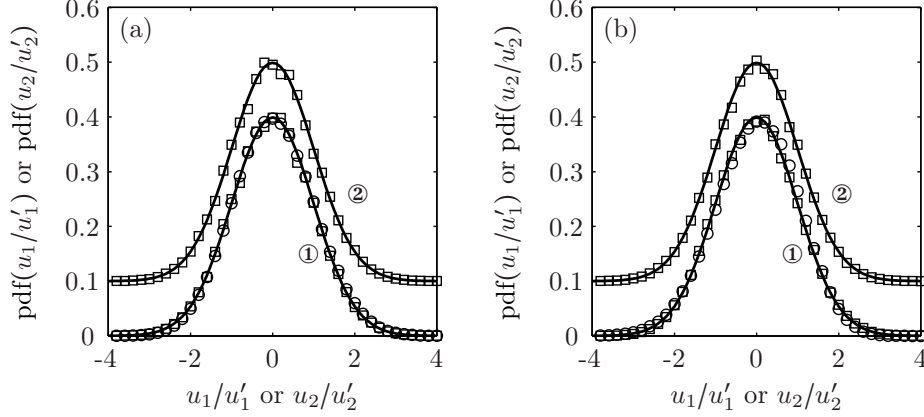


FIGURE 4.13 Velocity probability density functions of (a) the RTG and (b) the ITG: ①, u_1 ; ②, u_2 ; ○, HFA; □, LDA; solid lines, Gaussian distributions. The u_2 -pdf was shifted upwards by 0.1 on the ordinate.

TABLE 4.2 Skewness, S_{u_i} , and kurtosis, K_{u_i} , of velocity distributions for the RTG and the ITG.

Grid	S_{u_1}	S_{u_2}	K_{u_1}	K_{u_2}
RTG	0.035	0.006	2.990	2.990
ITG	0.017	-0.038	2.910	3.002

4.4.2 IMPROVED TURBULENCE GRID

Because only the ITG consists of a significant improvement over the reference grid, it is the only one considered for a further characterization of its turbulence properties.

Probability distributions of uncorrected velocity fluctuations are plotted in figure 4.13 for these two grids, together with the corresponding Gaussian curves. For clarity, the u_2 -probability density function (pdf) was shifted by 0.1 on the ordinate. The skewness S_{u_i} ($\equiv \langle u_i^3 \rangle / \langle u_i^2 \rangle^{3/2}$) and kurtosis K_{u_i} ($\equiv \langle u_i^4 \rangle / \langle u_i^2 \rangle^2$) of the u_1 - and u_2 -pdfs for both grids are given in table 4.2. Generally, they are close to the values for a Gaussian distribution, that is, zero skewness and a kurtosis of three. They are also comparable to the values determined by Mohamed and LaRue⁹⁶ or Makita⁹⁰. Mohamed and LaRue⁹⁶ further highlights that the skewness S_{u_1} deviates from zero in non-isotropic turbulence. At a similar distance from the grid, they find u_1 -skewness values between -0.01 and 0.04 for various grid Reynolds numbers. Based on the values of the skewness S_{u_1} , the turbulence generated by the improved grid is closer to isotropy than the reference grid.

Figures 4.14 and 4.15 show the spectra of the RTG and the ITG, respectively, as estimated from data acquired with all three measurement techniques. They replot data from figure 4.10, but this time with an absolute scaling. The collapse of

the data at high wavenumbers is reasonable, considering that the PIV and LDA measurements contained high noise levels. Moreover, these measurements were realized several months apart, and their agreement emphasizes the good repeatability of the experiment.

Only the lateral PIV spectra showed a systematic underestimation of the large scale energy content, compared to the LDA. This could come from the limited field of view, which does not allow to capture the largest scales of the flow¹⁴⁷. Practically speaking, the smallest resolvable wavenumber with PIV is more than an order of magnitude larger than that with LDA.

To determine the extent of local isotropy, the measured spectrum ϕ_{22} was compared to the ϕ_{22} computed from the measured ϕ_{11} , using the isotropic relation¹⁰⁷

$$\phi_{22}(\kappa_1) = \frac{1}{2} \left[\phi_{11}(\kappa_1) - \kappa_1 \frac{\partial \phi_{11}(\kappa_1)}{\partial \kappa_1} \right], \quad (4.12)$$

where the differential was obtained from the polynomial fits to the HFA data. These spectra are indicated by the solid lines in figures 4.14 and 4.15. In the former figure, the turbulence was found to be closely locally isotropic for wavenumbers larger than 200 1/m , and 500 1/m respectively for the latter. Taking into account that the smallest length scales, η , of these two grids are very similar (cf. table 4.3), the ITG marginally reduces the wavenumber range over which the small scales are isotropic. On the other hand, the two figures show that the isotropy at large scales is slightly improved, that is, the difference between the measured ϕ_{22} and the ϕ_{22} from equation (4.12) is diminished.

The insets in both figures show the $\kappa_1 \phi_{ii}$ spectra, where the energy was normalized with the squared rms velocity. One notices that the tethered beads shift the energy peak towards lower wavenumbers, and also that they are narrower. The relative energy contained in the lateral spectrum peak is about 25 % for both grids, whereas in the case of the streamwise spectrum the ITG shows a higher peak. Based on the observation described in section 3.2 that the Strouhal number of the tethered spheres is roughly 0.1, one can deduce a shedding frequency of 10 Hz, or equivalently, a shedding wavenumber of 52 1/m for the ITG. This coincides with the wavenumber of the longitudinal energy peak, but does not reach into the scaling region, which is indicated by the arrows in figure 4.15.

Accepting that the integral length scales coincide with the peaks of $\kappa_1 \phi_{ii}$, the ITG generates turbulence with larger integral scales, which is indicated by the peaks shifted towards lower wavenumbers. In fact, the contrary is found for the streamwise integral scale when it is computed from the correlation function (cf. table 4.3). Hence, the peak of $\kappa_1 \phi_{11}$ in figure 4.15 is the effect of the tethered sphere, and affected the wavenumbers just below the streamwise integral scale.

4.5 CORRELATION FUNCTIONS AND LENGTH SCALES

Figure 4.16 shows the streamwise and the transverse correlation functions, respectively, computed from the corresponding LDA spectra of figure 4.10. Only a re-

4.5 CORRELATION FUNCTIONS AND LENGTH SCALES

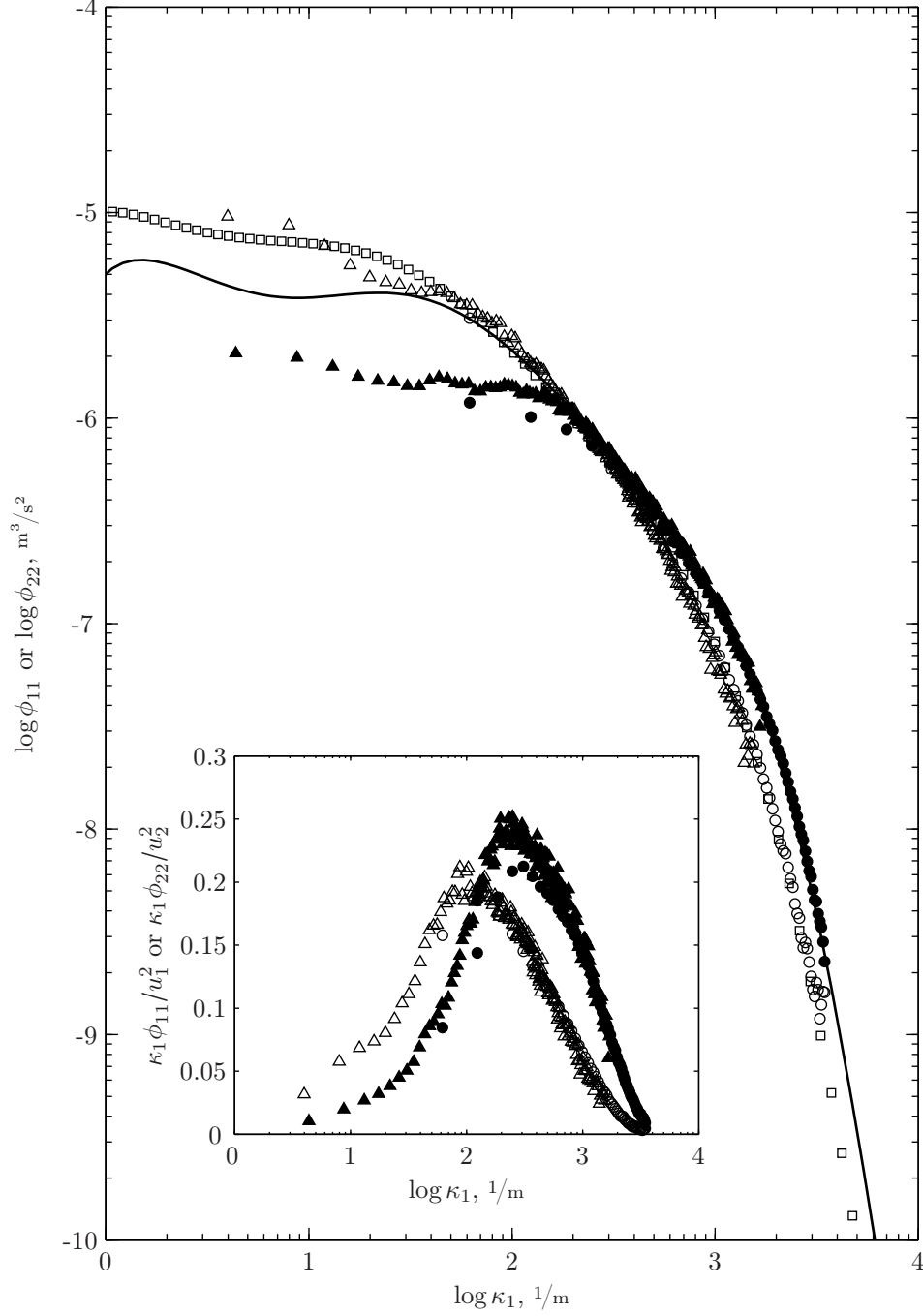


FIGURE 4.14 Longitudinal (open symbols) and lateral (solid symbols) velocity spectra of the RTG, measured at $x_1/M = 30$: \square , HFA; \triangle , \blacktriangle , LDA; \circ , \bullet , PIV. The solid line represents ϕ_{22} calculated from ϕ_{11} (\square) using isotropic relation. The inset shows $\kappa_1 \phi_{11}/u_1^2$ and $\kappa_1 \phi_{22}/u_2^2$ measured with LDA and PIV. For clarity, not all spectral samples obtained with LDA are shown.

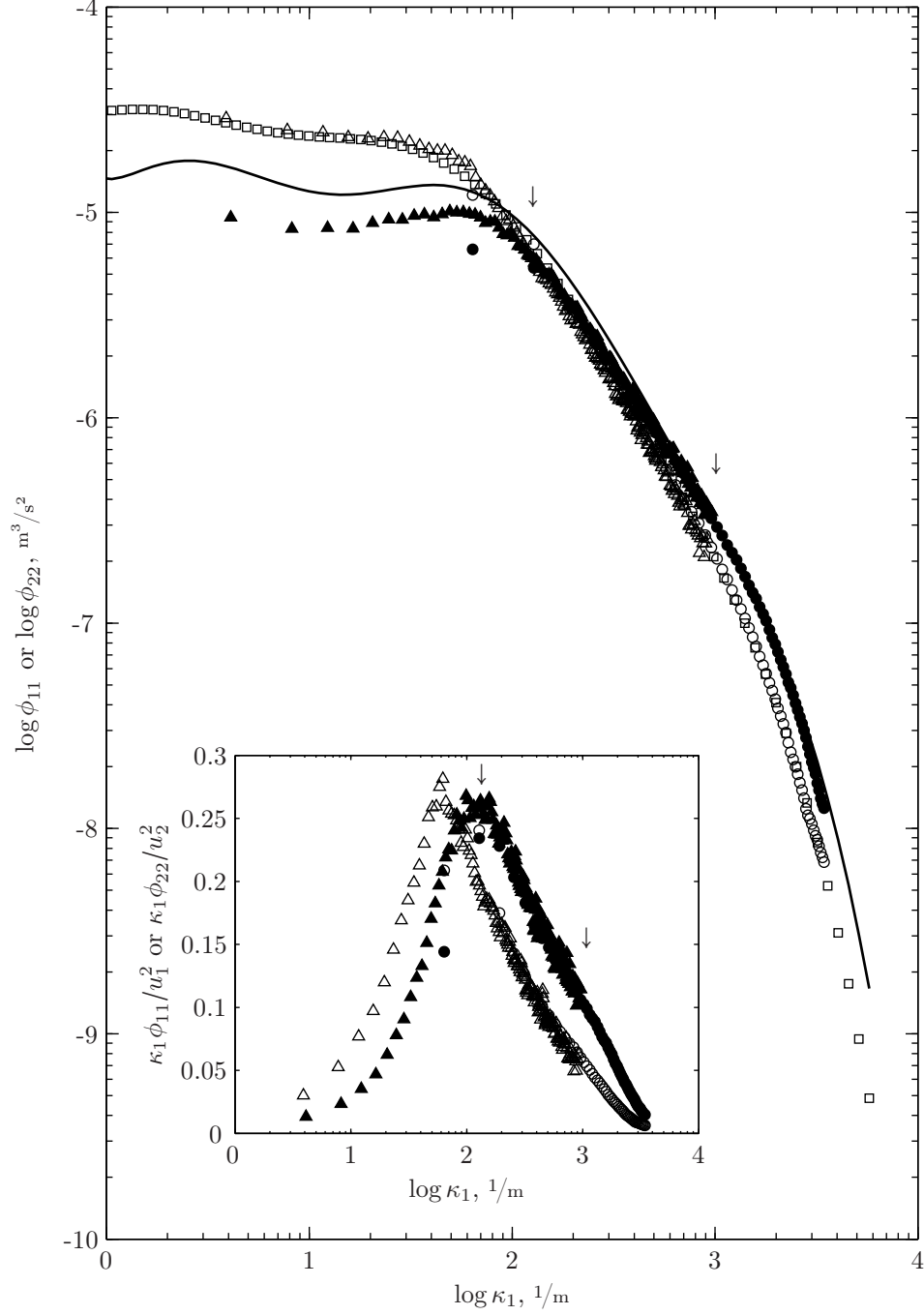


FIGURE 4.15 Longitudinal (open symbols) and lateral (solid symbols) velocity spectra of the ITG, measured at $x_1/M = 30$: \square , HFA; \triangle , \blacktriangle , LDA; \circ , \bullet , PIV. The solid line represents ϕ_{22} calculated from ϕ_{11} (\square) using isotropic relation. The inset shows $\kappa_1 \phi_{11}/u_1^2$ and $\kappa_1 \phi_{22}/u_2^2$ measured with LDA and PIV. For clarity, not all spectral samples obtained with LDA are shown. The arrows mark the start and the end of the scaling region.

4.5 CORRELATION FUNCTIONS AND LENGTH SCALES

TABLE 4.3 Summary of turbulence length scales and dissipation rates at $x_1/M = 30$ obtained from streamwise decay (dk), correlation coefficients (B_{11} and B_{22}), HFA spectra (iso), and direct measurement with PIV under the assumption of axisymmetry (axi). The turbulence Reynolds number Re_λ was deduced from decay properties.

Grid	Re_λ	ϵ_{dk} cm^2/s^3	ϵ_{iso} cm^2/s^3	ϵ_{axi} cm^2/s^3	η_{dk} mm	λ_{dk} mm	$\lambda_{B_{11}}$ mm	$\lambda_{B_{22}}$ mm	Λ_1 mm	Λ_2 mm
RTG	68	44.8	29.9	50.8	0.11	1.8	2.2	2.0	15.4	4.6
ITG	123	148.2	88.5	145.4	0.09	1.8	2.7	2.7	13.3	6.2
W12	148	122.5	57.7	—	0.09	1.6	2.5	2.3	12.8	5.6
W8	84	60.4	32.0	—	0.11	1.7	2.6	2.4	10.1	3.8
W6	77	55.5	34.2	—	0.11	1.7	2.5	2.4	9.6	4.2
G6	66	53.0	31.8	—	0.11	1.6	2.1	2.0	11.2	3.8

duced number of points are plotted to avoid cluttering the graph, and the r_1 -axis is logarithmic. The LDA spectra showed a considerable level of noise in the last decade. Therefore, this region was cut off before the spectra were converted, and the obtained results agreed well with correlation functions computed from HFA measurements. Of course, only the longitudinal components were compared. Processing the lateral component in the exact same way, it was assumed that the results are of equal quality. All correlation functions obtained with this procedure were consistent. To avoid redundancy, the HFA data are not presented here. The dynamic range of PIV measurements, on the other hand, was too poor to obtain adequate correlation functions. In particular, the small scales were not resolved sufficiently to detect the parabolic region, and for an estimation of the integral scale the field of view was not large enough. Typically, the largest detectable structure should be at least an order of magnitude greater than the integral scale¹⁴⁷.

Little differences exist between the correlations of the various grids, and only the W12 grid and the ITG are distinguishable from the rest. All grids exhibit a small portion where the correlation of u_2 is negative¹³⁴, although the one of the RTG is very small.

These correlation functions allowed to calculate the longitudinal and lateral integral scales, Λ_1 and Λ_2 , as well as the Taylor microscale λ tabulated in table 4.3. Practically speaking, the integral length scales defined in (3.30) were found by integration of the correlation coefficients up to the first zero-crossing point, with the exception of the coefficients of the W8 grid. The latter presented two large oscillations that were also taken into account for the integral. The method described in section 3.8 was applied to acquire estimates of the Taylor length scale from both correlation functions, B_{11} and B_{22} . In figure 4.16, the parabolae to the correlation coefficients of the RTG (cf. solid lines) are shown as an example. The Taylor length scale is then given by the intersection of the parabolae with the r_1 -axis.

A summary of all acquired values for Λ_1 , Λ_2 and λ is given in table 4.3, together with estimates for λ and ϵ from other measurements, such as the streamwise decay and the direct measurement of the dissipation rate. Looking at the integral scales, it appears that the plain grid has the largest Λ_1 , and also the smallest ratio between

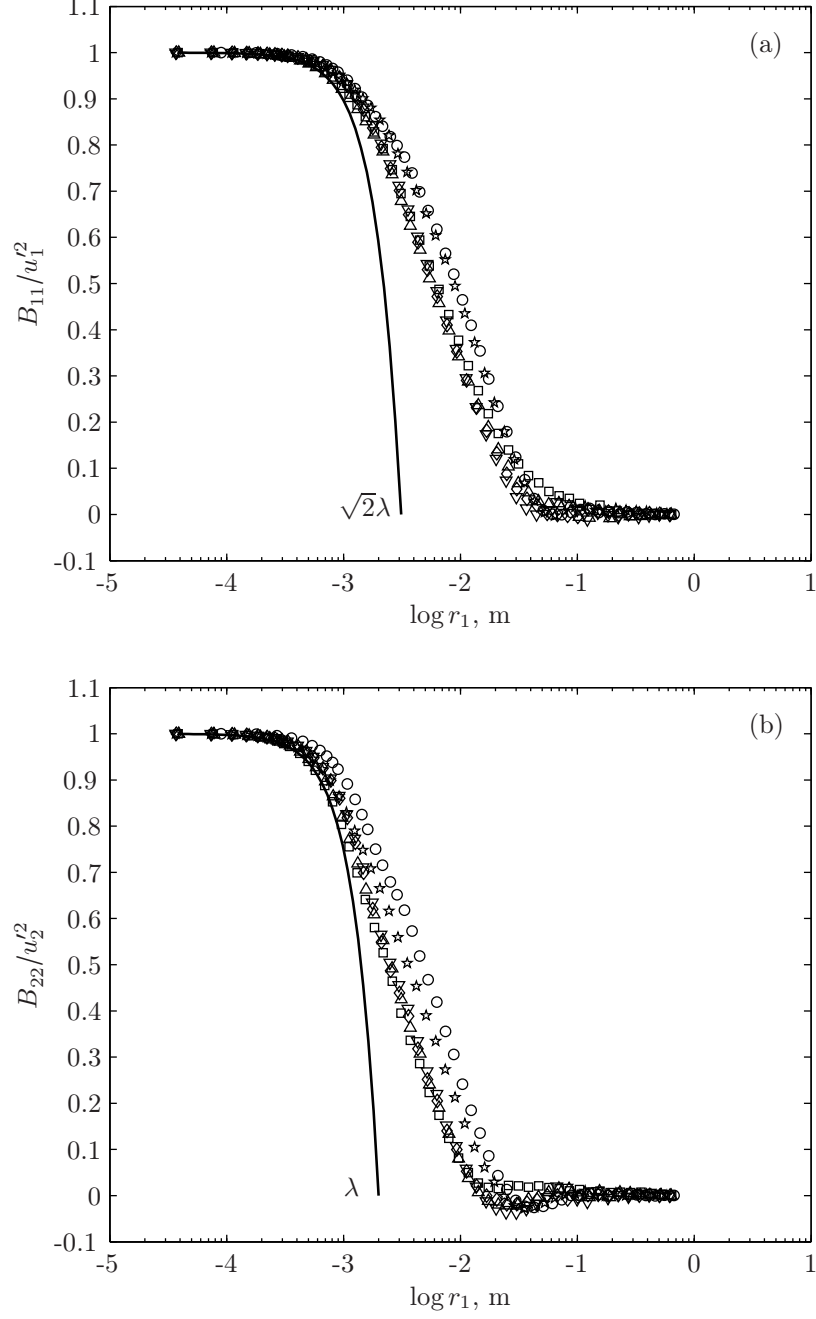


FIGURE 4.16 (a) longitudinal and (b) lateral correlation coefficient measured with LDA at $x_1/M = 30$: \square , RTG; \triangle , G6 grid; \diamond , W6 grid; ∇ , W8 grid; \star , W12 grid; \circ , ITG. For clarity, only a reduced number of points is shown. The solid lines are an example of the fitted parabola, given for the RTG.

4.6 DIRECT MEASUREMENT OF THE DISSIPATION RATE

Λ_2 and Λ_1 . The grids equipped with tethered spheres on the other hand, produce smaller streamwise integral scales and their Λ_2 to Λ_1 ratio is closer to the isotropic value of one half¹⁰⁷. The grids producing turbulence closest to large-scale isotropy are notably the W12 grid and the ITG.

The Taylor microscales estimated from the correlation functions are indicated with the according subscript. They are, in contrast, all very close to 2.3 millimeters, regardless of the grid and the correlation function used for the estimation. This supports the earlier finding that the small scales of the turbulence are isotropic and universal for all tested grids. However, the indirect approach gave somewhat different results: the length scales λ_{dk} are consistently smaller than the ones found with the correlation functions. This suggests that the dissipation rate of energy is either underestimated in the spectrum measurements, or it is overestimated by the streamwise decay. To this end, PIV measurements were realized on five different streamwise locations, with the goal to measure the turbulence intensity and the dissipation rate; the latter directly, without referring to equation (4.9) (cf. the following section).

Table 4.3 also specifies the turbulence Reynolds numbers based on the Taylor scale determined from the decay. The value of Re_λ ($\equiv \lambda u'_1/\nu \approx \lambda\sqrt{q^2/3}/\nu$) increases with the diameter of the tethered spheres, and for the ITG it is almost twice as large as for the plain grid.

4.6 DIRECT MEASUREMENT OF THE DISSIPATION RATE

The dissipation rate of turbulence energy defined by equation (1.9) was directly determined from the PIV velocity fields using the expression for a flow field symmetric about the x_1 -axis,

$$\epsilon_{\text{axi}} = \nu \left[2 \left\langle \left(\frac{\partial u_1}{\partial x_1} \right)^2 \right\rangle + 3 \left\langle \left(\frac{\partial u_2}{\partial x_2} \right)^2 \right\rangle + 3 \left\langle \left(\frac{\partial u_1}{\partial x_2} \right)^2 \right\rangle + 3 \left\langle \left(\frac{\partial u_2}{\partial x_1} \right)^2 \right\rangle + 4 \left\langle \frac{\partial u_2}{\partial x_1} \frac{\partial u_1}{\partial x_2} \right\rangle \right], \quad (4.13)$$

where the terms involving the velocity component or the derivative in the x_3 -direction were substituted by equivalent terms in the x_2 -direction. Only the mixed term involving the x_2 - and x_3 -direction had to be replaced with an isotropic expression¹⁰⁷.

In case of truly isotropic turbulence, equation (1.9) can be reduced to¹³⁴

$$\epsilon_{\text{iso}} = 15\nu \left\langle \left(\frac{\partial u_1}{\partial x_1} \right)^2 \right\rangle. \quad (4.14)$$

This, in turn, is a rough approximation of the true dissipation rate, as the streamwise velocity fluctuations are more intense than the two lateral velocities.

Figure 4.17 shows the results for the RTG and the ITG, applying these equations to the same PIV maps as in figures 4.5 and 4.6. Again, the noise and filtering corrections described in section 3.5 were calculated for the five measurement

locations, and then interpolated with a quadratic least squares fit for positions in-between.

Regarding the dissipation rate derived from the streamwise turbulence energy decay (4.9), which are indicated by the solid lines, the equations (4.13) and (4.14) produce reasonably good results. In particular, the results for the ITG agree well with the decay data. The discrepancy between ϵ_{axi} and ϵ_{dk} for the plain grid, could result from the inferior signal to noise ratio. Nonetheless, the dissipation rate ϵ_{axi} is still within the 95 % confidence intervals of ϵ_{dk} .

As expected, the isotropic approach overestimates the dissipation rate for both grids, although, the difference between the results for equations (4.13) and (4.14) is small for the ITG. Moreover, at locations close to the grid, the grid wake effects are stronger and, hence, the inequality between the velocity component statistics is larger. This is reflected by the increasing gap between ϵ_{axi} and ϵ_{iso} for decreasing x_1/M .

The values of ϵ_{axi} at $x_1/M = 30$ for the two grids, the RTG and the ITG, are given in table 4.3. No PIV measurements have been realized for the other grids.

As stated by Monin and Yaglom⁹⁷, the expression (4.14) is equivalent to the integral of the dissipation spectrum, that is,

$$\epsilon_{\text{iso}} = 15\nu \int_0^\infty \kappa_1^2 \phi_{11}(\kappa_1) d\kappa_1. \quad (4.15)$$

This equation requires a good resolution of the small scales in order to capture the entire dissipation range. Practically speaking, only the HFA has a sufficiently high sampling frequency, and consequently, the spacial derivative of (4.14) is approximated by a temporal derivative using Taylor's frozen turbulence hypothesis. Equation (4.15) was evaluated for HFA spectra acquired for all tested grids, and the obtained values of ϵ_{iso} are presented in table 4.3.

As mentioned earlier, the distance downstream of the turbulence grid available to explore the streamwise decay was very limited. Generally in such experiments, decay laws are fitted to turbulence intensities measured at distances much larger than fifty meshes from the grid. Kurian and Fransson⁷⁸ even states that the power-law region begins at $x_1/M > 60$. Nevertheless, it was assumed in section 4.3 that there exists a power-law decay for $x_1/M > 20$. To verify this assumption in the case of the two major grids, the ratio between the squared Taylor length scale, λ^2/M^2 , and the streamwise distance x_1/M is plotted in figure 4.18. By means of the relations (4.4) and (4.9), the Taylor microscale can be expressed as

$$\lambda^2 = 5\nu \frac{q^2}{\epsilon} = \frac{10\nu x_1}{U_0 n_{\text{dk}}}. \quad (4.16)$$

It follows that the ratio

$$\frac{\lambda^2 M}{M^2 x_1} = \frac{10\nu}{U n M} \quad (4.17)$$

is constant for a power-law decay.^{6, 147} In the corresponding plot, figure 4.18, the measured dissipation rates ϵ_{axi} from figure 4.17 were used together with the analytical expression (4.4) for q^2 . The scatter in the resulting plot comes from the

4.6 DIRECT MEASUREMENT OF THE DISSIPATION RATE

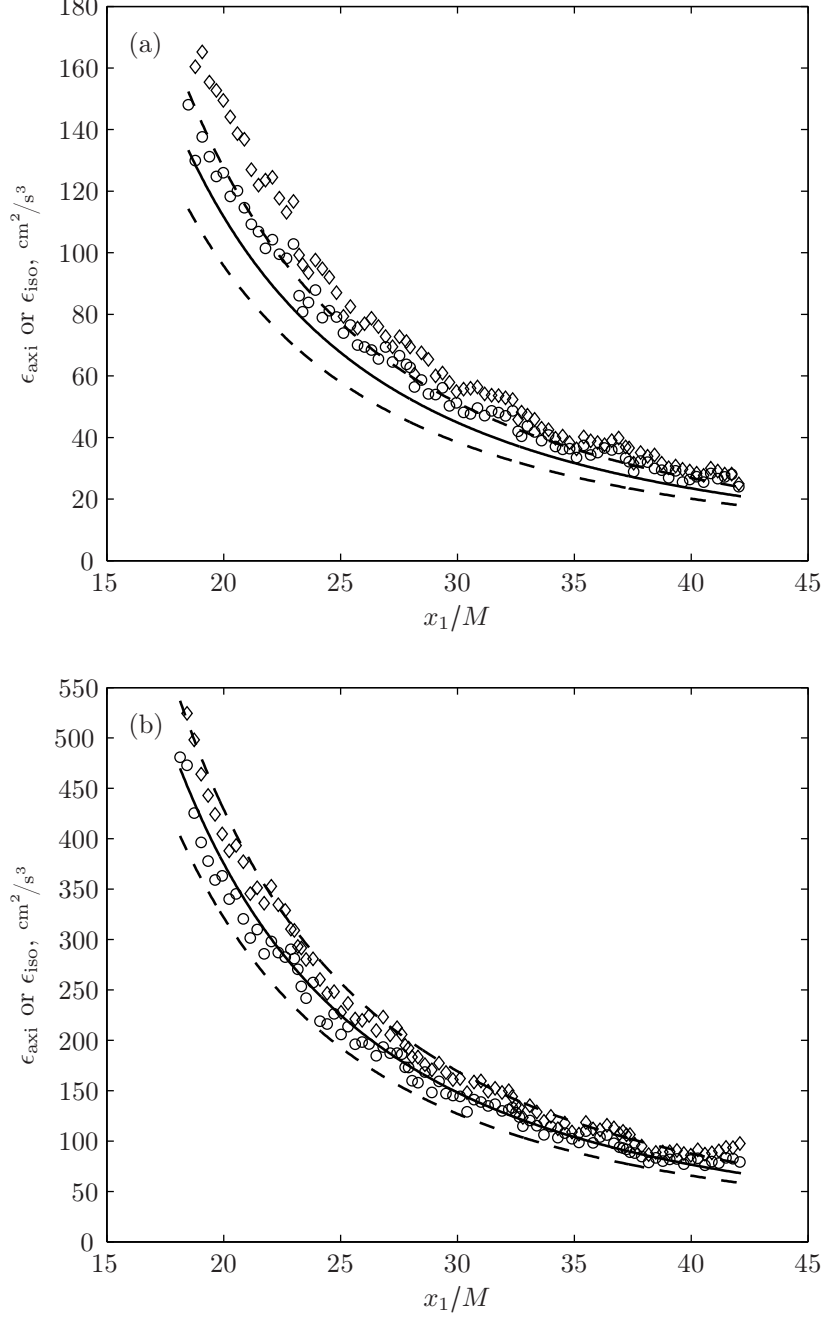


FIGURE 4.17 Turbulence energy dissipation rate of (a) the RTG and (b) ITG, measured directly with PIV: \circ , axisymmetric assumption (4.13); \diamond , isotropic assumption (4.14). The solid and broken lines represent the dissipation rate derived from the turbulence energy decay (4.9) with its 95 % confidence intervals.

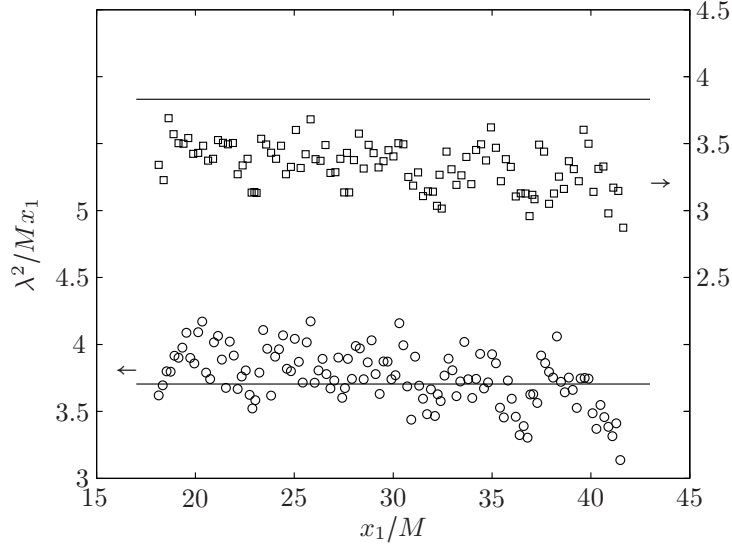


FIGURE 4.18 Streamwise evolution of the ratio λ^2/Mx_1 for the RTG (\square) and the ITG (\circ). Only a fraction of the available points are presented. The solid lines correspond to the ratio in case of a power-law decay, that is, $10\nu/UnM$.

random PIV measurement error, but the data still support the power-law fitted to the measured streamwise decay of energy, albeit both data sets drift away from the constant value. The gap between the ideal and the measured ratio for the RTG probably arises from an overestimation of the dissipation rate. However, Antonia et al.⁶ illustrates that with an appropriate virtual origin in the power-law, the present ratio can be altered. Thus, they use this particular plot to determine a suitable value for the virtual origin. However, the virtual origin can also be regarded as a trick to force a power-law.

4.7 CONCLUDING REMARKS

The new passive grids equipped with tethered beads are capable of enhancing the turbulence properties; notably the grid with the largest beads increased the Reynolds number Re_λ by a factor of roughly two, as indicated by table 4.3. This is primarily due to the increase in turbulence intensity, as the Taylor length scales remained virtually unchanged for all tested grids.

The most promising grid is the ITG, which generates turbulence homogeneous over planes normal to the streamwise direction, and decays in the streamwise direction according to a power-law. Furthermore, this grid improves the large-scale isotropy, albeit a small difference between streamwise and transverse turbulence intensities persists. It also verifies local isotropy, which was the case for all tested grids.

There are at least two possible mechanisms involved in the turbulence produc-

4.7 CONCLUDING REMARKS

tion behind the new grids: the increased pressure drop that could also be achieved by increasing solidity of the a plain grid, and the vortex shedding from the spheres. The results above suggest that the shedding from the beads appreciably contributes to the turbulence production only in the case of the large beads. For all the other grids with tethered spheres, this mechanism was overshadowed by the ‘conventional’ turbulence generation.

Only two geometrical grid parameters have been explored, that is, the diameter and the relative mass per unit volume of the tethered spheres. The results showed that light and large beads are favorable for introducing large velocity fluctuations into the flow. Grids with smaller spheres, heavy or light, had only moderate effects. Other parameters, such as the tether length or the shape of the beads, have not been studied. This leaves many open questions. For example, the tether length was chosen for convenience, but it may have an effect on the oscillating motion. So does the relative bead weight^{57, 151}, which was not stressed enough in the present study. For example, it was observed that the turbulence intensity was lower for the heavier than for the lighter beads of the same size. This may result from dampened oscillation amplitudes^{57, 151}.

Finally, the ITG offers a simple solution for high Reynolds number turbulence, but which is still one order of magnitude below the Reynolds numbers achieved with other turbulence enhancing grids, such as active grids^{90, 98} or fractal grids^{66, 119}. Yet, there is still some room for improvement, possibly with even larger beads of shapes other than spherical.

CHAPTER 5

Grid turbulence in polymer solutions

5.1 BRIEF OVERVIEW

This chapter covers the experiments on the effects of fluid elasticity on grid generated turbulence. In particular, it will treat the velocity spectra and the dissipation rate of energy obtained from PIV measurements with respect to a recent theoretical model⁴⁹. Based on the latter and the present experimental results, a slightly modified model spectrum is depicted in the final section of this chapter, including a summary of the most important findings. Furthermore, a new simplistic cascade model is introduced to describe the evolution in time of quantities influenced by degrading polymers.

5.2 EXPERIMENTAL CONDITIONS

All experiments were realized using the ITG with the same boundary conditions as in the experiments reported in the preceding chapter. Strictly speaking, these were a constant pump rotation speed generating a mean flow velocity U_0 of approximately 1.20 m/s , as well as nearly the same temperature for all fluids.

Three different polymer concentrations were investigated: 25, 50 and 100 wppm, which were determined from the respective weights of polymers added to the water in the flow facility.* The uncertainty which arises from the error made on the calculation of the tunnel volume is roughly 4 % of the nominal concentration. Another estimate of the concentration was obtained by means of equation (2.25a) from a fluid sample taken shortly before the beginning of the experiment. These values are twenty percent below the apparent concentrations (cf. table 5.1). This is most probably due to the addition of 0.04 wt% NaCl, which was added to the parent solution to reduce the preparation time. Therefore, the salt had a much larger effect on the polymer coils than initially expected (cf. section 2.4). In this case, the low viscosity is consistent with the idea that salt reduces the polymer coil diameter, resulting from a weaker polymer-solvent interaction.¹⁵³ Consequently, elastic effects might be affected as well and should be interpreted with care.

*Although the used polymer concentrations seem relatively small, 100 wppm corresponds to 1.5×10^{19} polymers per cubic meter. This yields roughly 10^6 polymers in a volume of the size of a viscous eddy, that is, the Kolmogorov scale ($\approx O(0.1) \text{ mm}$).

GRID TURBULENCE IN POLYMER SOLUTIONS

TABLE 5.1 Experimental conditions including estimates of the concentration c_v deduced from the solution viscosity ν . The values of U_0 and Re_M were evaluated at the end of each experiment.

Symbol	c wppm	c_v wppm	m_{peo} g	ν mm^2/s	ν_s mm^2/s	τ_R ms	T $^\circ\text{C}$	U_0 m/s	Re_M $\times 10^{-3}$
\diamond	25	24	180	0.99	0.95	3.4	22.2	1.18	19.1
\circ	50	42	360	1.04	0.98	5.4	21.1	1.21	18.6
\square	100	82	720	1.07	0.95	8.8	22.2	1.21	18.1

Table 5.1 summarizes the experimental conditions, including the fluid viscosity at the actual temperature of the solution during the experiment, the mass of polymers m_{peo} added to the tunnel, and the two different estimates of the polymer concentration c and c_v . It also specifies the polymer relaxation time τ_R computed with the empirical relation (2.30). Based on the Kolmogorov time scale $t_K (\equiv \sqrt{\nu/\epsilon})$ which was of the order of 8 ms in pure water, the Weissenberg numbers $Wi (= \tau_R/t_K)$ were below one for all concentrations. In view of the viscoelastic effects reported in the next sections, this seems odd. Berti et al.¹⁷, for example, found a critical Weissenberg number larger than one which has to be exceeded in order to observe viscoelastic effects. However, one should note that the polymer relaxation time was not measured directly, and thus, could be much larger than expected because of polymer networks present in the solution.

Another indicator if the elastic degrees of freedom will be excited or not in the turbulent flow is the Reynolds number

$$Re_{cs} = \left(\frac{\Lambda^2}{\nu\tau} \right)^{2/3} \quad (5.1)$$

associated with the *coil-stretch transition*.⁸ The latter corresponds to the instant when the turbulence-polymer configuration is such that the polymers start to affect the smallest turbulence scales. For Re_M below Re_{cs} the polymers are passive and the flow properties are essentially Newtonian. Taking the integral scale $\Lambda \sim M$ yields $Re_{cs} \sim O(2 \times 10^3)$, hence all flow configurations should exhibit elastic effects.

All velocity measurements were carried out with the stereo PIV setup, with the field of view located in the central x_1 - x_2 -plane 30 mesh widths downstream of the grid. The Reynolds number was of roughly 1.9×10^4 , based on the mean flow velocity U_0 given in table 5.1, which was determined at the end of each experiment. From the results in the former chapter, one expects a turbulence intensity in pure water of the order of 5% at this location.

Repetitions of the experiments with solutions of 50 and 100 wppm PEO produced virtually the same results and are not reported here.

5.3 DEGRADATION OF THE POLYMER SOLUTIONS

5.3 DEGRADATION OF THE POLYMER SOLUTIONS

Fluid and flow properties were monitored by means of viscosity measurements and the continuous recording of the pressure drop. This was necessary because Polyox WSR 301 is sensitive to mechanical breakdown.¹⁴⁰ The degrading polymers allowed to study their effects on turbulence under changing fluid elasticity, which diminishes with decreasing molecular weight. Unfortunately, the exact elastic characteristics of the evolving solutions could not be established, and rough estimates of the Weissenberg number were calculated from turbulence properties instead. The latter also appears to be an appropriate indicator for the polymer stability.

5.3.1 FLUID VISCOSITY

The viscosities of the three experiments were determined with the capillary viscometer and are shown in figure 5.1 (a) relative to the solvent viscosity. The viscosity ratios were determined for the actual temperature during the experiment. For all three fluids the viscosity underwent only moderate changes, typically of less than one percent. Only the thickest solution shows a decreasing viscosity that could result from polymer degradation. For the other two solutions, the increasing viscosity suggests that the solution was still heterogeneous, and that the samples taken contained a fraction of polymers below average.

Polymer chains of high molecular weights have been observed to break close to the midpoint, when they were subject to a turbulent flow.⁶⁵ Thus, the molecular weight is reduced by one half, whereas the concentration stays the same. Considering the relationships (2.19) and (2.25a), the expected drop in viscosity when the molecular weight is halved from 4×10^6 to 2×10^6 g/mol is 1.2, 2.5 and 5 % for the 25, 50 and 100 wppm solutions, respectively. Comparing these differences with the measured viscosities indicates that there was no such severe polymer chain degradation.

5.3.2 STATIC PRESSURE DROP

Figure 5.1 (b) shows the pressure drop coefficient across the working section averaged over time periods of 200 seconds, which corresponds to two circuits in the tunnel. It was normalized with the C_p value determined for the ITG in water (cf. previous chapter). To calculate the C_p , the change of the streamwise mean velocity $U_0 \approx \bar{U}_1$ was extrapolated from exponential fits to the mean velocity \bar{U}_1 measured with PIV. These fits are shown in figure 5.1 (c) together with the measured velocities averaged over the field-of-view. The number of PIV measurements per time step was very low, generally a random number between 40 and 60, and explains the random scatter.

The resulting pressure coefficients demonstrate drag-reducing^{88, 145} behavior for the two lower concentrated solutions. The thickest solution, on the other hand, produces a higher pressure drop coefficient. This could be explained by elastic

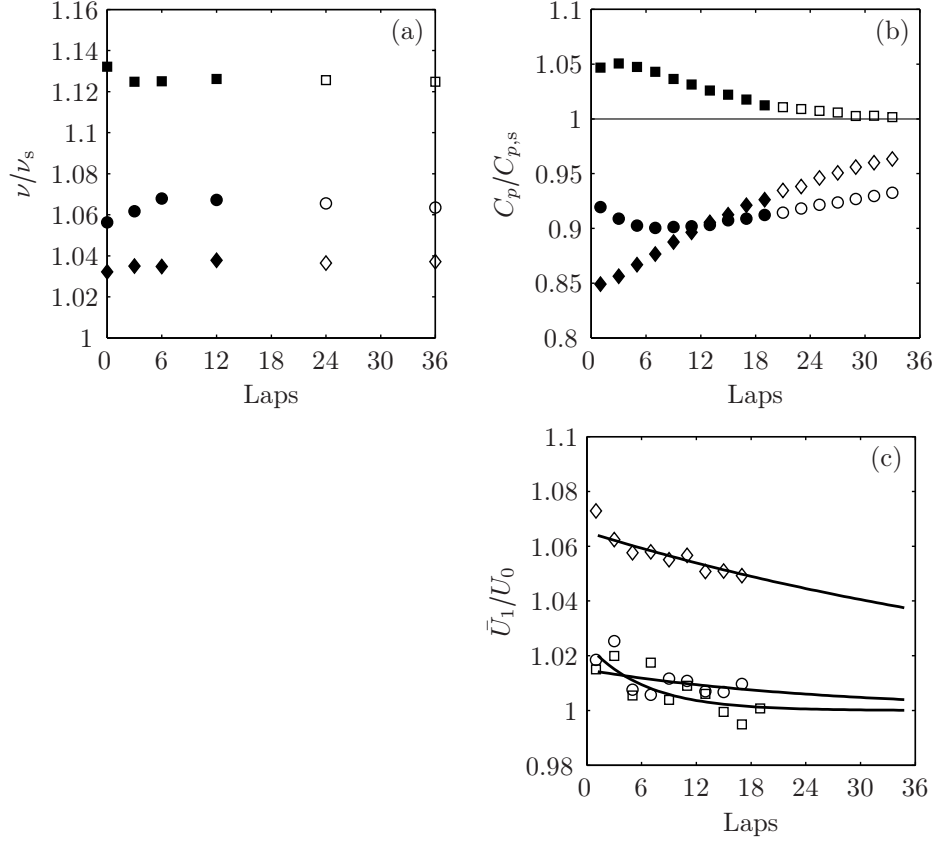


FIGURE 5.1 Evolution of (a) the fluid viscosity, (b) the pressure drop coefficient during the turbulence experiments and (c) the average streamwise velocity deduced from PIV. See table 5.1 for the values of U_0 and the symbols. Solid symbols mark the time span of the PIV measurements. The pressure drop coefficient of the pure solvent $C_{p,s} = 1.04$, and the solid lines in (c) are exponential extrapolations.

effects that are insufficient to compensate for the increase in viscosity. Friehe and Schwarz⁵¹ realized a similar experiment with another polymer type, and noted pressure drop coefficients depending on the polymer concentration, in agreement with the present measurements. Unlike the viscosity, the C_p shows a clear evolution of the flow characteristics. With the pump rotation speed and the fluid temperature kept constant, it follows that the change can be attributed to a transformation of the fluid properties. The closest conclusion is polymer degradation. Another possible cause is the breakup of polymer networks that have formed during the preparation. Both explanations result in reduced elastic properties which are directly dependent on the polymer length or network size.

However, the fluid properties changed quite rapidly, especially for the solution with the lowest polymer concentration. Assuming that this change happens slow enough to gather at least a small set of measurements with approximately con-

5.3 DEGRADATION OF THE POLYMER SOLUTIONS

stant conditions, a statistical approach is nonetheless possible. For the velocity measurements, it was assumed that the fluid and the flow properties remained unchanged over intervals of 200 seconds, allowing for averaged velocity spectra and dissipation rates. Each period corresponds to two passes in the working section. The solid symbols in figures 5.1 (a) and 5.1 (b) mark the span over which PIV recordings were acquired, that is, approximately half an hour which is equivalent to approximately 20 passes in the working section.

5.3.3 FLUID ELASTICITY

The change in elasticity due to the polymer breakup manifests itself as the approach of the polymer spectrum to the Newtonian spectrum, as can be seen in figures 5.3 to 5.5. The difference between the solvent and the polymer spectrum has almost vanished for the most degraded solutions, except for the thickest polymer solution where the energy flux at the small scales is still affected at the last time interval. This suggests that in the 100 wppm case there was still a significant fraction of intact polymer chains present in the fluid.

The curves in figures 5.6 (a) and 5.6 (b) show the Lumley scale, which will be defined further below, and the Weissenberg number as a function of passes through the test section. It reflects the integrity of the polymers and is therefore expected to follow an exponential law³², assuming that polymer chains break up at a rate that is constant over time. Polymer degradation experiments in a double-gap rheometer cell²⁰ have shown that a simple exponential function is only adequate for the early decay region, as it is the case for the present data.

Stretched exponential functions are sometimes¹²⁹ used to take into account the changing decay rate, but like the polymer conformation model by Brostow²⁴, it lacks the flexibility to adequately describe the present data. Therefore, a new (over)simplified cascade model has been developed, based on the following hypotheses: (i) the initial molecular weight is monodisperse; (ii) the polymers break at the midpoint; and (iii) the exponential decay rate depends only on the molecular weight. Furthermore, the model considers only two polymer lengths, the initial length and half the initial length. More degrees of freedom can be added as one sees fit. The temporal evolution of the weight concentrations c_0 and c_1 of the original polymer and its first breakdown product can be expressed as

$$\frac{dc_0}{d\theta} = -a_0 c_0, \quad (5.2a)$$

$$\frac{dc_1}{d\theta} = a_0 c_0 - a_1 c_1. \quad (5.2b)$$

With the initial conditions $c_0(0) = 1$ and $c_1(0) = 0$ one obtains the solutions

$$c_0(\theta) = \exp(-a_0 \theta), \quad (5.3a)$$

$$c_1(\theta) = \frac{a_0}{a_0 - a_1} [\exp(-a_1 \theta) - \exp(-a_0 \theta)], \quad (5.3b)$$

TABLE 5.2 Parameters of the cascade model (5.4) fitted to the data of figure 5.6.

Symbol	c wppm	a_0 1/lap	a_1 1/lap	A_0 1/wppm	A_1 1/wppm
◇	25	1/4	1/60	21.0	5.7
○	50	1/4	1/60	22.0	6.0
□	100	1/4	1/60	32.0	8.7

where a_0 and a_1 are decay rates. The Lumley scale, or the Weissenberg number, of figure 5.6 can then be approximated by the function

$$g(\theta) = A_0 c_0(\theta) + A_1 c_1(\theta), \quad (5.4)$$

where A_0 and A_1 quantify the influence of the molecular weights on $g(\theta)$. Furthermore, considering the ideas that higher molecular weights contribute more to the fluid elasticity and that shorter polymer molecules are less likely to break under high shear, it seems reasonable to assume that $A_1 \leq A_0$, as well as $a_1 \leq a_0$. The manually fitted curves are indicated by solid lines in figure 5.6 and the corresponding values for the model parameters are given in table 5.2.

The cascade model describes the increase of the Lumley scale fairly well with the same decay rates a_0 and a_1 for all three solutions. For the model fit of the Weissenberg number the proportionality $Wi \propto \ell_p^{2/3}$ from equations (5.7) and (5.8) was used.

5.4 TURBULENCE SPECTRA IN POLYMER SOLUTIONS

In order to focus on the small-scale properties of the turbulence, the field of view was chosen relatively narrow which, in turn, limited the resolution of the large scales. The integral scales, for example, were not captured and nor were the viscous scales. The latter was due to the limited dynamic range of the PIV cameras. Nevertheless, the spectra covered roughly two decades of an intermediate spectrum range where the elastic effects could be observed.

5.4.1 KINETIC ENERGY AND LARGE-SCALE ISOTROPY

Turbulence intensities were calculated for each time step as averaged values over the ensemble and the field of view, which was less than five grid meshes wide. Figure 5.2 (a) shows that the presence of polymers in the fluid considerably increased the turbulence kinetic energy k ($= [u_1'^2 + 2u_2'^2]/2$) per unit C_p compared to the solvent. (The figure shows the same quantity—up to a factor two, because $k = q^2/2$ —as in figure 4.8.) This is in contrast to other turbulence studies^{4, 93}, for which it was observed that the polymers reduce the turbulence intensities. Although, Barenblatt et al.⁹ or Friehe and Schwarz⁵¹ also reported increased intensity levels in polymer solutions over those in the pure solvent. Furthermore, De Angelis et al.³⁷ ran numerical experiments on homogeneous turbulence in dilute polymer solutions and

5.4 TURBULENCE SPECTRA IN POLYMER SOLUTIONS

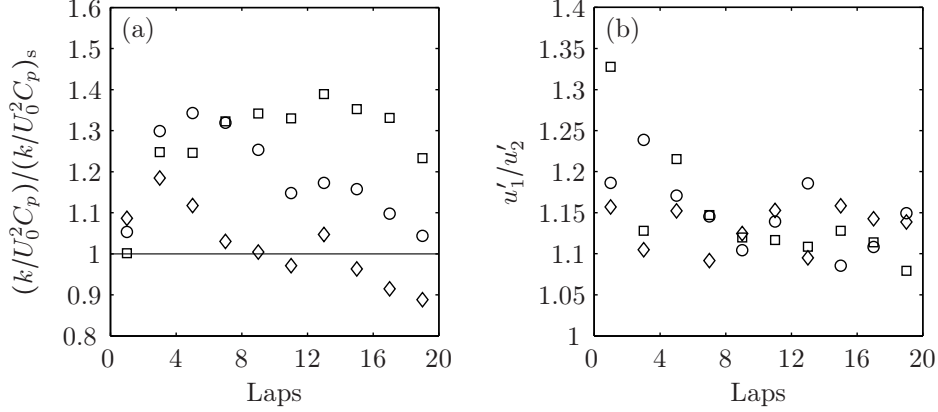


FIGURE 5.2 Evolution of (a) the turbulence kinetic energy and (b) the ratio between streamwise and transverse rms velocity. Solvent properties: $U_0 = 1.2$ m/s, $C_p = 1.04$ and $k = 46$ cm²/s². See table 5.1 for symbols and U_0 .

found that, depending on the Weissenberg number, the flow may be purely damped or may show a reduction of the small scales accompanied by increased large-scale intensities. However, the increased kinetic energy could also be attributed to a modified turbulence production at the grid, as will be shown further below.

The evolution in time of the kinetic energy for all three solutions, which is slowly decreasing after reaching a maximum, is a somewhat peculiar behavior because it does not correlate well with the integrity loss of the polymers. Moreover, it also suggests that the turbulence production at the grid varies with the properties of the solution. Shear rates in the boundary layers of the grid rods are of the order $O(10^4)$ 1/s, which is sufficiently large to stretch the polymer coils, as the inverse of the relaxation time is of the order $O(10^3)$ 1/s. Friehe and Schwarz⁵¹ described the same production phenomenon in their grid turbulence experiments in polymer solutions.

In figure 5.2 (b) are shown the ratios between the streamwise and transverse rms velocities. Besides the large scatter, the data display relatively large anisotropies for undegraded solutions, as well as a tendency towards the same value as in pure water, that is, 1.1. Increased large-scale anisotropy due to drag-reducing agents was also reported elsewhere¹⁴¹.

5.4.2 EFFECTS OF FLUID ELASTICITY ON VELOCITY SPECTRA

Velocity spectra for the streamwise and transverse components were also computed from the same velocity fields, and are shown in figure 5.3 to 5.5. Each spectrum is compared to the reference spectrum in water, and was rendered independent of the dissipation rate by using Kolmogorov variables. Strictly speaking, the dissipation rate ϵ_0 of the inertial cascade was determined by fitting $\alpha_i \epsilon_0^{2/3} \kappa_1^{-5/3}$ (indicated in

all three figures) simultaneously to ϕ_{11} and ϕ_{22} for each time interval. With these values and the solution viscosities from table 5.1, the Newtonian viscous scale η was calculated for each solution and each time interval. Generally, it differed by less than 10% from the Kolmogorov scale in the solvent.

The resulting collapse of the spectra at the low wavenumber end is fairly good, though not perfect. Convergence of the spectra was limited since there were only about ninety statistically independent spectra in a given set. To avoid cluttering the figures, not all time steps are shown. Notably, the spectra for the strongly degraded solution are omitted, except for the last.

Overall, in presence of polymers the spectra show significant effects in the small-scale region, which diminish at each time interval. In particular, the modified spectra do not show the exponential behavior in the region where the solvent spectrum has the exponential behavior associated with the dissipation range. Instead, the turbulence energy cascade appears to transition to a power-law. Solid lines proportional to κ_1^{-3} in each graph indicate this new spectral region that will be called the *elastic subrange*, which is a short form of the earlier⁴⁹ introduced name ‘elastic waves range’. Similar observations can be made in the spectra published by McComb et al.⁹³, Warholic et al.¹⁴⁸ or Berti et al.¹⁷, where the polymer spectra decay as well with a slope close to -3 , albeit the authors do not mention it explicitly. As will become clear further below, the proportionality to κ_1^{-3} is not a coincidence, and derives from the equilibrium between elastic and kinetic stresses.

However, by fitting this κ_1^{-3} curve to the longitudinal and the lateral spectrum the characteristic length scale at which the spectrum rolls off is identified as the crossover of the inertial and the elastic power-law slope (cf. dashed lines in figure 5.3 ff.). This scale is generally^{17, 37, 101} attributed the name *Lumley scale*, after Lumley^{87, 88} who first introduced the concept of a characteristic scale below which the polymers affect the turbulence. For a three-dimensional spectrum it is approximated by¹⁷

$$\ell_p \sim \sqrt{\epsilon_0 \tau_p^3}. \quad (5.5)$$

It is related to the streamwise and the transverse one-dimensional Lumley scale, via

$$\ell_p = \left(\frac{11}{27}\right)^{3/4} \ell_{p,1} = \left(\frac{11}{18}\right)^{3/4} \ell_{p,2}. \quad (5.6)$$

The prefactors account for the directional dependence of the one-dimensional spectra (i.e., $\phi_{11}(\kappa_1)$ and $\phi_{22}(\kappa_1)$), and were found with a reasoning similar to the Kolmogorov coefficients α , α_1 and α_2 . Equation (5.5) is simply a special case of the general relation $\ell \sim \sqrt{\epsilon t^3}$ for the length scale ℓ of an eddy with the time scale t in a turbulent flow with an energy flux ϵ .

Estimates of ℓ_p were gathered for all time intervals and are plotted against the number of circuits in the tunnel in figure 5.6 (a). Ideally, open and close symbols of the same shape should overlap in order to verify the relation (5.6), and the (systematic) difference is probably an artifact from the rigid fitting process of the two power-laws. Nonetheless, the data of all three tested solutions follow

5.4 TURBULENCE SPECTRA IN POLYMER SOLUTIONS

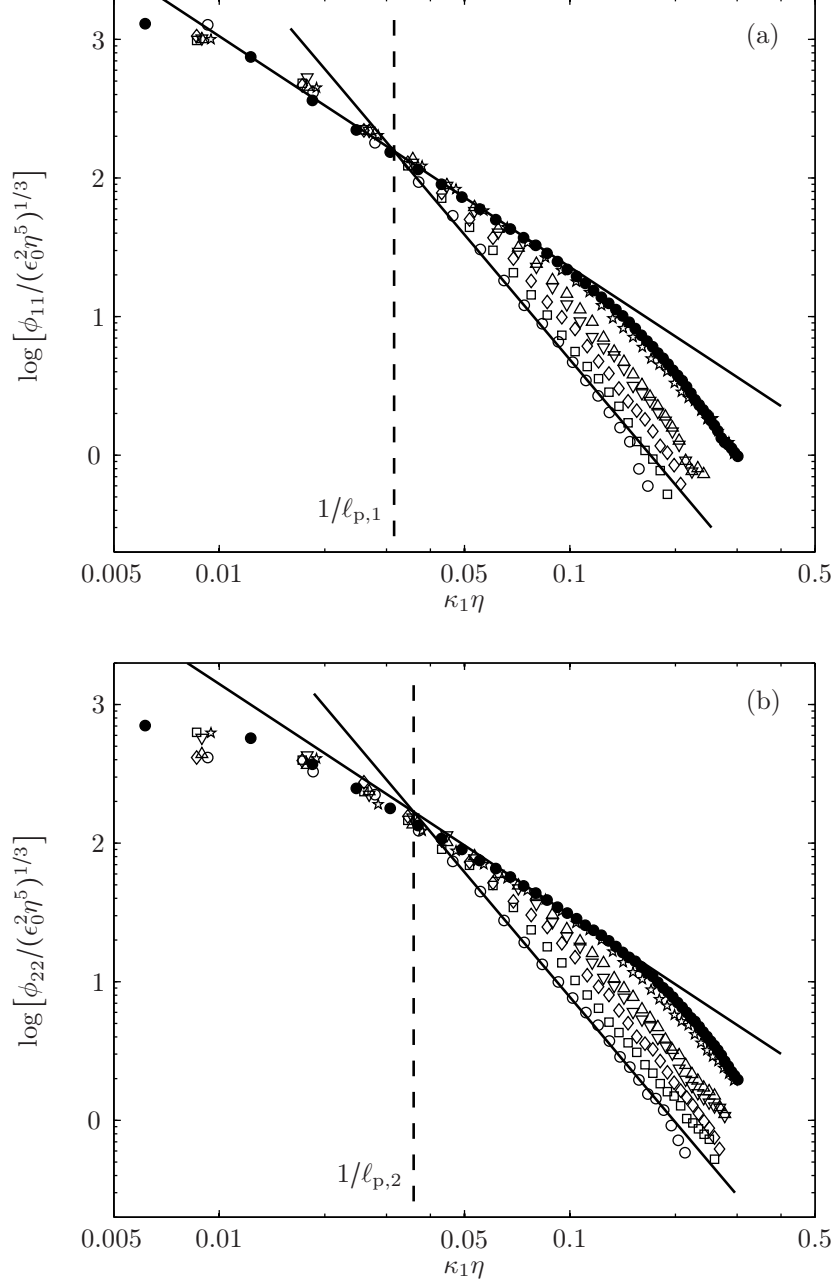


FIGURE 5.3 Rescaled (a) streamwise and (b) transverse velocity spectra in the 25 wppm PEO solution after: \circ , 1; \square , 3; \diamond , 5; ∇ , 7; \triangle , 9; and \star , 19 circuits in the tunnel. The reference spectra (\bullet) correspond to the Newtonian solvent, and the solid lines indicates the slopes of -3 and $-5/3$ fitted to the first data set. The one-dimensional Lumley scales are given by the dashed lines.

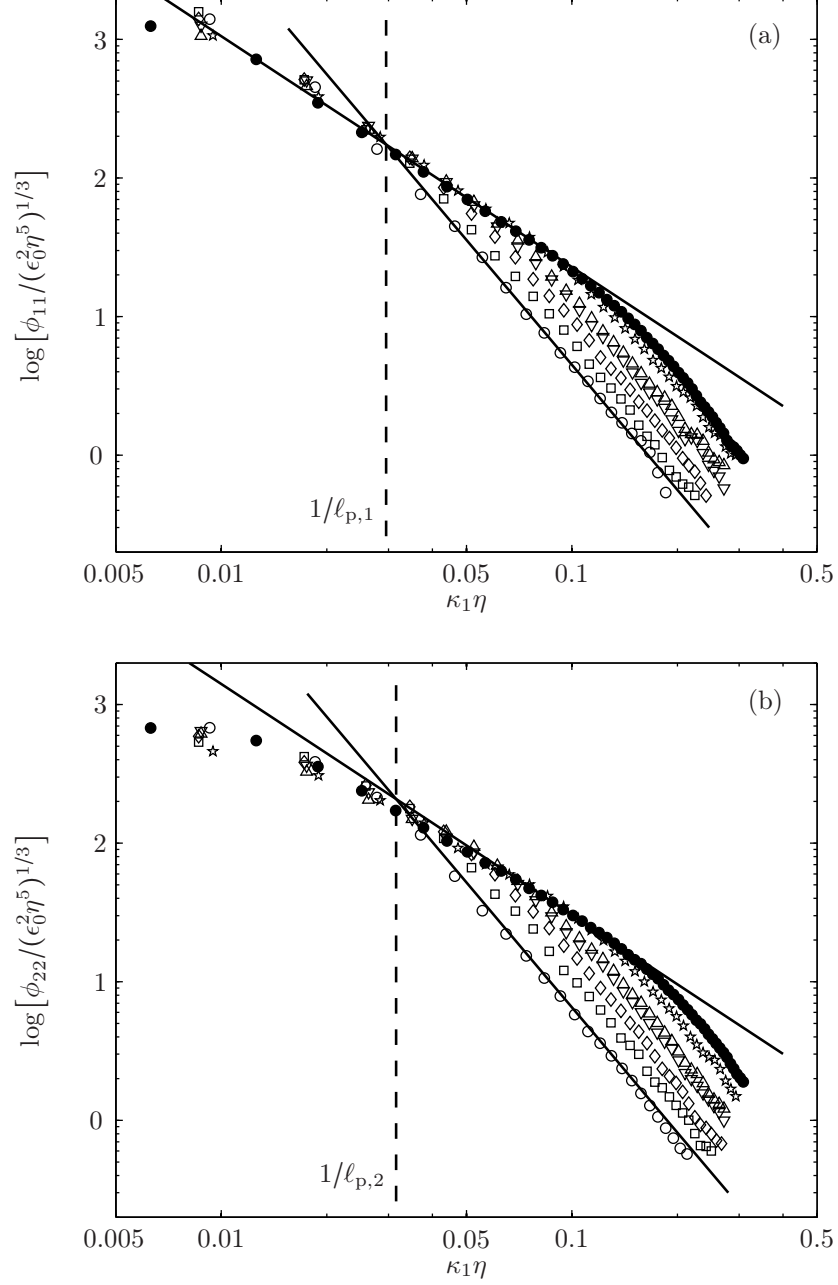


FIGURE 5.4 Rescaled (a) streamwise and (b) transverse velocity spectra in the 50 wppm PEO solution after: ○, 1; □, 3; ◇, 5; ▽, 7; △, 9; and ☆, 19 circuits in the tunnel. The reference spectra (●) correspond to the Newtonian solvent, and the solid lines indicates the slopes of -3 and $-5/3$ fitted to the first data set. The one-dimensional Lumley scales are given by the dashed lines.

5.4 TURBULENCE SPECTRA IN POLYMER SOLUTIONS

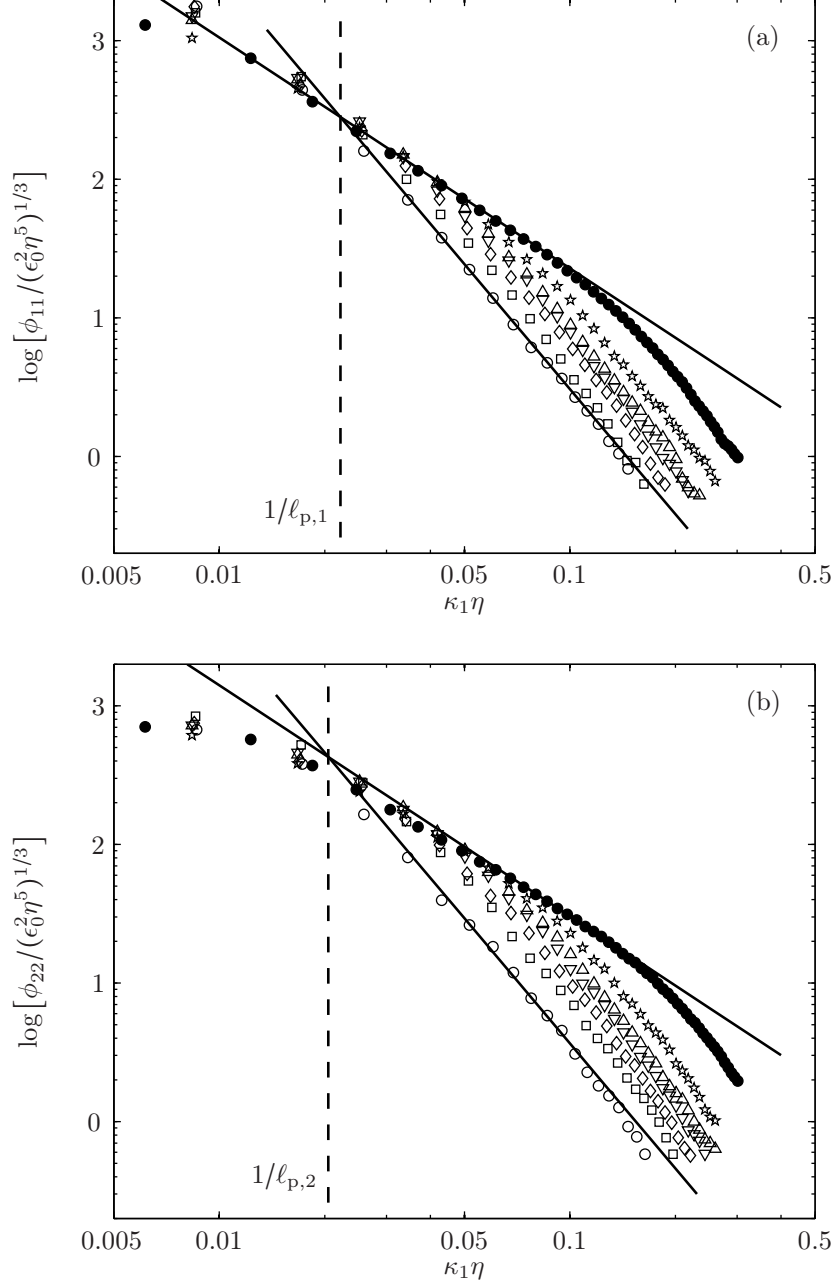


FIGURE 5.5 Rescaled (a) streamwise and (b) transverse velocity spectra in the 100 wppm PEO solution after: ○, 1; □, 3; ◇, 5; ▽, 7; △, 9; and ☆, 19 circuits in the tunnel. The reference spectra (●) correspond to the Newtonian solvent, and the solid lines indicates the slopes of -3 and $-5/3$ fitted to the first data set. The one-dimensional Lumley scales are given by the dashed lines.

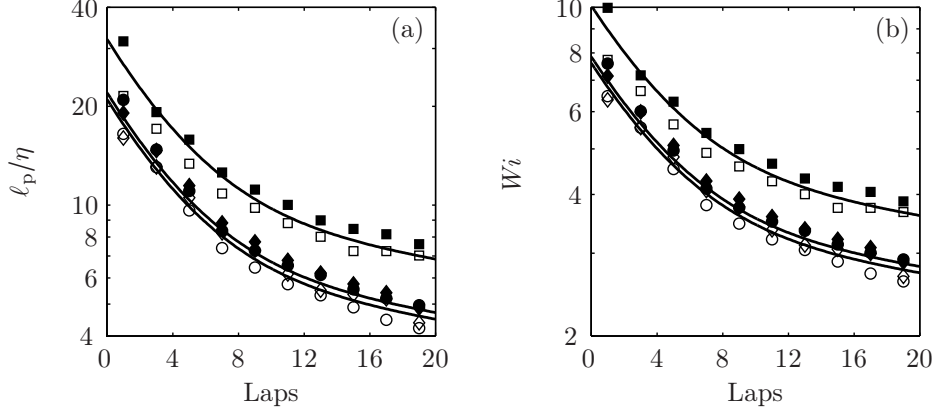


FIGURE 5.6 Evolution of (a) the Lumley scale and (b) the Weissenberg number: symbols according to table 5.1; open symbols, streamwise data (i.e., $\ell_p = (11/27)^{3/4}\ell_{p,1}$); solid symbols, transverse data (i.e., $\ell_p = (11/18)^{3/4}\ell_{p,2}$). The solid lines indicate the fitted cascade model (5.4) with the parameters as specified in table 5.2.

a similar curve with a vertical offset that depends on the polymer concentration. Hence, the magnitude of the elastic effect grows with the increasing concentration, consistently with the polymer relaxation time predicted by the Maxwell model or Rozhkov et al.'s relation (cf. section 2.4.4).

Concerning the value of τ_p obtained from these estimates, it is curious to note that it is at least one order of magnitude larger than any of the estimates of the polymer relaxation time τ as shown in figure 2.9. The reasons for this are not clear but it is noted that the ratio between ℓ_p and the fully stretched polymer length ($\approx 13.3 \mu\text{m}$) is about two orders of magnitude, that is, comparable to the ratio τ_p/τ .

The evolution of the Lumley scale in figure 5.6 (a) is an indirect measure of the evolution of the fluid elasticity. A more straightforward way to express the importance of the elastic effects is to calculate the Weissenberg number from

$$Wi = \left(\frac{\eta_p}{\eta} \right)^2, \quad (5.7)$$

where

$$\eta_p = \left(\frac{\nu \ell_p^{2/3}}{\epsilon_0^{1/3}} \right)^{1/2} \quad (5.8)$$

is the new viscous scale at the end of the elastic subrange when viscous stresses become significant. The corresponding graph is given in figure 5.6 (b), where the fitted decay model (5.4) is indicated by the solid lines (cf. table 5.2 for the parameters). These values for the Weissenberg number seem plausible, and are in contrast to the estimates based on the relaxation times reported in table 5.1 which were much smaller (viz., $Wi \lesssim 1$). This also means that the ‘effective’ relaxation time is much larger than predicted, as has been discussed in section 2.4.4.

5.4 TURBULENCE SPECTRA IN POLYMER SOLUTIONS

Between the Lumley scale ℓ_p and the viscous dissipation scale η_p energy is already dissipated before reaching the viscous subregion. This is achieved through internal friction, as well as through viscous drag, of the recoiling polymer molecules stretched by the turbulent flow.^{37, 101} The described dissipation process is sometimes^{8, 17, 49} referred to as *elastic dissipation*, which is rather a confusing term, and therefore will be called *polymer dissipation* instead. Because these dissipation mechanisms are scale-independent, a power-like spectrum can be expected.^{8, 49} Furthermore, this subrange is *self regulating*, that is to say, a temporary increase of the local shear rate entails a more vigorous polymer stretching which, in turn, produces a stronger back reaction that reduces the shear rate. The same reasoning holds vice versa. As a result, the local Weissenberg number is in the vicinity of one over the entire elastic subrange. This involves a constant local shear rate

$$s(\kappa) \sim \epsilon^{1/3}(\kappa) \kappa^{2/3} = \frac{1}{\tau}, \quad (5.9)$$

where

$$\epsilon(\kappa) = \epsilon_0 (\ell_p \kappa)^{-2} \quad (5.10)$$

is the reduced energy flux at the wavenumbers $1/\ell_p < \kappa < 1/\eta_p$ (cf. figure 5.9). Therefore, the spectrum of the elastic subrange,

$$E(\kappa) = \alpha \epsilon_0^{2/3} \ell_p^{5/3} (\ell_p \kappa)^{-3}, \quad (5.11)$$

is governed by a -3 -decay. In contrast, Fouxon and Lebedev⁴⁹ claim that in this subrange the energy has to decrease faster than -3 , in order to ensure a finite value for the integral of the derivative spectrum, that is,

$$\left\langle \left(\frac{\partial u_i}{\partial x_1} \right)^2 \right\rangle = \int_0^\infty \kappa_1^2 \phi_{ii}(\kappa_1) d\kappa_1. \quad (5.12)$$

For the -3 -decay the convergence of the integral is assured by the exponential decay in the viscous subregion, similar to a Newtonian spectrum.

The elastic cascade proceeds until the viscous stresses overcome inertial and elastic stresses and reaches η_p ($= \sqrt{\nu\tau}$), with a residual energy dissipation rate

$$\epsilon_v = \frac{\nu}{\tau^2}, \quad (5.13)$$

which can be significantly smaller than the initial ϵ_0 . Early grid turbulence experiments in polymer solutions by Friehe and Schwarz⁵¹ exhibited reduced dissipation rates in presence of polymers. van Doorn et al.¹⁴¹ have shown with a towed grid experiment that in dilute polymer solutions ϵ_v is indeed smaller than ϵ_0 , and Liberson et al.⁸³ have found evidence of energy dissipation by polymers in a ‘washing machine’-like facility[†].

[†]Turbulence is generated by sets of rotating disks at two opposing walls of a small tank.

However, considering the reduction of the energy flux specified by relation (5.10), the viscous dissipation ϵ_v can become vanishingly small in favor of the polymer dissipation, denoted ϵ_p . Hence, ℓ_p can be associated to a new dissipation scale which replaces the Kolmogorov scale.⁴⁹

A summary, as well as additional information about the employed model spectrum can be found in the last section of this chapter.

5.4.3 VISCOUS AND POLYMER DISSIPATION RATE

Taking into account the polymer dissipation, the total energy budget for turbulence without production in an elastic fluid reads⁸⁹

$$\frac{d}{dt}(k + e_p) = -\epsilon_0 = -\epsilon_v - \epsilon_p, \quad (5.14)$$

where k is the turbulence kinetic energy and e_p is the potential elastic energy of the polymers. The total energy is dissipated at rates of ϵ_v and ϵ_p .

Recall that $\epsilon_v \equiv 2\nu \langle s_{ij}s_{ij} \rangle$, which was measured with PIV. Estimates of the turbulence dissipation rate ϵ_v were again obtained using equation (4.13), followed by averaging over each time step and the field of view. Figure 5.7 (a) shows the viscous dissipation rates relative to the total dissipation rates (determined from the spectrum fits explained in the previous subsection) as a function of passes through the test section. The presence of polymers lowered the viscous dissipation rate by remarkable 40 to 70 % in the three tested solutions. These values agree well with the findings by Virk et al.¹⁴⁶ who measured a reduction of 40 % in a turbulent pipe flow. Due to polymer degradation, the fraction of energy dissipated by viscosity gradually increases until the polymer coils are too small to contribute to the dissipation, which is also reflected in the velocity spectra presented above. Furthermore, the higher concentrated solution exhibit elastic effects during a longer period, which seems reasonable as there are more polymer molecules.

Figure 5.7 (b) shows the same data as a function of the Weissenberg number found via the Lumley scale. All three sets are consistent with the idea that a stronger elasticity leads to larger dissipative effects.

Berti et al.¹⁷ highlights two different scenarios of viscoelastic effects on the turbulence spectrum: the first one is essentially the model already described, where the viscous dissipation may be negligible and the scale ℓ_p becomes the new dissipation scale.

The second scenario limits the energy dissipation by polymer relaxation to a fixed fraction of the total dissipation, so that there is always viscous dissipation present.¹⁵ In this alternative, the inertial cascade continues with a reduced energy flux after a relatively brief intermediate elastic subrange. The maximum fraction of energy dissipated in this subrange is supposedly limited and becomes independent of the Weissenberg number.¹⁷ Although, the present data in figure 5.7 (b) is limited to low Wi , it does not support the model initially suggested by Benzi et al.¹⁵.

The experimental conditions for all three solutions were comparable, but the resulting turbulence, namely ϵ_0 and k , varied with the solution concentration and

5.4 TURBULENCE SPECTRA IN POLYMER SOLUTIONS

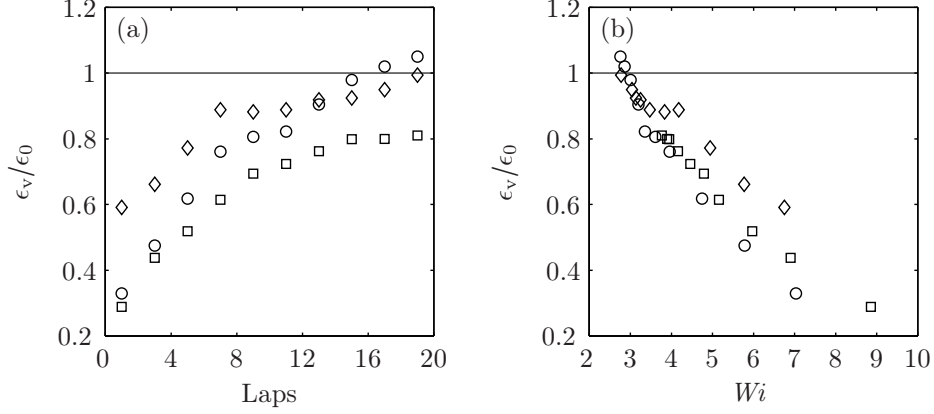


FIGURE 5.7 Ratio between viscous and total dissipation rate: (a) evolution in time; (b) dependence on Wi . The dissipation rate ϵ_0 was estimated from the spectra. See table 5.1 for symbols.

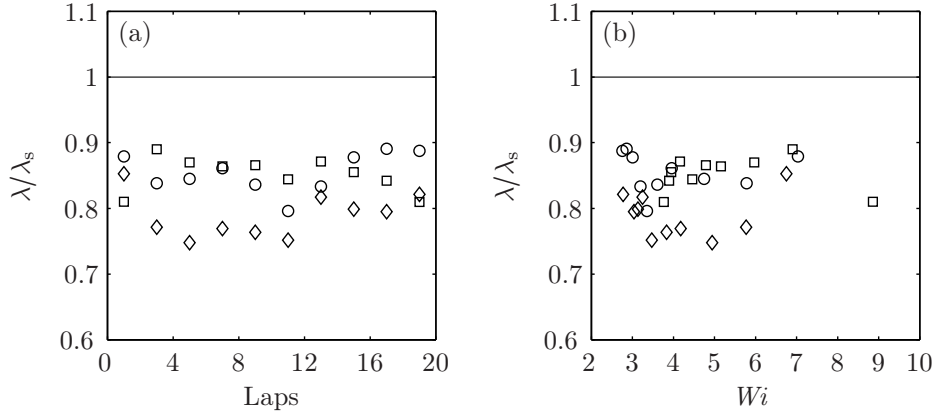


FIGURE 5.8 Evolution of the Taylor microscale with respect to $\lambda_s = 1.7$ mm: (a) evolution in time; (b) dependence on Wi . See table 5.1 for symbols.

the degree of polymer degradation. A popular quantity to compare different turbulent flows is the Taylor microscale λ ($= \sqrt{10\nu k/\epsilon_0}$) shown for all solutions in figure 5.8.

Although fairly lower than the value for pure water, the Taylor scales are very little affected by the changing fluid elasticity, which is in accord to other laboratory findings⁸². This conclusion is also supported by plotting the data against the Weissenberg number (cf. figure 5.8 (b)). The systematic offset suggests that the turbulence generation was not identical in the polymer solutions and the pure solvent after all, or it could be an artifact of the data processing. A 10 to 20% error seems reasonable regarding the fitting procedures on data with a relatively

narrow spectral band.

It has to be noted that the Taylor scale was calculated with the total dissipation rate ϵ_0 , and that the use of the viscous dissipation rate ϵ_v instead would mainly reflect the evolution of the latter.

5.5 SUMMARY AND CONCLUDING REMARKS

5.5.1 THE MODEL SPECTRUM

The model spectrum established in the preceding sections was adapted from Fouxon and Lebedev⁴⁹. It consists of three major regions (cf. figure 5.9): (I) a Newtonian inertial cascade at low wavenumbers; (V) a Newtonian viscous dissipation subrange at the high wavenumber end; (E) an elastic subrange between the inertial and the viscous region, that is governed by a strong back reaction of the polymers on the flow. In the following the main properties of each subrange are summarized.

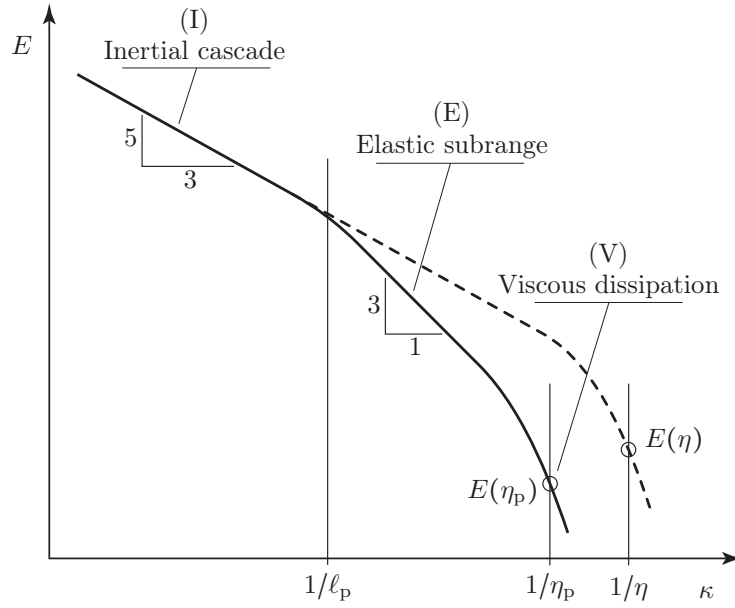


FIGURE 5.9 Model spectrum for turbulence in polymer solutions indicating the three regions: (I) $\kappa < 1/\ell_p$, Kolmogorov's inertial cascade; (E) $1/\ell_p < \kappa < 1/\eta_p$, fractions of turbulence kinetic energy is transferred to elastic energy, which is then dissipated by viscous drag of relaxing polymers and internal friction between the monomers of a single polymer; (V) $\kappa \gtrsim 1/\eta_p$, turbulence kinetic energy is dissipated by viscous forces, identical to the Newtonian spectrum (broken line).

Inertial subrange (I) It is determined by an energy cascade with a constant energy flux ϵ_0 and the constant scaling

$$E(\kappa) = \alpha \epsilon_0^{2/3} \kappa^{-5/3}, \quad (5.15)$$

5.5 SUMMARY AND CONCLUDING REMARKS

also known as the Kolmogorov spectrum. Consequently, the local shear rate $s(\kappa)$, approximated by

$$s(\kappa) \sim \frac{u(\kappa)}{\ell} \sim \epsilon_0^{1/3} \kappa^{2/3}, \quad (5.16)$$

is growing for increasing wavenumbers, but is too weak to excite the elastic degrees of freedom. The quantities u and ℓ are the characteristic velocity fluctuation and length of a turbulence scale at a given wavenumber $\kappa \sim 1/\ell$, respectively. Similarly, the local Reynolds and Weissenberg numbers can be expressed as

$$Re(\kappa) = \frac{u(\kappa)\ell}{\nu} \sim \frac{\epsilon_0^{1/3}}{\nu\kappa^{4/3}}, \quad (5.17)$$

$$Wi(\kappa) = s(\kappa)\tau \sim \epsilon_0^{1/3} \tau \kappa^{2/3}. \quad (5.18)$$

Elastic subrange (E) This new spectral region is separated from the inertial cascade by the Lumley scale ℓ_p ($\sim \sqrt{\epsilon_0 \tau^3}$) determined by the elastic properties of the fluid and the turbulence dissipation rate. In this subrange fractions of the turbulence kinetic energy arriving from the inertial subrange is converted into elastic energy by extending the polymer coils. Subsequent relaxation of the stretched coils dissipates a part of this elastic energy due to the viscous drag of the polymer molecules in the solvent, as well as interactions between monomers of a single polymer.¹⁰¹ The residual part of the elastic energy is transformed back to turbulence kinetic energy. This *back reaction*⁸ is the main feature of this subrange. As a result, the energy flux from higher to lower wavenumbers is continuously reduced.

Furthermore, this region appears to follow a power-law (cf., e.g., refs. 49 and 148, as well as figures 5.3 to 5.5) with a slope of -3 (cf. present study), which suggests that it is *self regulating*, in the sense that elastic and kinetic forces are in equilibrium. This requires that the polymer stresses overcome the viscous stresses, that is,

$$Wi(\kappa) = O(1) \quad (5.19)$$

for $1/\ell_p < \kappa < 1/\eta_p$. This implicates that the shear rate s is constant and comparable to $1/\tau_p$ which, in turn, requires the verification of relation (5.10), that is,

$$\epsilon(\kappa) = \epsilon_0 (\ell_p \kappa)^{-2}.$$

The local dissipation rate is bound by $\epsilon_v \leq \epsilon(\kappa) \leq \epsilon_0$. Hence, the energy contained in a turbulent structure of wavenumber κ decreases according to equation (5.11), namely

$$E(\kappa) = \alpha \epsilon_0^{2/3} \ell_p^{5/3} (\ell_p \kappa)^{-3},$$

and the local Reynolds number is, thus, given by

$$Re(\kappa) \sim \frac{\epsilon_0^{1/3} \ell_p^{4/3}}{\nu (\ell_p \kappa)^2}. \quad (5.20)$$

Viscous subrange (V) This region is dominated by viscous stresses which transform turbulence kinetic energy into heat, identical to the dissipation range in the Newtonian spectrum. Therefore,

$$Re(\kappa) \lesssim 1, \quad (5.21)$$

$$Wi(\kappa) \lesssim 1, \quad (5.22)$$

and the new viscous dissipation scale is given by

$$\eta_p = \left(\frac{\nu^3}{\epsilon_v} \right)^{1/4} \sim \sqrt{\nu \tau}, \quad (5.23)$$

where τ determines the characteristic time scale of the smallest turbulence structures. The latter is a direct consequence of the self regulation which, moreover, uniquely determines the reduced energy flux

$$\epsilon_v \sim \frac{\nu}{\tau^2} \quad (5.24)$$

contributing to the viscous dissipation at the end of the elastic subrange.

The dissipation scales η_p and η and their respective energies are related by

$$\eta_p \sim \eta Re_p^{1/4}, \quad (5.25)$$

$$E(\eta_p) \sim E(\eta) Re_p^{-1/4}, \quad (5.26)$$

where

$$Re_p = \frac{(\ell_p^4 \epsilon_0)^{1/3}}{\nu} = \frac{\epsilon_0}{\epsilon_v} \quad (5.27)$$

is the local Reynolds number at the Lumley scale.

The Reynolds number Re_{cs} defined by (5.1) specifies the necessary flow conditions such that the Lumley scale becomes comparable to the Newtonian Kolmogorov scale from below (ℓ_p grows with increasing Re), and hence, polymers are no longer passive in the turbulence. Equation (5.27), on the other hand, defines a local Reynolds number that is equal to one below the coil-stretch transition, that is, when $Re_M \lesssim Re_{cs}$.

5.5 SUMMARY AND CONCLUDING REMARKS

5.5.2 GENERAL REMARKS

In chapter 2 it was shown that shear-thinning for the investigated concentrations is virtually absent, and thus, the encountered non-Newtonian effects can be attributed to fluid elasticity.

Furthermore, the results obtained from high resolution PIV measurements are of excellent quality, mainly because of the recently developed correction procedures⁸¹ which have been adapted for the present measurement configuration.

The obtained results confirm the previously reported findings (cf. refs. 10, 53, 93, 141, 146, 148) that these effects are local, that is, they modify the small-scale structure of the turbulence, whereas the large scales remain essentially unaffected.

Moreover, the turbulence kinetic energy and the large-scale anisotropy were observed to increase in all polymer solutions, which is likely to be caused by a modified turbulence production at the grid.

Since the degradation of the polymer solutions modified both turbulence decay and turbulence production, the comparison of the total dissipation rates or the Taylor microscales between polymer solutions and the pure solvent is difficult. Therefore, future experiments should include a fluid independent turbulence production or a means to accurately determine the total dissipation rate.

However, the polymer degradation is not an inconvenience per se. The difficulties are in the determination of the important fluid properties, such as the relaxation time, and the varying turbulence production. Apart from that, the degrading polymers actually allow to cover a wide range of Weissenberg numbers in one experiment.

Finally, a new cascade model was successfully introduced to describe the evolution of fluid or flow quantities under polymer degradation, which was necessary as the existing attempts in the literature were unsatisfactory.

CHAPTER 6

Final remarks and outlook

6.1 SUMMARY OF THE MOST IMPORTANT FINDINGS

Grid turbulence was studied in water and in low concentration PEO solutions, where turbulence was generated with a novel grid type which consists of a square mesh grid with tethered spheres attached to each grid node. Three different tethered bead diameters were tested in pure water and the largest diameter ($D/M = 3/4$) produced the most significant changes in turbulence properties over the plain grid. The influence of the density ratio between the sphere and water was also investigated for the smallest bead diameter, and was found to be negligible at the flow rate studied.

This new grid allowed to increase the turbulence Reynolds number Re_λ in water by a factor of roughly two, resulting in a small but noticeable constant scaling range in the velocity spectrum. This change can be attributed to the increase in turbulence intensity, meanwhile the Taylor microscale remained unaffected compared to the RTG. It was observed that the new grid produces higher turbulence intensities per unit C_p than the classical plain grid. Hence, the new grid transforms potential energy more effectively into turbulence energy. Moreover, the new grid improves the large-scale isotropy by reducing the deficit between the streamwise and the transverse intensities.

Velocity spectra and energy dissipation rates of energy have been measured with PIV in dilute PEO solutions with concentrations below 100 wppm. Severe polymer decay in the flow facility allowed for a study of these quantities under decreasing elastic effects. The results show that dissipation rates and kinetic energies varied considerably with the investigated concentration and the degree of degradation. This is presumably due to a modified turbulence production at the grid. They also indicate that the anisotropy between streamwise and transverse intensities is stronger in polymer solutions than in the Newtonian solvent.

Furthermore, the measurements evidence the existence of a characteristic length scale ℓ_p where the polymers start to affect the energy cascade. It was observed that above this scale the velocity spectra are virtually unchanged relative to the Newtonian case. Below ℓ_p , however, the energy transfer from large to small scales is reduced proportional to κ^{-2} , and consequently, the energy spectrum scales with κ^{-3} instead of $\kappa^{-5/3}$ and becomes self-regulating. The residual energy is most likely

dissipated due to viscous drag of relaxing polymer chains and by internal friction in the polymer coils. Hence, ℓ_p acts like a new dissipation scale. With diminishing fluid elasticity, this scale is shifted towards higher wavenumbers, but the -3 -power-law is maintained. Therefore, the scale ℓ_p depends on the elastic properties of the fluid.

6.2 PERSPECTIVES

Some theoretical and numerical predictions have been confirmed with the present study but the results also raise new questions, such as the physical interpretation of the time scale τ_p extracted from ℓ_p . This time scale was found to be much larger than any relaxation time estimate, and is worthy of future detailed investigation. Moreover, an accurate measure of the polymer relaxation time of dilute solutions would allow to verify if indeed it coincides with the time scale τ_p of the observed switchover from the $-5/3$ - to the -3 -scaling region.

A major flaw of the present experiment is the turbulence production that varies with the working fluid, and affects kinetic energy and dissipation rate. To overcome this difficulty, it would be necessary to build an experiment where the production is indifferent to the studied fluid, or to develop a method to accurately determine the total energy flux.

References

1. J. B. Abbiss, T. W. Chubb, and E. R. Pike. Laser Doppler anemometry. *Opt. Laser Technol.*, pages 249–261, 1974. 41
2. R. J. Adrian and C. S. Yao. Power spectra of fluid velocities measured by laser Doppler velocimetry. *Exp. Fluids*, 5:17–28, 1987. 43, 44
3. H.-E. Albrecht, M. Borys, N. Damaschke, and C. Tropea. *Laser Doppler and phase Doppler measurement techniques*. Springer, 2003. 41
4. Y. Amarouchene and H. Kellay. Polymers in 2d turbulence: suppression of large scale fluctuations. *Phys. Rev. Lett.*, 89(10):104502, 2002. 82
5. R. Antonia, P. Lavoie, L. Djenidi, and A. Benaissa. Effect of a small axisymmetric contraction on grid turbulence. *Exp. Fluids*, 2009. 27
6. R. A. Antonia, R. J. Smalley, T. Zhou, F. Anselmet, and L. Danaila. Similarity of energy structure functions in decaying homogeneous isotropic turbulence. *J. Fluid Mech.*, 487(-1):245–269, 2003. 55, 72, 74
7. S. Baldi and M. Yianneskis. On the quantification of energy dissipation in the impeller stream of a stirred vessel from fluctuating velocity gradient measurements. *Chem. Eng. Sci.*, 59(13):2659–2671, 2004. 35
8. E. Balkovsky, A. Fouxon, and V. Lebedev. Turbulence of polymer solutions. *Phys. Rev. E*, 64:056301, 2001. 2, 78, 89, 93
9. G. Barenblatt, V. Kalashnikov, and A. Kudin. Hot-wire anemometer study of the structure of polymer solutions. *J. Appl. Mech. Tech. Phy.*, 9(5):610–612, 1968. 31, 82
10. B. J. S. Barnard and R. H. J. Sellin. Grid turbulence in dilute polymer solutions. *Nature*, 222(5199):1160–1162, 1969. 1, 13, 95
11. H. A. Barnes, J. F. Hutton, and K. Walters. *An introduction to rheology*. Elsevier, 1998. 20, 30
12. G. K. Batchelor. *The theory of homogeneous turbulence*. Cambridge University Press, 1953. Reprinted 1970. 1, 2, 3, 27, 45, 48
13. G. K. Batchelor and A. A. Townsend. Decay of isotropic turbulence in the initial period. *P. Roy. Soc. Lond. A Mat.*, 193(1035):539–558, 1948. 2, 51, 57
14. L. H. Benedict, H. Nobach, and C. Tropea. Estimation of turbulent velocity spectra from laser Doppler data. *Meas. Sci. Technol.*, 11:1089–1104, 2000. 42
15. R. Benzi, E. De Angelis, R. Govindarajan, and I. Procaccia. Shell model for drag reduction with polymer additives in homogeneous turbulence. *Phys. Rev. E*, 68(1):016308, 2003. 2, 90
16. N. S. Berman. Drag reduction by polymers. *Annu. Rev. Fluid Mech.*, 10:47–64, 1978. 13

REFERENCES

17. S. Berti, A. Bistagnino, G. Boffetta, A. Celani, and S. Musacchio. Small-scale statistics of viscoelastic turbulence. *Europhys. Lett.*, 76(1):63–69, 2006. 1, 2, 47, 78, 84, 89, 90
18. R. B. Bird, R. C. Armstrong, and O. Hassager. *Dynamics of polymeric liquids*, volume 1: Fluid mechanics. Wiley Interscience, second edition, 1987. 7, 8, 9, 10, 11, 12, 16, 19, 20, 30
19. R. B. Bird, C. F. Curtiss, R. C. Armstrong, and O. Hassager. *Dynamics of polymeric liquids*, volume 2: Kinetic theory. Wiley Interscience, second edition, 1987. 10
20. V. C. Bizotto and E. Sabadini. Poly(ethylene oxide) \times polyacrylamide. Which one is more efficient to promote drag reduction in aqueous solution and less degradable? *J. Appl. Polym. Sci.*, 110(3):1844–1850, 2008. 23, 81
21. D. V. Boger. A highly elastic constant-viscosity fluid. *J. Non-Newton. Fluid*, 3:87–91, 1977/78. 8
22. C. Brennen and G. E. Gadd. Aging and degradation in dilute polymer solutions. *Nature*, 215(5108):1368–1370, 1967. 23
23. D. Britz and R. A. Antonia. A comparison of methods of computing power spectra of LDA signals. *Meas. Sci. Technol.*, 7(7):1042–1053, 1996. 42
24. W. Brostow. Drag reduction and mechanical degradation in polymer-solutions in flow. *Polymer*, 24(5):631–638, 1983. 81
25. W. Brostow. Drag reduction in flow: review of applications, mechanism and prediction. *J. Ind. Eng. Chem.*, 14(4):409–416, 2008. 1
26. H. H. Bruun. *Hot-Wire Anemometry*. Oxford University Press, 1995. 31
27. H. H. Bruun. Hot-film anemometry in liquid flows. *Meas. Sci. Technol.*, 7(10):1301–1312, 1996. 31
28. P. Buchave, W. K. J. George, and J. L. Lumley. The measurement of turbulence with the laser-Doppler anemometer. *Annu. Rev. Fluid Mech.*, 11:443–503, 1979. 41, 42
29. P. Burattini, P. Lavoie, and R. Antonia. Velocity derivative skewness in isotropic turbulence and its measurement with hot wires. *Exp. Fluids*, 45(3):523–535, 2008. 35
30. T. Burghelea, E. Segre, and V. Steinberg. Elastic turbulence in von Kármán swirling flow between two disks. *Phys. Fluids*, 19(5):053104, 2007. 7
31. F. H. Champagne. Fine-scale structure of turbulent velocity-field. *J. Fluid Mech.*, 86(MAY):67–108, 1978. 35
32. S. U. Choi, Y. I. Cho, and K. E. Kasza. Degradation effects of dilute polymer solutions on turbulent friction and heat transfer behavior. *J. Non-Newton. Fluid*, 41:289–307, 1992. 23, 81
33. G. Comte-Bellot and S. Corrsin. The use of a contraction to improve the isotropy of grid-generated turbulence. *J. Fluid Mech.*, 25:657–682, 1966. 2, 27, 55
34. J. J. Cooper-White, J. E. Fagan, V. Tirtaatmadja, D. R. Lester, and D. V. Boger. Drop formation dynamics of constant low-viscosity, elastic fluids. *J. Non-Newton. Fluid*, 106(1):29–59, 2002. 7
35. A. Corana, M. Marchesi, C. Martini, and S. Ridella. Minimizing multimodal functions of continuous variables with the “simulated annealing” algorithm. *ACM Trans. Math. Softw.*, 13(3):262–280, 1987. 11
36. M. E. Cowan, R. D. Hester, and C. L. McCormick. Water-soluble polymers; LXXXII.

REFERENCES

- Shear degradation effects on drag reduction behavior of dilute polymer solutions. *J. Appl. Polym. Sci.*, 82(5):1211–1221, 2001. 15, 23
37. E. De Angelis, C. M. Casciola, R. Benzi, and R. Piva. Homogeneous isotropic turbulence in dilute polymers. *J. Fluid Mech.*, 531:1–10, 2005. 82, 84, 89
38. J. de Jong, L. Cao, S. Woodward, J. Salazar, L. Collins, and H. Meng. Dissipation rate estimation from PIV in zero-mean isotropic turbulence. *Exp. Fluids*, 46(3): 499–515, 2009. 35, 47
39. S. de Waele and P. M. T. Broersen. Reliable LDA-spectra by resampling and ARMA-modeling. *IEEE T. Instrum. Meas.*, 48(6):1117–1121, 1999. 42
40. J. M. J. Den Toonder, A. A. Draad, G. D. C. Kuiken, and F. T. M. Nieuwstadt. Degradation effects of dilute polymer-solutions on turbulent drag reduction in pipe flows. *Appl. Sci. Res.*, 55(1):63–82, 1995. 13, 23, 25
41. J. M. J. Den Toonder, M. A. Hulsen, G. D. C. Kuiken, and F. T. M. Nieuwstadt. Drag reduction by polymer additives in a turbulent pipe flow: numerical and laboratory experiments. *J. Fluid Mech.*, 337:193–231, 1997. 1
42. S. S. Deshpande, M. J. Sathe, and J. B. Joshi. Evaluation of local turbulent energy dissipation rate using piv in jet loop reactor. *Ind. Eng. Chem. Res.*, 48(10):5046–5057, 2009. 35
43. F. Durst, A. Melling, and J. H. Whitelaw. *Principles and practice of laser-Doppler anemometry*. Academic Press, 1976. 41, 42
44. K. W. Ebagninin, A. Benchabane, and K. Bekkour. Rheological characterization of poly(ethylene oxide) solutions of different molecular weights. *J. Colloid. Interf. Sci.*, 336(1):360–367, 2009. 7
45. S. Elghobashi. On predicting particle-laden turbulent flows. *Appl. Sci. Res.*, 52(4): 309–329, 1994. 36
46. M. P. Escudier, F. Presti, and S. Smith. Drag reduction in the turbulent pipe flow of polymers. *J. Non-Newton. Fluid*, 81(3):197–213, 1999. 1
47. J. D. Ferry. *Viscoelastic Properties of Polymers*. Wiley, third edition, 1980. 1, 9, 12
48. J. Foucaut, J. Carlier, and M. Stanislas. PIV optimization for the study of turbulent flow using spectral analysis. *Meas. Sci. Technol.*, 15:1046–1058, 2004. 40, 41
49. A. Fouxon and V. Lebedev. Spectra of turbulence in dilute polymer solutions. *Phys. Fluids*, 15(7):2060–2072, 2003. 2, 77, 84, 89, 90, 92, 93
50. F. N. Frenkiel, P. S. Klebanoff, and T. T. Huang. Grid turbulence in air and water. *Phys. Fluids*, 22(9):1606–1617, 1979. 2
51. C. Friehe and W. Schwarz. Grid-generated turbulence in dilute polymer solutions. *J. Fluid Mech.*, 44:173–193, 1970. 1, 2, 31, 51, 80, 82, 83, 89
52. M. Gad-el-Hak and S. Corrsin. Measurements of the nearly isotropic turbulence behind a uniform jet grid. *J. Fluid Mech.*, 62(01):115–143, 1974. 3, 51, 58
53. G. E. Gadd. Turbulence damping and drag reduction produced by additives in water. *Nature*, 206(4983):463–467, 1965. 1, 13, 95
54. W. K. George. The decay of homogeneous isotropic turbulence. *Phys. Fluids. A Fluid*, 4(7):1492–1509, 1992. 35
55. M. T. Ghannam. Rheological properties of aqueous polyacrylamide/NaCl solutions. *J. Non-Newton. Fluid*, 72:1905–1912, 1999. 14
56. W. L. Goffe, G. D. Ferrier, and J. Rogers. Global optimization of statistical functions with simulated annealing. *J. Econometrics*, 60(1-2):65–99, 1994. 11

REFERENCES

57. R. N. Govardhan and C. H. K. Williamson. Vortex-induced vibrations of a sphere. *J. Fluid Mech.*, 531:11–47, 2005. 3, 30, 75
58. W. W. Graessley. Polymer-chain dimensions and the dependence of viscoelastic properties on concentration, molecular-weight and solvent power. *Polymer*, 21(3): 258–262, 1980. 1, 8, 9
59. A. Groisman and V. Steinberg. Elastic turbulence in a polymer solution flow. *Nature*, 405(6782):53–55, 2000. 1, 7
60. A. Groisman and V. Steinberg. Elastic turbulence in curvilinear flows of polymer solutions. *New J. Phys.*, 6:29, 2004. 1, 7
61. S. Hanson. Broadening of the measured frequency spectrum in a differential laser anemometer due to interference plane gradients. *J. Phys. D Appl. Phys.*, 6:164–171, 1973. 42
62. S. Herpin, C. Wong, M. Stanislas, and J. Soria. Stereoscopic PIV measurements of a turbulent boundary layer with a large spatial dynamic range. *Exp. Fluids*, 45(4): 745–763, 2008. 35
63. E. Hinch and C. Elata. Heterogeneity of dilute polymer solutions. *J. Non-Newton. Fluid*, 5:411–425, 1979. 10, 16
64. J. O. Hinze. *Turbulence*. McGraw-Hill, second edition, 1975. 3, 4, 32, 45, 61
65. A. F. Horn and E. W. Merrill. Midpoint scission of macromolecules in dilute solution in turbulent flows. *Nature*, 312(8):140–141, 1984. 7, 79
66. D. Hurst and J. C. Vassilicos. Scalings and decay of fractal-generated turbulence. *Phys. Fluids*, 19(3):035103, 2007. 3, 75
67. E. A. Jensen. Determination of discrete relaxation spectra using simulated annealing. *J. Non-Newton. Fluid*, 107(1-3):1–11, 2002. 11
68. J. Jimenez, R. Martinez-Val, and M. Rebollo. Hot-film sensors calibration drift in water. *J. Phys. E Sci. Instrum.*, 14(5):569–572, 1981. 32
69. V. Kalashnikov. Degradation accompanying turbulent drag reduction by polymer additives. *J. Non-Newton. Fluid*, 103:105–121, 2002. 10
70. V. N. Kalashnikov. Shear-rate dependent viscosity of dilute polymer-solutions. *J. Rheol.*, 38(5):1385–1403, 1994. 10, 13
71. V. N. Kalashnikov and S. A. Vlasov. Scale-dependent effect in laminar-flow of dilute polymer-solution in tubes. *Rheol. Acta*, 17(3):296–302, 1978. 15
72. H. S. Kang, S. Chester, and C. Meneveau. Decaying turbulence in an active-grid-generated flow and comparisons with large-eddy simulations. *J. Fluid Mech.*, 480: 129–160, 2003. 3
73. J. Kilander and A. Rasmuson. Energy dissipation and macro instabilities in a stirred square tank investigated using an LE PIV approach and LDA measurements. *Chem. Eng. Sci.*, 60(24):6844–6856, 2005. 35
74. C. A. Kim, J. T. Kim, K. Lee, H. J. Choi, and M. S. Jhon. Mechanical degradation of dilute polymer solutions under turbulent flow. *Polymer*, 41(21):7611–7615, 2000. 23
75. J. Kim and R. A. Antonia. Isotropy of the small scales of turbulence at low Reynolds number. *J. Fluid Mech.*, 251(-1):219–238, 1993. 35
76. K. Kim and A. I. Sirviente. Wall versus centerline polymer injection in turbulent channel flows. *Flow Turbul. Combust.*, 78(1):69–89, 2007. 1
77. A. Kistler and T. Vrebalovich. Grid turbulence at large Reynolds numbers. *J. Fluid*

REFERENCES

- Mech.*, 26:37–47, 1966. 2
78. T. Kurian and J. H. M. Fransson. Grid-generated turbulence revisited. *Fluid Dyn. Res.*, 41(2):021403, 2009. 35, 72
 79. J. V. Larssen. *Large scale homogeneous turbulence and interactions with a flat-plate cascade*. PhD thesis, Virginia Polytechnic Institute and State University, 2005. 3
 80. P. Lavoie, P. Burattini, L. Djenidi, and R. A. Antonia. Effect of initial conditions on decaying grid turbulence at low r_λ . *Exp. Fluids*, 39(5):865–874, 2005. 55
 81. P. Lavoie, G. Avallone, F. De Gregorio, G. P. Romano, and R. A. Antonia. Spatial resolution of PIV for the measurement of turbulence. *Exp. Fluids*, 43(1):39–51, 2007. 39, 46, 47, 95
 82. A. Liberzon, M. Guala, B. Luthi, W. Kinzelbach, and A. Tsinober. Turbulence in dilute polymer solutions. *Phys. Fluids*, 17(3):031707, 2005. 13, 91
 83. A. Liberzon, M. Guala, W. Kinzelbach, and A. Tsinober. On turbulent kinetic energy production and dissipation in dilute polymer solutions. *Phys. Fluids*, 18(12):125101, 2006. 1, 89
 84. A. Liberzon, M. Holzner, B. Luthi, M. Guala, and W. Kinzelbach. On turbulent entrainment and dissipation in dilute polymer solutions. *Phys. Fluids*, 21(3):035107, 2009. 1, 13
 85. S. C. Ling and C. A. Wan. Decay of isotropic turbulence generated by a mechanically agitated grids. *Phys. Fluids*, 15(8):1363–1369, 1972. 3
 86. R. C. Little. The effect of added salt on the flow of highly dilute solutions of poly(ethylene oxide) polymers. *J. Appl. Polym. Sci.*, 15(12):3117–3125, 1971. 14
 87. J. L. Lumley. Drag reduction by additives. *Annu. Rev. Fluid Mech.*, 1:367–384, 1969. 1, 9, 84
 88. J. L. Lumley. Drag reduction in turbulent flow by polymer additives. *J. Polym. Sci. Macrom. Rev.*, 7:263–290, 1973. 79, 84
 89. V. S. L’vov, A. Pomyalov, I. Procaccia, and V. Tiberkevich. Polymer stress tensor in turbulent shear flows. *Phys. Rev. E*, 71(1):016305, 2005. 90
 90. H. Makita. Realization of a large-scale turbulence field in a small wind tunnel. *Fluid Dyn. Res.*, 8:53–64, 1991. 3, 65, 75
 91. W. Marquardt and J. Nijmann. Experimental errors when using rotational rheometers. *Appl. Rheol.*, 3:120–129, 1993. 18
 92. W. D. McComb. *The physics of fluid turbulence*. Oxford University Press, 1990. 1, 3
 93. W. D. McComb, J. Allan, and C. A. Greated. Effect of polymer additives on the small-scale structure of grid-generated turbulence. *Phys. Fluids*, 20(6):873–879, 1977. 1, 2, 13, 82, 84, 95
 94. C. L. McCormick, R. D. Hester, S. E. Morgan, and A. M. Safieddine. Water-soluble copolymers. 30. Effects of molecular structure on drag reduction efficiency. *Macromolecules*, 23(8):2124–2131, 1990. 15
 95. R. D. Mehta. The aerodynamic design of blower tunnels with wide-angle diffusers. *Progress of Aerospace Science*, 18:59–120, 1977. 25
 96. M. S. Mohamed and J. C. LaRue. The decay power law in grid-generated turbulence. *J. Fluid Mech.*, 219:195–214, 1990. 35, 55, 58, 65
 97. A. S. Monin and A. M. Yaglom. *Statistical fluid mechanics*, volume 2. Dover, 2007. First published in 1975 by MIT Press. 45, 72

REFERENCES

98. L. Mydlarski and Z. Warhaft. On the onset of high-Reynolds-number grid-generated wind tunnel turbulence. *J. Fluid Mech.*, 320:331–368, 1996. 3, 61, 75
99. R. S. Neve and T. Shansonga. The effects of turbulence characteristics on sphere drag. *Int. J. Heat Fluid Fl.*, 10(4):318–321, 1989. 30
100. M. S. N. Oliveira, R. Yeh, and G. H. McKinley. Iterated stretching, extensional rheology and formation of beads-on-a-string structures in polymer solutions. *J. Non-Newton. Fluid*, 137(1-3):137–148, 2006. 15
101. N. T. Ouellette, H. Xu, and E. Bodenschatz. Bulk turbulence in dilute polymer solutions. *J. Fluid Mech.*, 629(-1):375–385, 2009. 2, 84, 89, 93
102. G. Patterson, J. L. Zakin, and J. Rodrigue. Drag reduction; polymer solutions soap solutions and solid particle suspensions in pipe flows. *Ind. Eng. Chem.*, 61(1):22–30, 1969. 1
103. J. M. Piau. A characteristic length for dilute drag reducing polymer-solutions: measurement using hot film anemometers. *Rheol. Acta*, 19(6):724–730, 1980. 31
104. C. J. Pipe. *Experiments investigating the effects of fluid elasticity on laminar vortex shedding from a cylinder*. PhD thesis, EPFL, 2005. 7, 13, 16, 25
105. C. J. Pipe and P. A. Monkewitz. Vortex shedding in flows of dilute polymer solutions. *J. Non-Newton. Fluid*, 139(1-2):54–67, 2006. 9, 18, 25
106. C. Poelma, J. Westerweel, and G. Ooms. Turbulence statistics from optical whole-field measurements in particle-laden turbulence. *Exp. Fluids*, 40(3):347–363, 2006. 35, 39
107. S. B. Pope. *Turbulent flows*. Cambridge University Press, fifth edition, 2008. 3, 4, 46, 58, 66, 71
108. A. K. Prasad. Stereoscopic particle image velocimetry. *Exp. Fluids*, 29:103–116, 2000. Overview on different setups. 36
109. M. Raffel, C. Willert, S. Wereley, and J. Kompenhans. *Particle image velocimetry: a practical guide*. Springer, 2007. 35, 37
110. A. Ramond and P. Millan. Measurements and treatment of LDA signals, comparison with hot-wire signals. *Exp. Fluids*, 28(1):58–63, 2000. 42
111. P. Roach. The generation of nearly isotropic turbulence by means of grids. *Int. J. Heat Fluid Fl.*, 8(2):82–92, 1987. 2
112. L. E. Rodd, T. P. Scott, J. J. Cooper-White, and G. H. McKinley. Capillary break-up rheometry of low-viscosity elastic fluids. *Appl. Rheol.*, 15(1):12–27, 2005. 9, 12
113. A. Rozhkov, B. Prunet-Foch, and M. Vignes-Adler. Impact of drops of polymer solutions on small targets. *Phys. Fluids*, 15(7):2006–2019, 2003. 7, 22, 24, 88
114. A. Rozhkov, B. Prunet-Foch, and M. Vignes-Adler. Dynamics and disintegration of drops of polymeric liquids. *J. Non-Newton. Fluid*, 134(1-3):44–55, 2006. 7
115. S. G. Saddoughi and S. V. Veeravalli. Local isotropy in turbulent boundary layers at high Reynolds number. *J. Fluid Mech.*, 268(-1):333–372, 1994. 35, 61
116. T. Sarpkaya, P. G. Rainey, and R. E. Kell. Flow of dilute polymer-solutions about circular cylinders. *J. Fluid Mech.*, 57(JAN23):177–208, 1973. 15
117. J. Schedvin, G. R. Stegen, and C. H. Gibson. Universal similarity at high grid Reynolds numbers. *J. Fluid Mech.*, 65(03):561–579, 1974. 34, 35
118. R. H. J. Sellin, J. W. Hoyt, J. Pollert, and O. Scrivener. The effect of drag reducing additives on fluid-flows and their industrial applications. 2. Present applications and future proposals. *J. Hydraul. Res.*, 20(3):235–292, 1982. 1

REFERENCES

119. R. E. Seoud and J. C. Vassilicos. Dissipation and decay of fractal-generated turbulence. *Phys. Fluids*, 19(10):105108, 2007. 75
120. J. Sheng, H. Meng, and R. O. Fox. A large eddy PIV method for turbulence dissipation rate estimation. *Chem. Eng. Sci.*, 55(20):4423–4434, 2000. 35
121. A. V. Shenoy. A review on drag reduction with special reference to micellar systems. *Colloid Polym. Sci.*, 262(4):319–337, 1984. 13
122. L. Simon and J. Fitzpatrick. An improved sample-and-hold reconstruction procedure for estimation of power spectra from LDA data. *Exp. Fluids*, 37(2):272–280, 2004. 43, 44
123. K. A. Smith, E. W. Merrill, H. S. Mickley, and P. S. Virk. Anomalous Pitot tube and hot film measurements in dilute polymer solutions. *Chem. Eng. Sci.*, 22(4):619–626, 1967. 31
124. S. M. Soloff, R. J. Adrian, and Z.-C. Liu. Distortion compensation for generalized stereoscopic particle image velocimetry. *Meas. Sci. Technol.*, 8:1441–1454, 1997. 37
125. D. Sree, S. O. Kjølgaard, and W. L. Sellers. Effect of non-Poisson samples on turbulence spectra from laser velocimetry. *AIAA*, 32(12):2480–2481, 1994. 42
126. K. R. Sreenivasan. On the universality of the Kolmogorov constant. *Phys. Fluids*, 7(11):2778–2784, 1995. 4
127. F. J. Stadler, C. Piel, J. Kaschta, S. Rulhoff, W. Kaminsky, and H. Münstedt. Dependence of the zero shear-rate viscosity and the viscosity function of linear high-density polyethylenes on the mass-average molar mass and polydispersity. *Rheol. Acta*, 45:755–764, 2006. 18, 19
128. R. W. Stewart and A. A. Townsend. Similarity and self-preservation in isotropic turbulence. *Philos. T. R. Soc. S. A*, 243(867):359–386, 1951. 2
129. J. H. Sung, S. T. Lim, C. A. Kim, H. J. Chung, and H. J. Choi. Mechanical degradation kinetics of poly(ethylene oxide) in a turbulent flow. *Koera-Aust. Rheol. J.*, 16(2):57–62, 2004. 23, 81
130. N. D. Sylvester and J. S. Tyler. Dilute solution properties of drag-reducing polymers. *Ind. Eng. Chem. Prod. Res. Develop.*, 9(4):548–553, 1970. 14, 15
131. K. C. Tam and C. Tiu. A low viscosity, highly elastic ideal fluid. *J. Non-Newton. Fluid*, 31:163–177, 1989. 8
132. K. C. Tam and C. Tiu. Steady and dynamic shear properties of aqueous polymer-solutions. *J. Rheol.*, 33(2):257–280, 1989. 7, 12, 13, 15, 23
133. K. C. Tam and C. Tiu. Rheology of water-soluble polymers: a comparative study on the effect of monovalent salt. *Polym.-Plast. Technol.*, 32(1):123–138, 1993. 14
134. H. Tennekes and J. L. Lumley. *A first course in turbulence*. MIT Press, 1972. 3, 4, 33, 45, 69, 71
135. B. Thiele and H. Eeckelmann. Application of a partly submerged 2-component laser-Doppler anemometer in a turbulent-flow. *Exp. Fluids*, 17(6):390–396, 1994. 42
136. V. Tirtaatmadja, G. H. McKinley, and J. J. Cooper-White. Drop formation and breakup of low viscosity elastic fluids: effects of molecular weight and concentration. *Phys. Fluids*, 18(4):043101, 2006. 9, 10, 15
137. B. A. Toms. The flow of linear polymer solutions through straight tubes at large Reynolds numbers. In *Proc. First intern. Cong. on Rheology*, volume 2, page 135. North-Holland Publishing Company, 1948. 1
138. M. Ubroi and S. Wallis. Small axisymmetric contraction of grid turbulence. *J. Fluid*

REFERENCES

- Mech.*, 24:539–543, 1966. 27
139. T. Ursenbacher. *Traitement de vélocimétrie par images digitales de particules par une technique robuste de distortion d’images*. PhD thesis, EPFL, 2000. 36, 37, 38
 140. J. H. J. Van Der Meulen. Friction reduction and degradation in turbulent-flow of dilute polymer-solutions. *Appl. Sci. Res.*, 29(3):161–174, 1974. 23, 79
 141. E. van Doorn, C. White, and K. Sreenivasan. The decay of grid turbulence in polymer and surfactant solutions. *Phys. Fluids*, 11(8):2387–2393, 1999. 1, 2, 83, 89, 95
 142. H. R. E. van Maanen and A. Oldenziel. Estimation of turbulence power spectra from randomly sampled data by curve-fit to the autocorrelation function applied to laser-Doppler anemometry. *Meas. Sci. Technol.*, 9(3):458–467, 1998. 42
 143. H. R. E. van Maanen, H. Nobach, and L. H. Benedict. Improved estimator for the slotted autocorrelation function of randomly sampled LDA data. *Meas. Sci. Technol.*, 10(1):L4–L7, 1999. 42
 144. S. A. Vanapalli, S. L. Ceccio, and M. J. Solomon. Universal scaling for polymer chain scission in turbulence. *P. Natl. Acad. Sci. USA*, 103(45):16660–16665, 2006. 23, 24
 145. P. S. Virk. Drag reduction fundamentals. *AIChE J.*, 21(4):625–656, 1975. 1, 79
 146. P. S. Virk, E. W. Merrill, H. Mickley, K. A. Smith, and E. L. Mollo-Christensen. The Toms phenomenon: turbulent pipe flow of dilute polymer solutions. *J. Fluid Mech.*, 30:305–328, 1967. 1, 31, 90, 95
 147. H. Wang and W. K. George. The integral scale in homogeneous isotropic turbulence. *J. Fluid Mech.*, 459(-1):429–443, 2002. 55, 66, 69, 72
 148. M. D. Warholic, H. Massah, and T. J. Hanratty. Influence of drag-reducing polymers on turbulence: effects of Reynolds number, concentration and mixing. *Exp. Fluids*, 27(5):461–472, 1999. 84, 93, 95
 149. J. Westerweel and F. Scarano. Universal outlier detection for PIV data. *Exp. Fluids*, 39(6):1096–1100, 2005. 38
 150. B. Wieneke. Stereo-PIV using self-calibration on particle images. *Exp. Fluids*, 39(2): 267–280, 2005. 37
 151. C. H. K. Williamson and R. Govardhan. Dynamics and forcing of a tethered sphere in a fluid flow. *J. Fluid. Struct.*, 11(3):293–305, 1997. 3, 30, 52, 75
 152. J. C. Wyngaard. Measurement of small-scale turbulence structure with hot wires. *J. Phys. E Sci. Instrum.*, 1(11):1105–1108, 1968. 32, 34
 153. D. M. Yu, G. L. Amidon, N. D. Weiner, and A. H. Goldberg. Viscoelastic properties of poly(ethylene oxide) solution. *J. Pharm. Sci.*, 83(10):1443–1449, 1994. 14, 77

List of Figures

- 2.1 Intrinsic viscosity, 16
- 2.2 Zero-shear viscosity plotted against polymer concentration, 17
- 2.3 Concentration and temperature dependence of the zero-shear viscosity, 18
- 2.4 Carreau-Yasuda model fitted to reduced shear viscosity data, 19
- 2.5 Carreau-Yasuda parameter dependence on polymer concentration, 20
- 2.6 Rescaled Carreau-Yasuda model for various solutions, 21
- 2.7 Steady shear viscosity and complex shear viscosity, 22
- 2.8 Reduced elastic and viscous moduli with fitted Maxwell model, 23
- 2.9 Polymer relaxation time vs. polymer concentration, 24

- 3.1 Overview of the closed-loop flow facility, 26
- 3.2 Schematic representation of the test section, 27
- 3.3 Free-stream quality, 28
- 3.4 Turbulence grid with tethered spheres ITG, 29
- 3.5 Trajectory & power spectrum of tethered beads, 30
- 3.6 Polynomial fit and model function for a measured spectrum, 33
- 3.7 Spectrum correction for finite resolution, 34
- 3.8 Convected Taylor vortex array, 39
- 3.9 PIV error for a convected Taylor vortex array, 40
- 3.10 PIV error due to particle loss, 40
- 3.11 LDA spectrum test, 44
- 3.12 Taylor microscale parabola fit, 49

- 4.1 Static pressure drop coefficient of the turbulence grids, 52
- 4.2 Velocity profiles in the near grid wakes, 53
- 4.3 Turbulence homogeneity of the RTG and the W12 grid, 54
- 4.4 Turbulence homogeneity of the ITG, 55
- 4.5 Streamwise turbulence decay of the RTG, 56
- 4.6 Streamwise turbulence decay of the ITG, 57
- 4.7 Large scale isotropy levels, 58
- 4.8 Rescaled streamwise decay of all grids, 59
- 4.9 Streamwise turbulence energy production, 60
- 4.10 Longitudinal and lateral velocity spectra of all tested grids, 62
- 4.11 Spectra compensated for the scaling region, 63
- 4.12 Ratios of the transverse to longitudinal spectra, 64
- 4.13 Velocity probability density functions, 65
- 4.14 Velocity spectra of the RTG, 67
- 4.15 Velocity spectra of the ITG, 68

LIST OF FIGURES

- 4.16 Longitudinal and lateral correlation coefficient, 70
- 4.17 Dissipation rate measured with PIV, 73
- 4.18 Streamwise evolution of the Taylor microscale, 74

- 5.1 Evolution of the viscosity and the pressure drop, 80
- 5.2 Evolution of turbulence kinetic energy and isotropy, 83
- 5.3 Velocity spectra in 25 wppm PEO solution, 85
- 5.4 Velocity spectra in 50 wppm PEO solution, 86
- 5.5 Velocity spectra in 100 wppm PEO solution, 87
- 5.6 Evolution of the Lumley scale and the Weissenberg number, 88
- 5.7 Ratio between viscous and total dissipation rate, 91
- 5.8 Evolution of the Taylor microscale, 91
- 5.9 Model spectrum for turbulence in polymer solutions, 92

List of Tables

- 3.1 Test grids with tethered spheres, 29
- 3.2 Summary of experiments, 49
- 4.1 Streamwise turbulence energy decay and production, 58
- 4.2 Skewness and kurtosis of velocity distributions, 65
- 4.3 Summary of turbulence length scales and dissipation rates, 69
- 5.1 Experimental conditions, 78
- 5.2 Parameters of the fitted cascade model, 82

Notation

Acronyms and abbreviations

CY	Carreau-Yasuda model, 10
FFT	fast Fourier transform, 38
HFA	hot-film anemometry, 31
ITG	improved turbulence grid, 28
IW	interrogation window, 37
LDA	laser Doppler anemometry, 41
PEO	poly(ethylene oxide), 13
PIV	particle image velocimetry, 35
psd	power spectral density function, 29
rms	root mean square, 3
RTG	reference turbulence grid, 28
TS	test section, 25
wppm	weight parts per million, 14
wt%	percent by weight, 14

Nondimensional numbers

Re_{cs}	coil-stretch Reynolds number, 78
Re_M	grid based Reynolds number, 28
Re_λ	turbulence Reynolds number, 3
Sk	Stokes number, 36
St	Strouhal number, 30
Wi	Weissenberg number, 10

Greek letters

α	Kolmogorov constant, 4
β	solvent quality parameter, 15
$\dot{\gamma}$	rate-of-strain magnitude, 8
Δt	time lapse, 40
δ_{ij}	Kronecker delta, 3
ϵ	dissipation rate of energy, 4
ϵ_p	elastic dissipation rate of energy, 90
ϵ_v	viscous dissipation rate of energy, 89
ϵ_0	total dissipation rate of energy, 83
ζ	derivative filter function, 46
η	Kolmogorov length scale, 4
η_p	viscous scale in polymer spectrum, 88
κ_i	wavenumber component, 3
κ_c	cut-off wavenumber, 41
Λ	integral length scale, 4

NOTATION

Λ_1, Λ_2	longitudinal and transverse integral scale, 48
λ	Taylor microscale, 4
μ	dynamic viscosity, 8
μ_{inh}	inherent viscosity, 9
μ_{M}	Maxwell viscosity, 11
μ_{red}	reduced viscosity, 9
μ_{s}	solvent viscosity, 9
μ_0	zero-shear viscosity, 11
μ_{∞}	infinite-shear viscosity, 11
μ^*	complex viscosity, 20
$[\mu]$	zero-shear intrinsic viscosity, 9
ν	kinematic viscosity, 3
ξ_{ii}	white noise level, 40
ρ	solution mass per unit volume, 17
ρ_{b}	bead mass per unit volume, 28
ρ_{t}	tracer particle mass per unit volume, 35
τ	relaxation time, 10
τ_{CY}	Carreau-Yasuda time constant, 11
τ_{M}	Maxwell relaxation time, 11
τ_{P}	Lumley scale relaxation time, 22
τ_{R}	Rozhkov relaxation time, 22
τ_{Z}	Zimm relaxation time, 12
Φ_{ij}	spectrum tensor, 3
ϕ_{ij}	one-dimensional spectrum function, 3
χ, χ^*	spectral filter function, 32
ψ	stream function, 38
ψ_0	Taylor vortex intensity, 38
ω	angular frequency, 11

Roman letters

A_{dk}	streamwise energy decay coefficient, 55
a_{CY}	CY transition parameter, 11
B_{ij}	two-point correlation function, 48
C_p	pressure drop coefficient, 51
c	polymer concentration, 9
c^*	coil overlap concentration, 9
D	bead diameter, 28
D^*	relative bead diameter, 28
D_{ij}	deviatoric stress tensor, 8
d	grid rod diameter, 28
d_{t}	tracer particle diameter, 35
d_{T}	Taylor vortex diameter, 38
E	three-dimensional spectrum function, 3
e_{p}	potential elastic energy, 90
f	frequency, 32
f_{K}	Kolmogorov frequency, 31
f_{c}	data rate filter cut-off frequency, 43
f_{s}	sampling frequency, 43
G^*	complex modulus, 11
G', G''	storage and loss modulus, 11
H	test section height, 25

NOTATION

K	Mark-Houwink constant, 15
K_{u_i}	kurtosis, 65
k	turbulence kinetic energy, 2
L_1, L_2	tether lengths, 29
L_1^*, L_2^*	relative tether lengths, 29
l	HFA film length, 31
ℓ	eddy length scale, 84
ℓ_p	three-dimensional Lumley scale, 84
$\ell_{p,1}, \ell_{p,2}$	one-dimensional Lumley scales, 84
M	grid mesh width, 28
M_v	viscosity average molecular weight, 12
m^*	relative bead density, 28
n_{CY}	CY exponent, 11
n_{dk}	streamwise energy decay exponent, 55
\dot{n}	average data rate, 42
\mathcal{P}	turbulence kinetic energy production, 59
Q_E	three-dimensional spectrum correction, 47
Q_E^ε	dissipation rate correction, 47
Q_i	squared rms velocity correction, 33
Q_i^ε	dissipation rate correction, 34
Q_{ii}^ϕ	one-dimensional spectrum correction, 33
q^2	twice the turbulence kinetic energy, 55
R	universal gas constant, 12
S_{ij}	rate-of-strain tensor, 2
S_{u_i}	skewness, 65
s	eddy shear rate, 89
s_{ij}	fluctuating rate-of-strain tensor, 2
T	temperature, 12
t	eddy turnover time, 84
t_K	Kolmogorov time scale, 78
\bar{U}_i	time averaged velocity component, 27
U_i	velocity component, 2
U_0	mean flow velocity, 25
u	eddy velocity, 93
u_i	fluctuating velocity component, 2
u'_i	rms velocity, 3
W	test section width, 25
x_i	Cartesian coordinates, 27
y_i	Cartesian image coordinates, 38
Sub- and superscripts	
dk	streamwise decay, 55
m	measured quantity, 33
max	maximum, 17
p	polymer, 84
ref	reference, 12
s	solvent, 9
\sim	reduced variables, 12

Curriculum Vitae

Richard Vonlanthen

born on november 7th 1979

Doctoral studies

2005–2010 Ph.D. at the Laboratory of Fluid Mechanics (LMF), EPFL;
prof. P. A. Monkewitz.

Diploma studies

2000–2005 M.Sc. in mechanical engineering at the EPFL; award winning
diploma thesis (Prix Ryhming); Dr. M. Farhat.